EVALUATION OF MECHANICAL PROPERTIES AND CORROSION BEHAVIOR OF WIRE ARC ADDITIVELY MANUFACTURED 13CR (AISI 420)

by

© Jonas Halvorsen Lunde

A Thesis submitted to the

School of Graduate Studies

in partial fulfillment of the requirements for the degree of

Master's of Mechanical Engineering

Faculty of Engineering

Memorial University of Newfoundland

October 2021

St. John's Newfoundland and Labrador

Abstract

In this study, a 13Cr stainless steel multi-layer thin-wall part was fabricated using wire arc additive manufacturing (WAAM). In Chapter 1 the microstructure and mechanical properties of the bottom, middle and top regions in as-printed condition were investigated. A multi-phase microstructure consisting of a hard martensitic matrix along with retained austenite and delta ferrite was detected for all regions. The top region exhibited both lower strength and elongation compared with the other regions, due to the presence of harder martensite with vermicular delta ferrite. In Chapter 2 a post-fabrication heat treatment was applied to the as-printed part. Here, austenitizing and quenching eliminated the detrimental secondary phases and the microstructure and corrosion behavior after tempering at 300°C, 400°C, 500°C, and 600°C for 2 hours were investigated. Electrochemical tests revealed that tempering at 400°C provided the best corrosion resistance and tempering at 500°C provided the worst resistance. In chapter 3 tempering at 400°C was looked into further by varying the tempering time; 1 h, 2h, 4h, and 8h were investigated by microstructural observations and electrochemical testing. A decreasing corrosion resistance with increasing tempering time was found due to the growth of intergranular carbide precipitates.

General summary

By using a metal 3D-printing technology called wire arc additive manufacturing a 13Cr stainless steel wall was fabricated. The mechanical properties and microstructure of the bottom, middle and top regions of the wall were investigated in Chapter 1 using tensile and hardness tests, and scanning electron microscope, respectively. This revealed a hard and brittle wall, with the top regions showing lowest strength and elongation. For Chapter 2 the wall was subjected to heat treatment to achieve uniform properties throughout. Subsequently, the microstructure and corrosion resistance were evaluated after heat treatment at 300°C, 400°C,

500°C, and 600°C for 2h, which revealed that 400°C provided the best and 500°C the worst corrosion resistance. Chapter 3 tested 400°C further by varying the heat treatment time. Heat treatment for 1h, 4h, and 8h were investigated in addition to 2h. Here it was determined that increasing time led to decreasing corrosion resistance.

Acknowledgments

First and foremost, I would like to give my sincerest gratitude to my supervisor during my Master's thesis study, Dr. Ali Nasiri. His guidance, support, and availability throughout my entire program of study kept me motivated to extend and improve my knowledge. Not only as a supervisor, but as a mentor as well, I could not have wished or asked for more support.

Secondly, I would like to thank the support of Suncor Energy and the Memorial University of Newfoundland for sponsoring this work.

A special thanks is given to the members of my research group. I appreciate the conversations and discussions we had, and the assistance I was given with experiments and research.

Last but certainly not least, I would like to thank my family and friends for keeping me motivated throughout this journey. Whether it be in person or via long distance communication your words and actions have been greatly appreciated.

Contents

List of Figures

List of Tables

Chapter 1

Introduction

1.1 Stainless steels

The early discoveries of stainless steels (SS) began in the 18th and 19th centuries when chromium metal first was isolated, with the most significant advancements taking place in the early 20th century [1]. Harry Brearly along with Benno Strauß and Eduard Maurer are usually credited with the discovery of what is known as SS today [2, 3]. The development of alloy steels was driven by the aim of improving cutting instruments and to determine whether the new and improved alloy would improve corrosion resistance as well [1]. Initially, in the early 19th century, noble metals in addition to chromium and nickel were added to steel [1, 4]. However, the best performing alloys, containing platinum and rhodium, were deemed impractical due to the high concentrations required of the noble alloying elements. It was soon after found that the corrosion resistance of iron-chromium alloys was highly dependent on the chromium content, with an increasing chromium content providing greater corrosion resistance [1].

There were strong doubts with regards to producing engineering alloys with 12-30 % chromium as the high carbon contents of the already existing alloys obscured the parts' properties. It was not until late in the 19th century that methods for reducing the carbon contents viably were discovered, and even later that higher corrosion resistance was related to lower carbon content was documented [5]. The method for reducing carbon content was an important discovery, paving the way for the first developments of different SS variants in the early 20th century Through experimenting with carbon, chromium, and nickel content in the alloys three subdivisions of SSs were established: ferritic, martensitic, and austenitic. Further investigation

of the new alloys revealed significant improvement of corrosion resistance as the chromium content of the alloy approached 12 %, attributed to passivation. It was also established that excess carbon content in the alloys led to carbide precipitation, which was detrimental to the passivation [1].

Generally, an iron-based alloy needs approximately 11 % chromium to be considered stainless, as this is the minimum percentage of chromium where a protective passive oxide layer can form on the surface of the alloy [6]. SSs rarely contain above 30 % chromium or lower than 50 % iron, with carbon contents ranging from below 0.03 % to 1.0 % for certain alloys [7]. A representation of how the addition of certain elements provide specific types of SS is illustrated in Figure 1.1. Due to the flexibility of SS alloys, there exists a wide range of applications, such as cutlery, cooking utensils and fasteners, as well as in industries such as transportation, petroleum, and textile plants [8]. SSs are now commonly divided into five different categories: ferritic, austenitic, martensitic, duplex, and precipitation hardenable alloys. The precipitation hardenable alloys differ from the rest, as these alloys are categorized based on the heat treatment used, whereas the others are categorized by crystallographic structure [7].

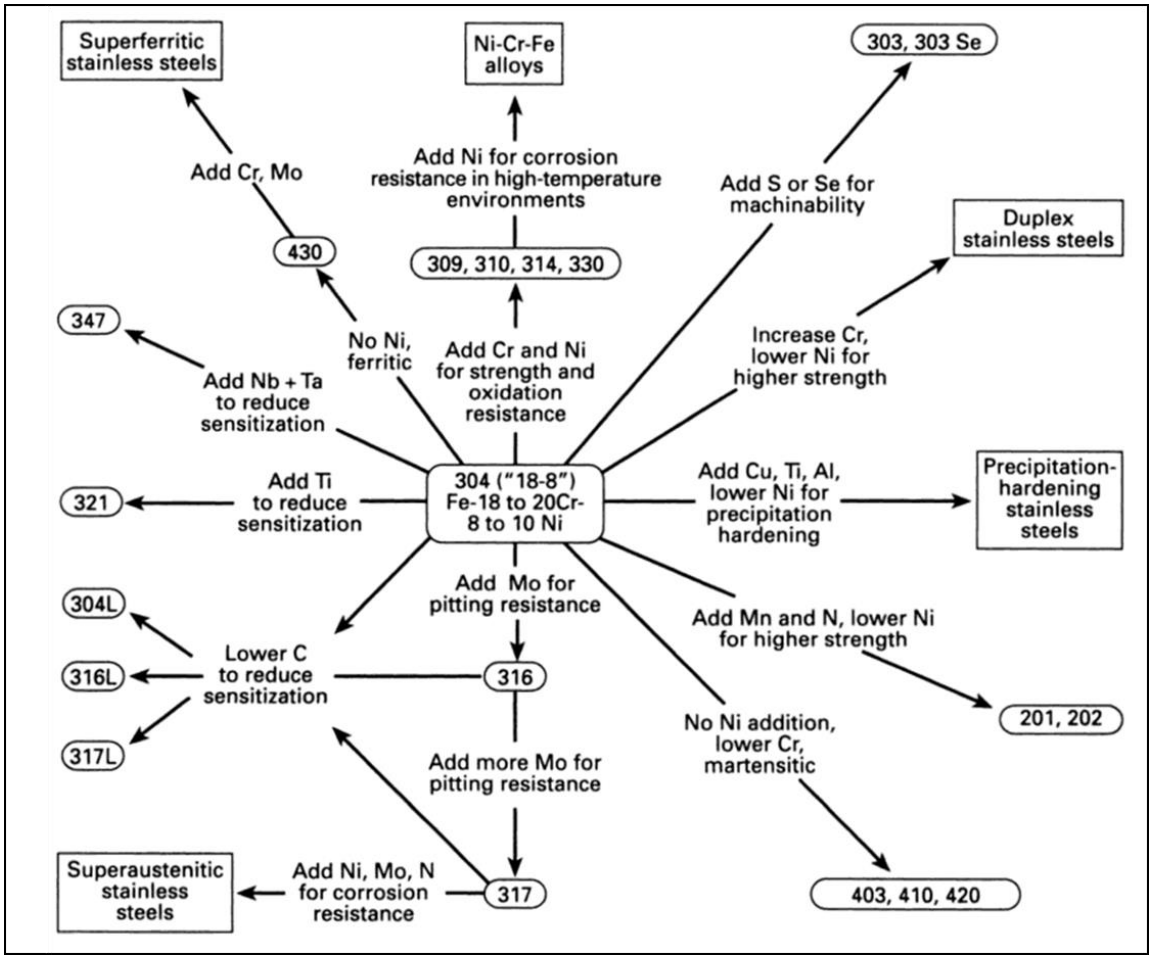

Figure 1.1. Illustration showing how addition of certain alloying elements leads to specific SS alloys [7].

Ferritic SSs are magnetic alloys consisting of body-centered cubic (bcc) crystal structure without the ability to be hardened by heat treatment [9]. These alloys generally possess poor toughness and are susceptible to sensitization [7]. The chromium content of ferritic SSs is normally from 12 % and up and their applications strongly depend on the amount of chromium present [6]. Alloys with lower chromium content can be produced at relatively low cost and provide fair corrosion resistance combined with good fabrication opportunities. Increasing the chromium content naturally improves the corrosion resistance, however this comes at the expense of toughness and weldability [7].

Austenitic alloys are non-magnetic with face-centered cubic crystal structure which are unable to be hardened by heat treatment, however hardening is possible through cold work [7, 9]. These alloys combine excellent ductility, toughness, formability, and corrosion resistance [10]. Austenite stabilizing elements (nickel, carbon, and nitrogen) combined with ferrite stabilizing elements (chromium and molybdenum) provides the mentioned corrosion resistance. Low alloy austenitic alloys are often used in applications where sliding wear is an issue, as when sufficiently work hardened the austenite transforms to harder martensite [7]. Alloys with high chromium content and corrosion resistant molybdenum added are used in highly corrosive environments and applications involving high temperatures, whereas high-nickel alloys are more suitable for acidic environments [7].

Martensitic SSs have a body-centered tetragonal crystal structure and are hardenable magnetic alloys [9]. The carbon content of martensitic alloys plays a big role in determining the mechanical properties, with increasing carbon leading to an increase in strength but a decrease in ductility and toughness [7]. Higher hardness is also related to higher carbon content, making high carbon martensitic alloys suitable for application requiring high adhesive and abrasive wear resistance [6]. To improve toughness and corrosion properties both molybdenum and nickel can be added to the alloys, however, the addition of these elements can result in a multiphase microstructure [6, 7].

The precipitation-hardenable alloys can all be hardened by aging treatments, and can be either austenitic, semi-austenitic, or martensitic [7, 9]. These alloys have good ductility and toughness and a moderate resistance to corrosion, which provides these alloys with a better combination of strength and corrosion resistance than the martensitic alloys [6]. The precipitation-hardened alloys have higher chromium, nickel, and molybdenum contents as well as a normally lower carbon content compared with the martensitic alloys, providing the improved properties [7].

Duplex SSs consist partly of ferrite and partly austenite, providing better toughness and ductility compared with the ferritic alloys and improved resistance to stress-corrosion cracking compared with the austenitic alloys [11]. Yield strengths are also increased for duplex alloys compared with both ferritic and austenitic alloys [7]. The addition of nitrogen to duplex alloys increases the amount of austenite in the mixture, thus improving corrosion resistance [11, 12]. A comparison of the minimum yield stress and pitting corrosion resistance between certain SS grades is shown in Figure 1.2.

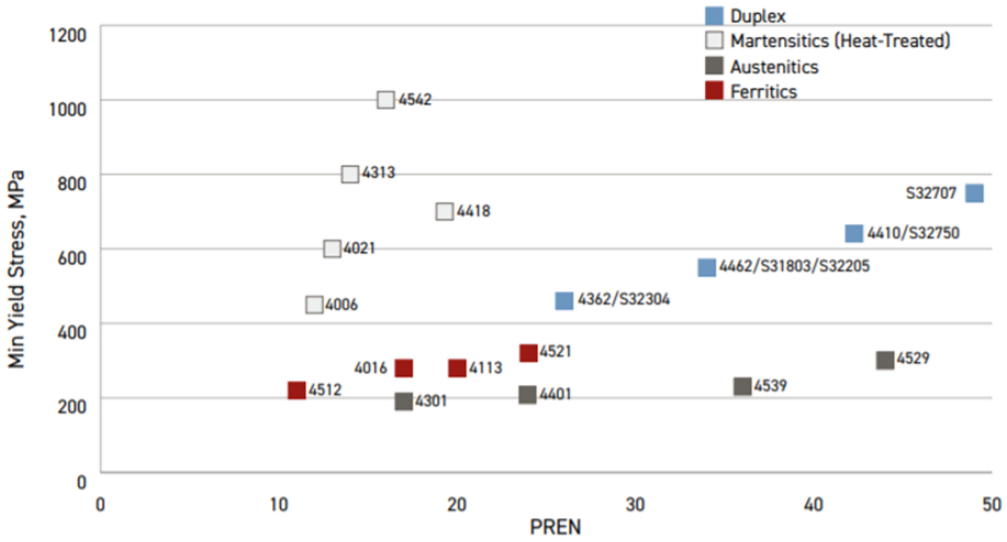

Figure 1.2. Comparison of minimum yield stress and resistance to pitting corrosion (PREN) between some SS grades [11].

As mentioned, the alloying elements added to SSs strongly affect the crystal structure and the formation of phases in the alloys. Carbon and chromium are the principal alloying elements in ferritic and martensitic alloys, whist the addition of nickel makes austenitic and duplex alloys. In addition to these, SSs also include intentional amounts of manganese and silicon, with the possibility to add a number of other alloying elements. These elements include molybdenum, titanium, nitrogen, and aluminum, to mention a few, which individually all can affect fabricability, corrosion resistance and microstructure [12].

The addition of chromium provides corrosion protection for the steel due to the formation of an $(Fe,Cr)_2O_3$ oxide on its surface [9, 12]. Chromium combines with oxygen more easily than iron; thus an increasing chromium content provides a more stable oxide [12, 13]. As chromium is a ferrite promoting element, a higher content of chromium in the alloy will promote the formation and retention of ferrite in all of martensitic, austenitic, and duplex alloys. In addition, chromium promotes the formation of carbide precipitates which, as mentioned, can be detrimental to corrosion performance [12].

As an austenite promoting element, nickel added to an alloy will cause the formation of more austenite phase, and a sufficient amount will make the austenite phase stable at room temperature and lower [12]. The general corrosion resistance of ferritic alloys has been shown to increase with the addition of nickel, especially in environments containing sulfuric acid [12]. The addition of nickel to ferritic and martensitic grades can improve toughness, as well as reduce the ductile-to-brittle fracture transition temperature [12].

The addition of manganese to SS (1-2 wt.% in austenitic and less than 1 wt.% in ferritic and martensitic) is to avoid cracking during solidification. The cause of the solidification cracks was the formation of eutectic iron-sulfide phases with low melting points. As manganese more easily combines with sulfur than iron, manganese sulfides (MnS) form instead, eliminating the issue of solidification cracking [12, 14]. Manganese can effectively prevent the formation of austenite to martensite at low temperatures [9]. 0.3-0.6 wt.% silicon is added to virtually all alloys of SSs to provide deoxidation during the melting process.

High concentrations of silicon (4-5 wt.%) affect corrosion resistance positively and is added to certain heat-resistant alloys to improve the resistance to scaling of oxides at higher temperatures [12]. Larger amounts of silicon added to ferritic and martensitic alloys promotes the formation of ferrite, as it is a ferrite stabilizing element [15]. Molybdenum is a commonly

used alloying element which provide different properties depending on the type of SS it is added to [12]. An improved resistance to pitting corrosion is achieved for SSs alloyed with molybdenum due to making the passive film more stable [16]. Since molybdenum is a ferrite promoting element it can cause retention of undesirable ferrite in the microstructure of martensitic alloys, causing reduction of toughness and ductility. To improve yield and ultimate tensile strength molybdenum is added to martensitic alloys as a carbide former which increases the secondary hardening characteristics [12].

To avoid the formation of detrimental carbide precipitates ($M_{23}C_6$) in the grain boundaries, which are highly involved in intergranular corrosion, other carbide forming elements are added. Titanium and niobium for example stabilizes the carbon in austenitic steels preventing the formation of the chromium-rich precipitates. These carbide forming elements work as ferrite promoters because they occupy the carbon, which is a strong austenite stabilizer, in addition to being ferrite stabilizers themselves [12].

1.2 Metal additive manufacturing

In 1920 electric arcs and metal electrodes were used to form walled structures, and many modern day additive manufacturing (AM) techniques are based on similar ideas [17]. Modern day AM uses 3D model data to fabricate near-net shape components in a layer-by-layer fashion. This method makes it possible to produce more complex designs cheaper with less material waste, lead time, and energy consumption compared with the more conventional subtractive methods [18]. In addition, computer-aided design (CAD) files can be used to produce parts that are still required for operation, but the fabricators of these parts are no longer available. Most of the AM activity around the world is related to polymer-based systems, however AM of metals is desirable for many industries due to the possibility of producing components of high quality at lower manufacturing costs [19].

Metal AM processes can be divided into two main groups: powder bed fusion (PBF) and directed energy deposition (DED), which again can be classified further depending on the energy source used [18, 20]. In addition to the energy source there is another parameter associated with the metal AM process, this being the input raw material which is either metal powder or wire [20]. PBF involves the selective fusion of metal powder with thermal energy based on the 3D model of the desired part [18]. A repeating process where powder is raked across the work area and fused by either laser or electron beam as the energy source is continued until the 3D part is produced [21]. DED processes can use both powder and wire as the feedstock material which is fused during deposition [18]. The powder feed systems use laser to melt the powder fed through a nozzle onto the substrate, and the desired shape is achieved by either movement of the deposition head or the work piece [21]. Similarly, the wire feed systems use either electron beam, laser beam or plasma arc as heat source to melt metal wire onto the substrate, achieving the shape by subsequent passes where a single material bead is deposited each time [21]. Schematics of the three mentioned AM systems can be seen in Figure 1.3.

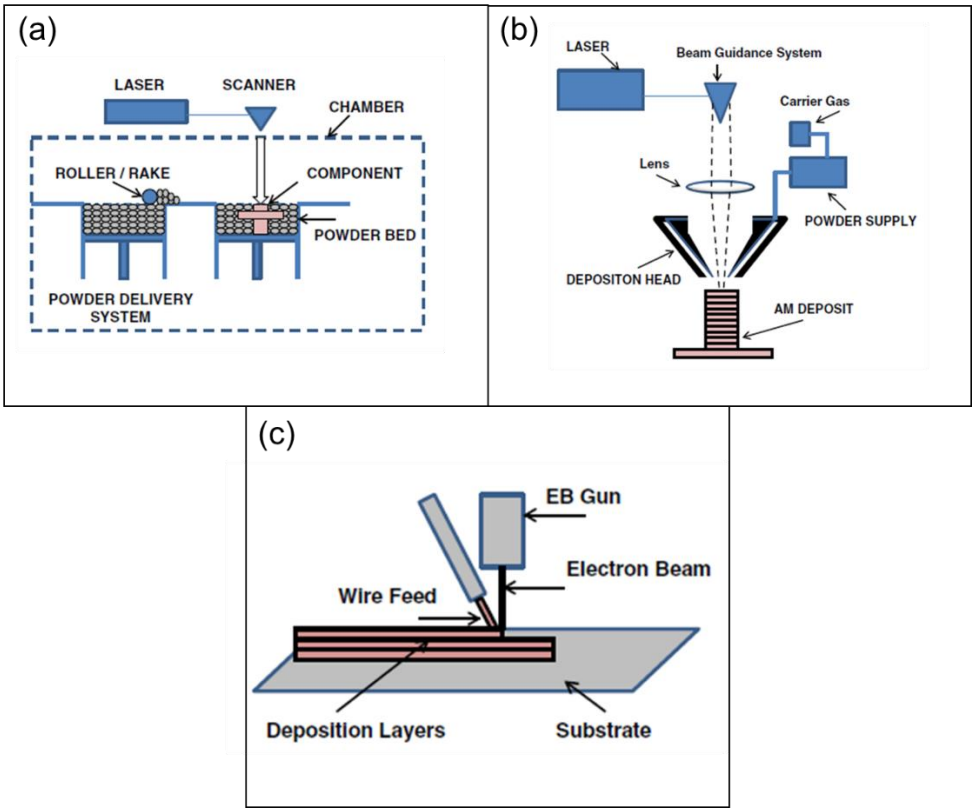

Figure 1.3. Schematic illustrations of (a) a powder bed system, (b) a powder feed system, and (c) a wire feed system (Adapted from [21]**)**.

Within the two main metal AM groups there are several different processes available, such as electron beam melting (EBM) and selective laser melting/sintering (SLM/SLS) for PBF and laser engineering net shaping (LENS) and direct metal deposition (DMD) for DED [22]. PBF is mainly used for rapid prototyping and the fabrication of high end parts, whereas applications for DED include part reparations and adding features to already existing parts [23]. DED processes generally have higher build speeds and can produce larger parts compared with PBF. However, a higher freedom of design, geometrical complexity and surface quality is associated with PBF [23].

From an industry perspective there are situations where the freedom of design associated with AM has both advantages and disadvantages. As there are few professionally trained AM manufacturers and AM software is expensive, there is skepticism shown with regards to the

fundamental design guidelines for AM technologies. There is also debate whether AM should be considered under traditional design for manufacturing and assembly principals, or if it should have its own manufacturing design regulation. Quality assurance and control can also be complicated when it comes to AM, as there is unpredictability of the produced parts associated with defects and surface roughness differences. Where subtractive manufacturing methods can produce low-complexity parts with high precision, AM can produce more complex components with poor tolerance and relative quality [24].

When comparing metal AM with more conventional subtractive manufacturing methods certain advantages and disadvantages are revealed [25]:

- AM achieves the desired part geometry while using the material efficiently, related to the layer-by-layer deposition method, whereas subtractive methods require substantial amounts of material to be removed.
- By the use of AM parts can be made to have different mechanical properties in some areas compared to others. Complex parts can be fabricated without sacrificing functionality to simplify manufacturing.
- AM can produce parts without the need for resources in addition to the main machine tool associated with subtractive methods. This allows for parts to be produced near to customers which creates improved dynamics in supply chains.
- Production of AM parts can be easily synchronized with the requirements of the customer, as the part quality is related to the process and not skill of the operator.
- The size of AM parts is restricted by the size of the build chamber and larger parts require long build times. Build defects and inhomogeneity are common problems in AM parts, and the cost associated with the fabrication is higher than for subtractive methods.

Although approximately 33 % of the published literature on metal AM are on steels, they are still mainly fabricated with conventional methods. Understanding the effect of the AM processes on microstructure, mechanical properties and corrosion behavior is key to improving reproducibility and gain industry acceptance for AM of steels [26]. The thermal history that an AM part experiences is very different from what a conventionally fabricated part experiences [27]. Process parameters such as high cooling and solidification rates and high thermal gradients play a big role in determining the final microstructure of the part [28]. This is also what allows AM to fabricate components with site-specific mechanical/corrosion properties [26]. Figure 1.4 depicts the microstructure of some steels and SSs after produced by PBF and DED compared with conventional methods.

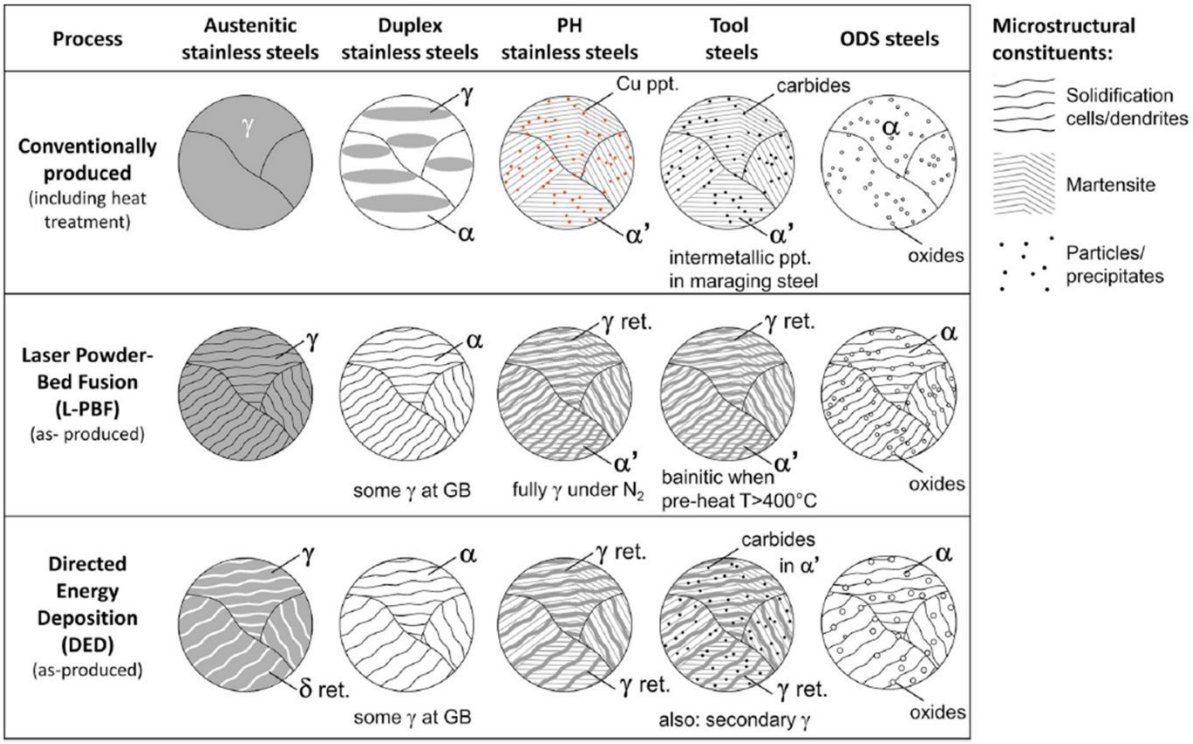

Figure 1.4. Illustration of the microstructural phases that can be expected in parts fabricated by conventionally methods and some AM processes [29].

The SSs used most often for AM are the austenitic alloys, with martensitic, duplex and precipitation hardened alloys being less commonly used [29]. It is common for the as-printed

microstructure of SSs to not be the desired microstructure for application [30–32]. The high cooling rates associated with fabrication can cause a change in the primary solidification phase and incomplete phase transformations, and microsegregation during solidification can lead to a local difference in the stability of phases [29]. These inhomogeneities may need to be eliminated by post-processing heat treatments.

Wire arc additive manufacturing (WAAM) is a DED type AM process able to fabricate large components by utilizing welding equipment with metal wire as the feedstock material [33, 34]. Using electric arc as heat source this specific DED process is superior to PBF in terms of lower material waste, higher deposition rates, lower cost, and part size limitations, however part complexity is limited [33]. As the metal wire is fed through the nozzle of the robotic weld arm it is simultaneously melted and deposited onto the metal substrate. This process is repeated until the desired part shape and dimensions are achieved, as is shown in Figure 1.3. WAAM with electric arc as heat source requires careful optimization of the process parameters to ensure good quality of the fabricated parts. The parameters involved are current intensity, voltage, type of shielding gas, flow rate of the shielding gas, distance between nozzle and substrate, travel and wire feed speed, and angle of torch [29]. These all play a role in affecting the transfer mode, which strongly influences the width and size of the deposited beads, the rate of deposition and the surface roughness of the finished component [35].

WAAM of various types of SSs and how process parameters and chemical composition affect the microstructure, corrosion behavior and mechanical properties is an ongoing study worldwide. The effect of certain process parameters on macroscopic characteristics, microstructure and mechanical properties of some SSs has been documented [36]. However, for WAAM of SSs to be properly implemented in industry more studies are required on fatigue and corrosion behavior [36].

1.3 Heat Treatment

The idea of heat treatment and quenching started with the early production of iron, which goes as far back as 1400-1200 BC. Through the years the heat treatment and quenching methods were established by blacksmiths through empirical research and experimentation. However, it was not until approximately 1850 AD that the effects of quenchants and alloying elements were quantified, and even later that hardenability, martensite formation and quenching mechanisms were identified [37]. Iron possesses an allotropic property which allows its crystal structure to change with temperature, providing steels and SSs with the ability to form ferrite, austenite, and martensite phases. The various alloying elements that can be added to iron, carbon in particular, all play a role in determining at what temperatures the phase transformations take place [38]. The microstructure of steels can be altered positively by proper heat treatment procedures, which can benefit mechanical and corrosion properties as these are highly dependent on the microstructural phases [38, 39]. Depending on the heat treatment, SSs can be provided with protection to wear and corrosion resistance throughout the cross-section of the part, making them less dependent on protective coating with limited life [40]. Undesired mechanical and corrosion properties along with residual stress can remain in a component after fabrication, heat treatment is able to restore these properties and eliminate the residual stress [40].

Phase diagrams are an important tool to identify which phases form at what temperatures for SSs. They are therefore also important in determining heat treatment temperatures for these alloys. For martensitic SS, which can be considered as Fe-Cr-C alloys, it is essential for austenite to form as this is the phase that transforms into martensite. An increase in the content of the ferrite stabilizing element chromium means that an increase in the austenite stabilizing element carbon is needed to counter the ferrite transformation [41]. Figure 1.5a and 1.5b show the pseudo-binary phase diagrams of 13Cr and 17Cr martensitic SSs, respectively. In the phase

diagram ferrite, austenite, delta ferrite, $M_{23}C_6$, and M_7C_3 are annotated by α, γ, δ, C_1, and C_2, respectively [12]. It can be seen that an increase in chromium content of the alloy leads to a shift towards higher carbon content for the single-phase austenite region.

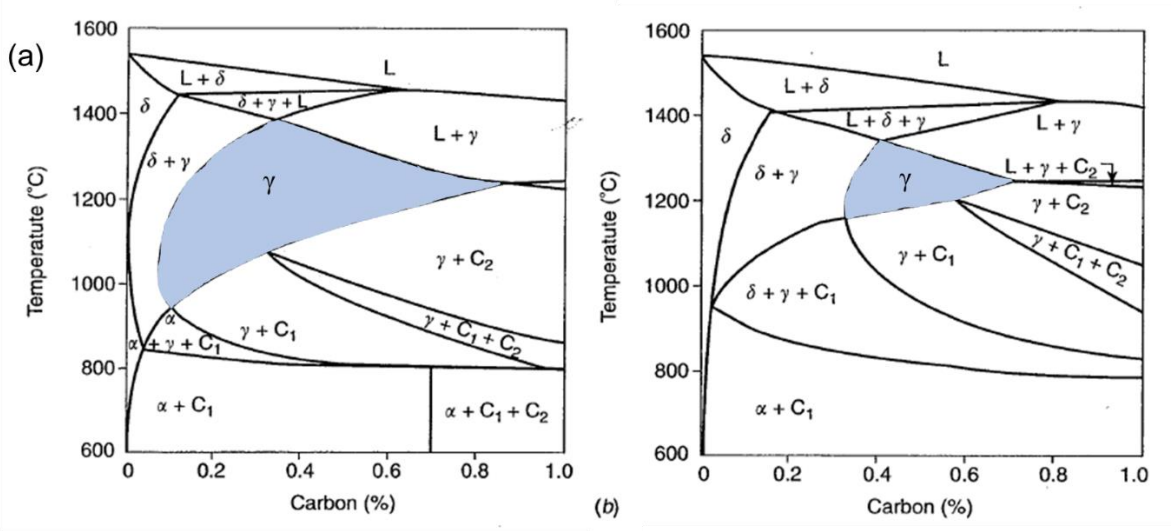

Figure 1.5. Fe-Cr-C pseudobinary phase diagrams of (a) 13Cr and (b) 17Cr martensitic SS. Single-phase austenite regions are marked with blue (Modified from [12]).

Austenitizing involves heating the martensitic SS to a temperature where the austenite phase transformation occurs, and carbide precipitates are fully or partially dissolved [42]. Higher temperatures used during austenitizing provides better mechanical and corrosion properties, however this increases the risk of decarburization, excessive grain growth, retained austenite, quench cracking and brittleness [40]. Subsequent steps in the heat treatment of martensitic SSs include cooling from austenitizing temperatures to transform the austenite into martensite, followed by tempering to improve toughness and ductility [41, 42]. Higher austenitizing temperatures have been shown to cause a higher dissolution rate of carbide precipitates, leading to a higher carbon content in the austenite matrix and ultimately higher retained austenite contents [42]. From the austenitizing temperature martensitic SSs are quenched in either air or oil. Oil quenching helps prevent the formation of carbide precipitation in the grain boundaries and air cooling is better for avoiding distortion of complex regions of a part [41, 43]. Martensite

formed as a result of quenching from austenitizing temperatures is hard, brittle, and prone to cracking due to a high level of internal stresses. Tempering is often applied to increase toughness and elongation at the cost of hardness [43]. Figure 1.6 shows how hardness is affected by tempering temperature in a 12Cr martensitic SS with 0.14 % carbon.

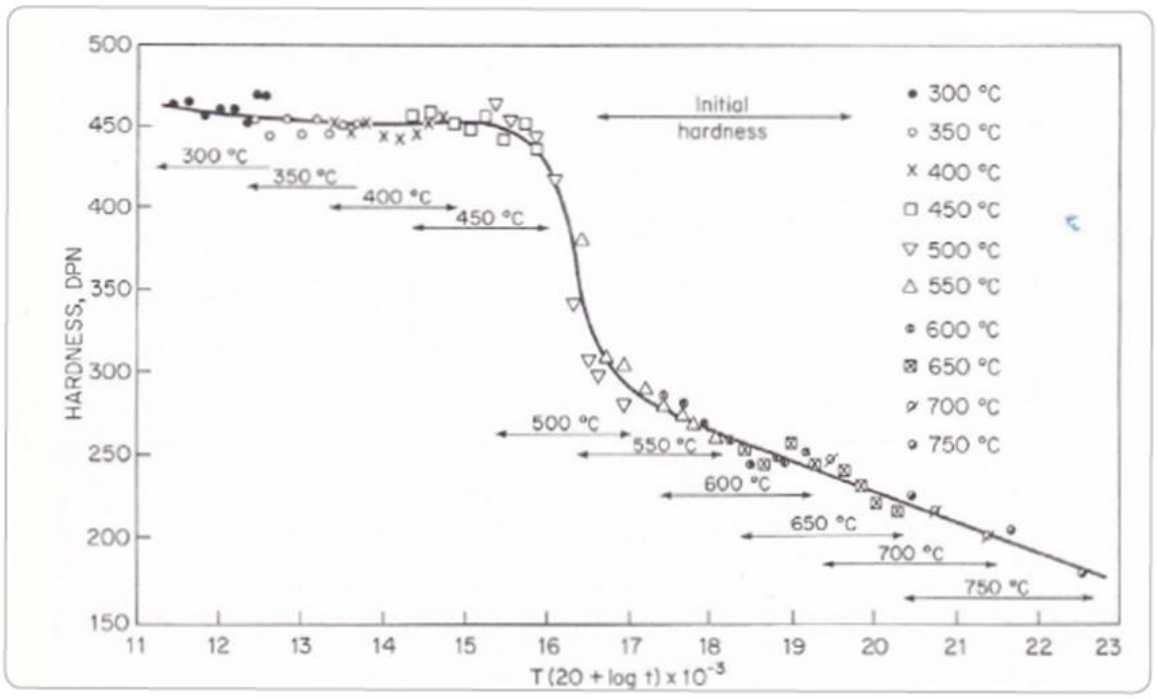

Figure 1.6. Graph showing the change in hardness with increased tempering temperature for a 12Cr martensitic SS with 0.14 % carbon [43].

1.4. Motivation and Research objectives

As WAAM can produce large components rapidly it is desirable for production companies to understand the properties of the fabricated parts. Varying the process parameters used for deposition of DED-fabricated SS parts can change their microstructure and mechanical properties in as-printed condition [44]. Anisotropy and the formation of various secondary phases, such as delta ferrite and retained austenite, have been documented in WAAM fabricated SS parts [45–47]. The effects of microconstituents on the mechanical properties of SS parts in as-printed condition need to be studied more extensively to properly understand the WAAM process.

SS parts produced by WAAM can experience residual stress and distortion, which requires a post-fabrication heat treatment to eliminate [36]. Heat treatment of SS parts has been shown to promote the growth of different types of carbide precipitates in the microstructure [48]. It is generally agreed upon that carbide precipitates formed in SSs adversely affect the corrosion resistance by draining Cr from the matrix [49]. Application of different heat treatment temperatures and times lead to the formation of different microstructural phases, capable of affecting corrosion performance [50–53]. A greater understanding of how heat treatment parameters affect the microstructure of the fabricated SS part is required for understanding its effect on the corrosion resistance.

As a result, this thesis aims to answer the following questions:

1. What is the effect of the WAAM process on the microstructural evolution and mechanical properties of a 13Cr martensitic SS in as-printed condition?
2. What are the effects of various post-fabrication heat treatment temperatures on the microstructure and corrosion behavior of the WAAM 13Cr martensitic SS part?

3. What are the effects of various tempering times on the microstructure and corrosion behavior of the WAAM 13Cr martensitic SS part?

With these questions in mind, the investigation of a 13Cr martensitic SS part in as-printed condition and after post-fabrication processing was performed and reported in this thesis.

1.5. Organization of the thesis

This is a thesis written in a manuscript format (paper based). All papers are currently either under internal review or peer review with journal papers or conferences.

The following three chapters presented in this study are on a WAAM AISI 420 martensitic SS thin-wall part. The second chapter investigates the as-printed microstructure and mechanical properties and determine the effect of the microstructural phases formed during fabrication on these properties. In the third chapter a post-fabrication heat treatment is applied to the thin-wall part. The optimal austenitizing and tempering temperatures with regards to corrosion resistance are determined by microstructural examining and electrochemical testing. The third and final chapter will further look into the tempering temperature that provided the best corrosion behavior after the heat treatment process. Samples exposed to the same tempering temperature for different time intervals are investigated by microstructural examination and electrochemical testing.

Chapter 2

Wire arc additive manufacturing of AISI 420 martensitic stainless steel: on as-printed microstructure and mechanical properties

Preface

I am the first and corresponding author of this paper. Along with the co-authors, Salar Salahi, Mostafa Kazemipour, and Dr. Ali Nasiri, I investigate the microstructure and mechanical properties of a wire arc additively manufactured 13Cr (AISI 420) martensitic stainless steel part in as-printed condition. I prepared methodology, performed experiments, analysed the data, and prepared the first draft of the manuscript, and given the co-authors' feedback I revised the paper. Mostafa Kazemipour and Salar Salahi contributed with experiments and data analysis, and Dr. Ali Nasiri contributed with conceptualization, design, project administration, and supervision, review and editing of the manuscript.

Abstract

In this study, the microstructure, and mechanical properties of an AISI 420 martensitic stainless steel (MSS) multilayer thin wall part produced by wire arc additive manufacturing (WAAM) were investigated. In order to characterize the microstructure and mechanical properties of different zones of the printed wall, samples were prepared from the bottom, middle and top regions along the building direction of the part. Utilization of scanning electron microscopy (SEM) along with electron backscatter diffraction (EBSD) and X-ray diffraction (XRD) analyses revealed the formation of a martensitic matrix along with delta ferrite and retained austenite as secondary phases in the as-printed microstructure. The presence of these secondary phases was correlated to the complex thermal history in the deposited layers associated with cyclic re-heating and cooling as subsequent layers were deposited. Higher hardness values were measured for the top region of the fabricated parts since these layers were not exposed to the same in-situ re-heating cycles as the bottom and middle layers. Uniaxial tensile tests along the building (vertical) and deposition (horizontal) directions revealed similar low elongation and high tensile strength for the bottom and middle regions along the horizontal direction and vertical samples. Differently, the samples from the top region fractured at a lower strength and elongation due to their harder nature of untempered martensitic matrix combined with the deteriorating effect of a significantly higher amount of delta ferrite in the top region.

1. Introduction

The advancements in the field of metal additive manufacturing (AM) in recent years have given various industries the opportunity of rapid fabrication of intricate components in an incremental layer-by-layer fashion [45]. As compared to the subtractive fabrication methods, *e.g*. casting, forming or machining, AM is capable of producing intricate components with fewer design complications and more economically efficient due to the lower material waste, leading to a shorter lead time [54]. Although there are multiple ways of producing parts through metal AM, the two commonly used techniques are powder bed fusion (PBF) and direct energy deposition (DED). The DED techniques cannot compete with the PBF capabilities in fabricating complex components, however, they are able to produce significantly larger parts with a less complex design much faster at drastically lower fabrication cost [55]. A common method of DED often termed as wire arc additive manufacturing (WAAM) involves the feeding of the feedstock metal wire at a controlled rate through a welding torch-produced arc or plasma, mounted on a multi-axis robotic arm or a CNC-gantry system. As a droplet-based 3D printing method, WAAM is well suited for producing thin-walled components with simple to medium complexity [56]. As compared to the laser-based or electron beam-based AM processes, using electric arc as the heat source in the WAAM contributes to a more moderate rate of heating and cooling during fabrication and can produce parts with fewer defects [57, 58].

Compared to most conventional manufacturing methods, a component produced by the WAAM experiences a more complicated thermal history during fabrication involving multiple cycles of heating and cooling, leading to the formation of a more inhomogeneous solidification structure [27, 59]. Such frequent heating and cooling cycles are attributed to the deposition of subsequent layers during the manufacturing process. Therefore, the obtained microstructure and mechanical properties of a WAAM part are commonly different from its wrought or entirely cast counterpart [60]. The inhomogeneous microstructure and undesirable micro-

constituents in AM fabricated products commonly provoke anisotropic mechanical properties [61], which emphasizes on the need to control the microstructure either during the printing process or through applying appropriate post-printing heat treat cycles [22, 62]. In a recent study by Hejripour *et al*. [46], the yield strength and elongation of samples along the horizontal and building directions for a WAAM fabricated duplex stainless steel (SS) were compared, and a higher yield strength but lower elongation were reported for the horizontal samples. Similar results were obtained by Griffith *et al*. [63] when studying the microstructure and mechanical properties of 316 and 304L SS components produced by laser engineered net shaping, reporting a higher yield strength at the cost of ductility for the horizontal specimens.

The AISI 420 martensitic stainless steel (MSS) is considered a general-purpose alloy and is mainly used in applications where an excellent combination of resistance to corrosion and good mechanical properties are required [64–66]. MSSs usually contain between 11.5 wt.% and 18 wt.% chromium and up to 0.6 wt.% carbon and form a martensitic microstructure when quenched from austenitizing temperatures [42, 67, 68]. The corrosion resistance of SSs in general is associated with the formation of a 1-3 nm thick passive oxide film on the surface of the alloy [69]. Although many other grades of SS can provide better corrosion performance in harsh environments, AISI 420 is the commonly used alloy due to its lower cost [50]. However, there is little published research on the use of the WAAM technology to produce parts using AISI 420 feedstock wire.

The high cooling rate associated with the welding of MSSs can lead to the supercooling of delta ferrite phase during its transformation to austenite, making it possible for delta ferrite to coexist with retained austenite and martensite at room temperature [52, 70, 71]. Baghjari *et al*. [72] studied the laser welding of AISI 420 SS and reported the formation of delta-ferrite along with carbide precipitates in a martensitic matrix. The formation and stabilization of delta-ferrite at room temperature has been also reported in the structure of other grades of AM fabricated

SSs, such as 304 SS, at various heat input levels [73]. Ge *et al*. [27] in their study of a 2Cr13 (containing approximately half the amount of carbon as the alloy in the present study) thin-wall part produced by cold metal transfer (CMT) WAAM reported that the martensite content increases from the bottom of the fabricated wall to the top. The formation of austenite in the microstructure of a WAAM-2Cr13 was also reported in a different study by Ge *et al*. [74], when they used a shorter interlayer dwell time during fabrication.

Implementing the WAAM technology for fabrication of parts from the MSS family and in particular AISI 420 SS is relatively new, and the open literature on this subject is very limited. More detailed studies of the topic are required to clearly elucidate the process-microstructure-performance correlations in the fabricated parts, especially when various modes of metal transfer are adopted during the fabrication process.

This study investigates the microstructural variations along the building direction and the resulting anisotropic mechanical response of an as-printed multi-layer single bead thickness wall of AISI 420 SS produced by the state-of-the-art surface tension transfer (STT) WAAM technology. The mechanical properties of the deposited wall were investigated by microhardness and uniaxial tensile tests, along with fractography of the fractured surfaces of the tensile specimens. The purpose of the performed study was to determine how the complex WAAM thermal history affected the microconstituents formation in the microstructure and their effect on the mechanical properties of the fabricated part.

2. Experimental Procedure

A multi-layer wall with the length, height and thickness of 150, 75 and 10 mm, respectively, was fabricated through the WAAM technology using ER420 SS feedstock wire on a wrought AISI 420 base plate. The illustration of the fabricated wall is shown in Figure 2.1. For fabrication of the wall, a six-axis robotic arm was used for consistent and uniform deposition

of the material. This robotic arm utilized an all-y scanning strategy with alternating directions. The chemical composition of the used wire and base plate and the process parameters used for deposition are displayed in Tables 2.1 and 2.2, respectively.

Table 2.1. Nominal chemical composition of the used feedstock wire and the base metal (all data in wt.%)

Sample	Cr	C	Si	Mn	Ni	Mo	P	S	Cu	V	Fe
AISI-420 Base Metal	12-14	0.15-0.46	0-1	0.4-0.1	-	0-0.1	0-0.04	0-0.03	-	0.3	Bal.
ER-420 Wire	12-14	0.3-0.4	0-1	0-1	0-0.5	0-0.5	0-0.04	0-0.03	0-0.5	-	Bal.

Table 2.2. Process parameters used during deposition of the multi-layer wall.

Wire Feed Speed	Travel Speed	Current	Gas Flow Rate	Arc Voltage	Wire Size
4.06 m/min	0.22 m/min	135 A	45 L/min	29 V	0.11 cm

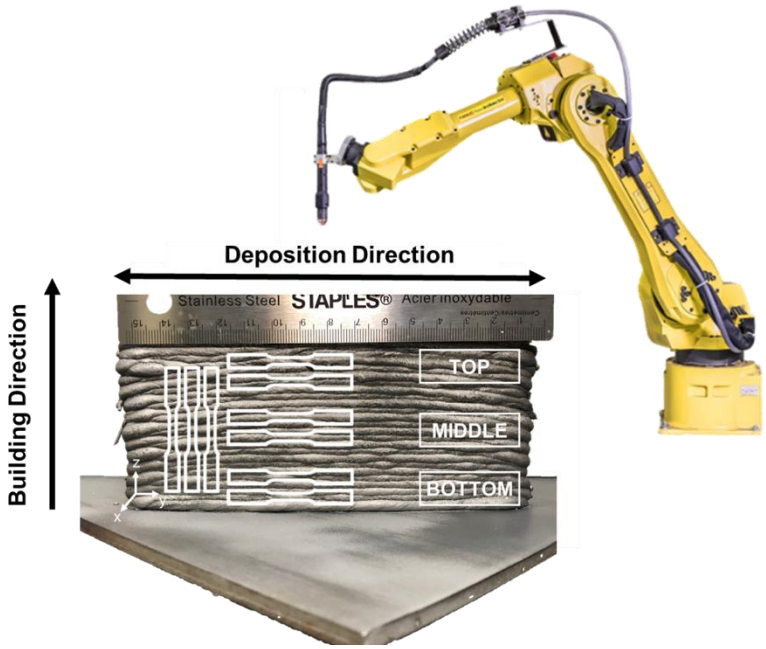

Figure 2.1. Illustration of the WAAM deposited wall and the robot used for the deposition along with some of the locations of the extracted tensile samples and the three investigated regions.

To ensure the consistent interlayer temperature of 200°C prior to the deposition of each layer, the temperature of each newly deposited layer was monitored using a laser thermometer. For characterization of the microstructure and mechanical properties, the wall was divided into three different regions, including the bottom, middle and top areas with the base plate as a reference point (see Figure 2.1). To prepare flat horizontal and vertical tensile samples, the wall was cut from the base plate and ground until a smooth and level surface was achieved, which decreased its thickness to 5 mm. The position of the horizontal and vertical uniaxial tensile test samples with the gauge dimensions of 30 × 10 × 2 mm prepared from the wall, along the deposition and building directions, are illustrated in Figure 2.1. The uniaxial tensile testing of the samples was conducted at the strain rate of 1 mm/min. The displacement data from each sample during tensile testing were gathered using an extensometer attached to the specimen's gauge and the yield strength was calculated using the 0.2% offset method. A minimum of three samples were tested for each region of the wall (bottom, middle, top, and vertical).

Vickers microhardness measurements were also performed covering three regions. The hardness profile included multiple layers within each region, which were large enough to have a center region distinguishable from heat-affected zones and melt pool boundaries. 15 indentations were made for each region of the wall. For characterizing the microstructure, samples from each region were cut, ground, polished, following standard sample preparation procedures for MSS, and etched with Vilella's etchant before being examined by an FEI MLA 650F scanning electron microscope (SEM) to determine the microstructure. The SEM was also equipped with a Bruker energy dispersive X-ray (EDX) analytical system to map

concentrations of the chemical elements and an HKL electron backscatter diffraction (EBSD) system.

The inverse pole figures (IPFs), pole figures (PFs), grain boundary maps, and phase maps were obtained using the EBSD analysis. Only data points with confidence index higher than 0.01 were considered valid in the performed EBSD analysis herein. To post-process the collected EBSD raw data, Channel 5 software was used. X-ray diffraction (XRD) analysis was also conducted using an Ultima-IV XRD diffractometer to determine the phases present in the microstructure. Cu-K_α radiation (λ=1.54Å) within a 2θ-range of 20-100° using 1° min^{-1} scanning rate were the measuring parameters. The MDI JADE 2010 software was used to determine the volume fractions of the phases in each region employing the whole pattern fitting (WPF) technique.

3. Results and Discussion

3.1 Microstructure

3.1.1 SEM analysis

The SEM images taken from the bottom, middle, and the top regions of the fabricated wall are shown in Figure 2.2. Figures 2.2a and d show the micrograph depicting the microstructure of the bottom and middle regions, respectively, revealing a coarse martensitic matrix denoted as α' phase. A noticeable change can be detected in the microstructure of the top region (Figure 2.2g) as compared to the bottom and middle regions. The top region's microstructure contains a high-volume fraction of vermicular shaped delta ferrite denoted as δ as an additional phase formed along the primary austenite grain boundaries embedded in a martensitic matrix. The SEM images shown in Figure 2.2a and d also revealed the formation of a less continuous network of delta ferrite phase (δ), as compared to the top region, along with the martensite. The EDX concentration maps taken from the microstructure of different regions of the fabricated

part also shown in Figure 2.2 confirmed the positions of delta ferrite phase along the interdendritic regions, where higher concentrations of Cr element (a ferrite stabilizing element) and lower concentration of iron as compared to the surrounding matrix were detected.

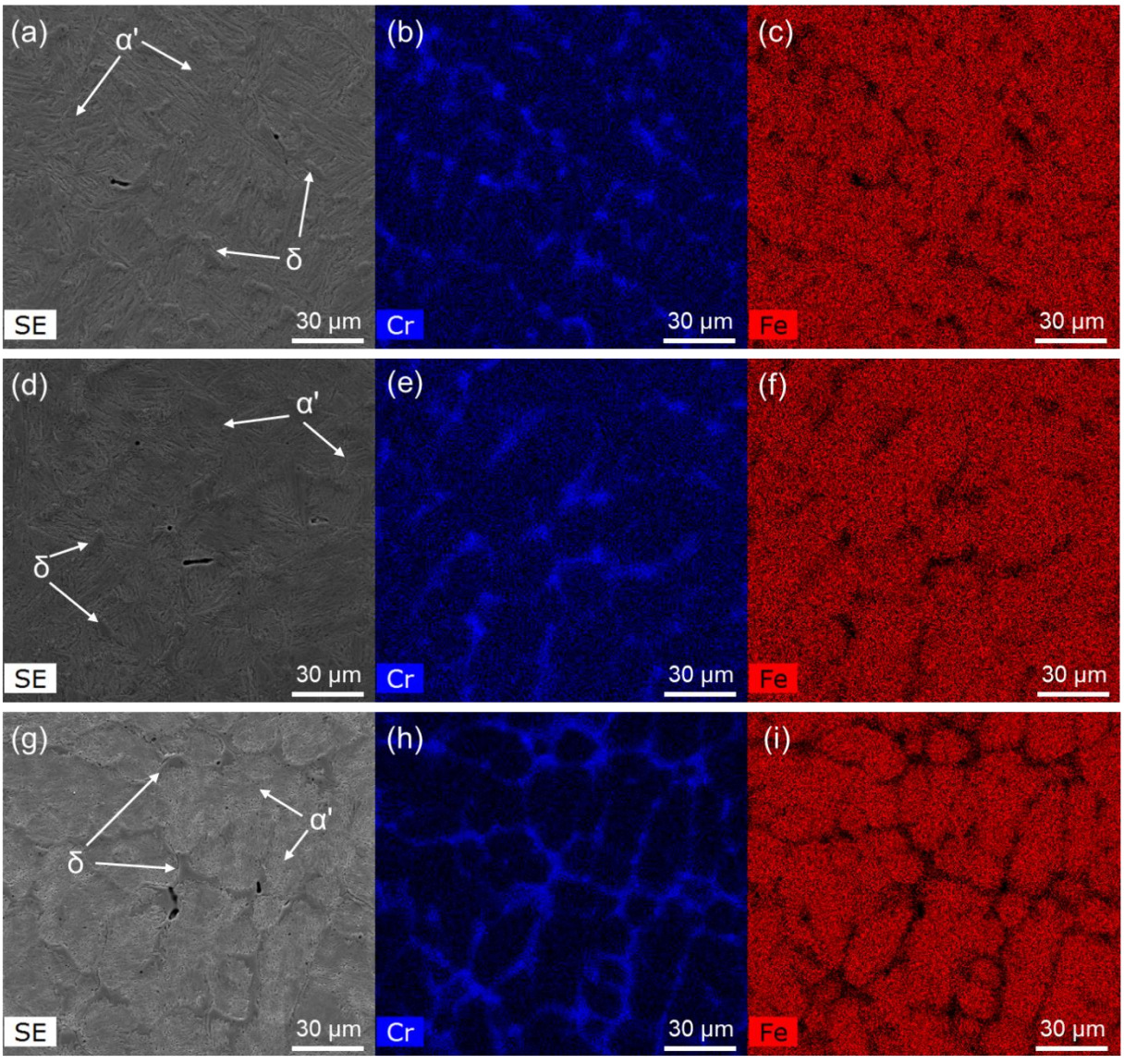

Figure 2.2. SEM images and EDX elemental maps indicating Cr and Fe concentrations taken from the (a-c) bottom, (d-f) middle, and (g-i) top regions of the WAAM fabricated ER420 wall.

Figure 2.3 depicts the Fe-Cr-C pseudo-binary phase diagram for a SS containing 13 wt.% chromium. The solidification process of an AISI 420 SS containing approximately 0.35 wt.% carbon during equilibrium conditions is indicated on the phase diagram and described in equation (1.1), where L, δ, γ, and α correspond to the liquid, delta ferrite, austenite, and ferrite phases, respectively.

$$L \rightarrow L + \delta \rightarrow \delta + \gamma + L \rightarrow \gamma \rightarrow \alpha \tag{1.1}$$

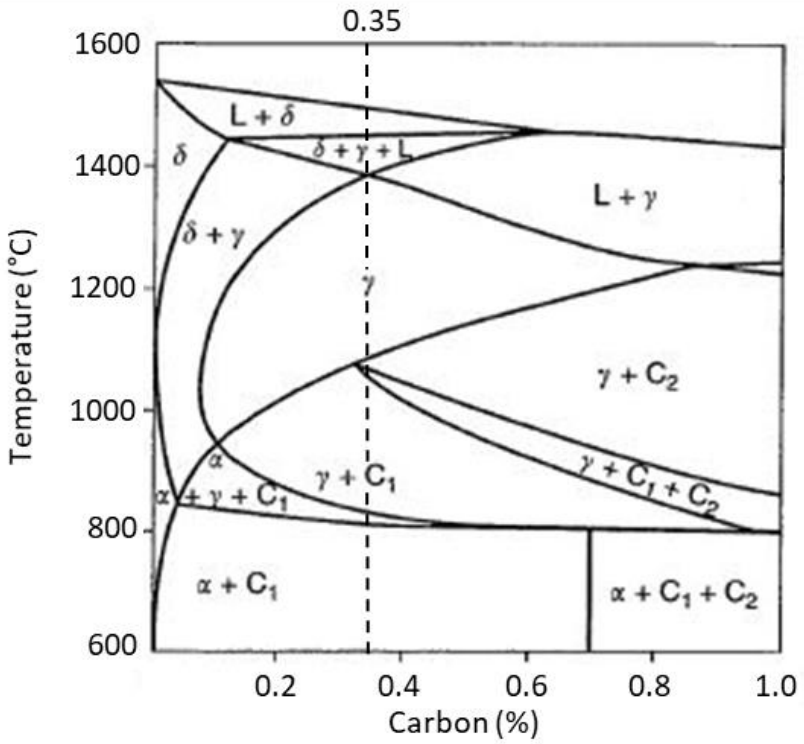

Figure 2.3. Pseudo-binary phase diagram of an MSS containing 13 wt.% chromium with the carbon content in the present study taken as the average of its range (0.35 wt.%) indicated by the dashed line (modified from [12]).

As already mentioned, the WAAM process can resemble a multi-pass arc welding process. Analogously, a non-equilibrium solidification is expected during WAAM ascribed to the high cooling rate associated with the process. Therefore, the equilibrium solidification path shown in Figure 2.3 and equation (1.1) will not be followed strictly during deposition and

solidification of each individual layer of the fabricated wall studied herein. Consequently, instead of obtaining a fully ferritic microstructure in as-printed condition, the high cooling rate of the WAAM leads to the formation of primarily a martensitic matrix [75]. If in the chemical composition of the MSS, the content of ferrite stabilizing elements dominates over the austenite stabilizing elements (the case of ER420), it is possible for high-temperature delta ferrite phase to be retained in the martensitic matrix at room temperature. It has been also reported that very high cooling rates during laser welding can prevent the delta ferrite to austenite transformation [72]. The chemical composition of the feedstock wire used in this study contains a relatively low amount of austenite stabilizers as compared to ferrite stabilizing elements, which allowed for the aforementioned retaining of delta ferrite in the microstructure at room temperature. The presence of delta ferrite in the microstructure of a duplex SS produced by WAAM has been also reported, and the concentration of chromium found in the delta ferrite phase was ~ 5% higher than that of the wire used for deposition [46]. The observed higher content of chromium in the delta ferrite phase formed along the interdendritic regions (~17 wt.% Cr) in this study (seen in Figure 2.2(b,e,h)) corresponds well with these findings. The observed vermicular shaped delta ferrite phase differentiates the detected as-printed microstructure of the fabricated alloy herein compared to that reported in previous studies on WAAM of 13Cr MSSs [27, 74, 76, 77].

The stabilization of retained austenite at room temperature in the microstructure can be justified if the martensite finish (M_f) temperature of the alloy is below the room temperature [78]. The M_f temperature of AISI 420 can be considered to be 150-200°C lower than the martensite start (M_s) temperature [42]. Several correlations for calculation of M_s have been reported in previous studies and are listed in Table 2.3. Using the average values of the provided ranges in Table 2.1 for the chemical composition of the ER420 feedstock wire, the M_s temperature of the alloy was calculated, employing all M_s correlations in Table 2.3. As can be

seen from Table 2.3, the M_f temperature ranges include temperatures below room temperature, confirming that the retained austenite can stay stable in the final as-printed microstructure of this alloy at room temperature.

Table 2.3. Martensite start temperature (M_s) correlation gathered from the literature.

Reference	M_s Correlation	M_s [°C]	M_f [°C]
Irvine *et al.* [81]	$551 - (474C + 33Mn + 11Si + 17Cr + 17Ni + 21Mo + 11W)$	183.6	$[-16.4, 33.6]$
Steven and Haynes [82]	$561 - (474C + 33Mn + 17Cr + 17Ni + 21Mo)$	148.1	$[-51.9, -1.9]$
Andrews [83]	$539 - (423C + 30.4Mn + 12.1Cr + 17.7Ni + 7.5Mo)$	212.2	$[12.2, 62.2]$
Gooch [84]	$540 - (497C + 6.3Mn + 10.8Cr + 36Ni + 46.6Mo)$	201.8	$[1.8, 51.8]$
Self *et al.* [85]	$526 - (354C + 29.7Mn + 31.7Si + 12.5Cr + 17.4Ni + 20.8Mo)$	199.4	$[-0.6, 49.4]$
Higgins [65]	$500 - (333C + 34Mn + 35V + 20Cr + 17Ni + 11Mo + 10Cu + 5W + 15Co - 30Al)$	97.0	$[-103, -53]$

The presence of retained austenite in SS parts produced by AM has been also reported in previous studies [47, 79]. Austenite contents of as high as 57% has been documented in parts of AISI 420 produced by selective laser melting due to exposure to thermal cycling during deposition [79]. It is also reported that WAAM processing parameters can affect the presence and content of retained austenite in the microstructure of 17-4 PH SS [47]. As a result of ambient temperature around the austenite reversion temperature range, the dwelling time between the deposition of each layer can significantly affect the content of retained austenite

in the produced part [74]. As the layers of the manufactured wall in the present study were deposited onto the previously solidified layer at a temperature of 200°C, the fabrication condition herein is analogous to a short interlayer dwelling time. As a new layer is deposited, the heat associated with the deposition affects the underlying layers, with the closer layers experiencing higher temperatures than the deeper underlying layers from the new deposit. Potentially, the closer layers can reach the austenitizing temperatures and consequently their martensite matrix can partially/locally retransform to austenite. This austenite can be partially retained in the martensitic matrix as it cools down [80]. These higher temperatures associated with the deposition of new layers also caused the less continuous network of delta ferrite phase in the bottom and middle regions, as some of the delta ferrite phase in these regions were retransformed to austenite and subsequently transformed into martensite upon cooling.

3.1.2 XRD analysis

The XRD patterns obtained from three regions, *i.e*. the bottom, middle, and the top of the WAAM-ER420 wall can be seen in Figure 2.4. Consistent with the results obtained from the SEM analysis, the XRD spectra revealed austenite peaks alongside the martensite peaks. Four diffraction peaks for each of the two phases were detected, (110), (200), (211) and (220) for martensite and (111), (200), (220) and (311) for austenite. Even though diffraction peaks for alpha ferrite, delta ferrite and martensite are not possible to be distinguished due to their similar lattice axis ratio [86], the SEM analysis results (Figure 2.2) determined that the peaks belonged to both martensite and delta ferrite. The similar XRD patterns found for the bottom and middle regions indicate that the in-situ re-heating effect associated with newer deposited layers have affected these regions equally. Using the WPF technique, the volume fractions of austenite in the bottom, middle and top regions were found to be 17.4%, 18.2%, and 20.6%, respectively, further confirming the retransformation of some austenite to martensite in more frequently tempered bottom layers.

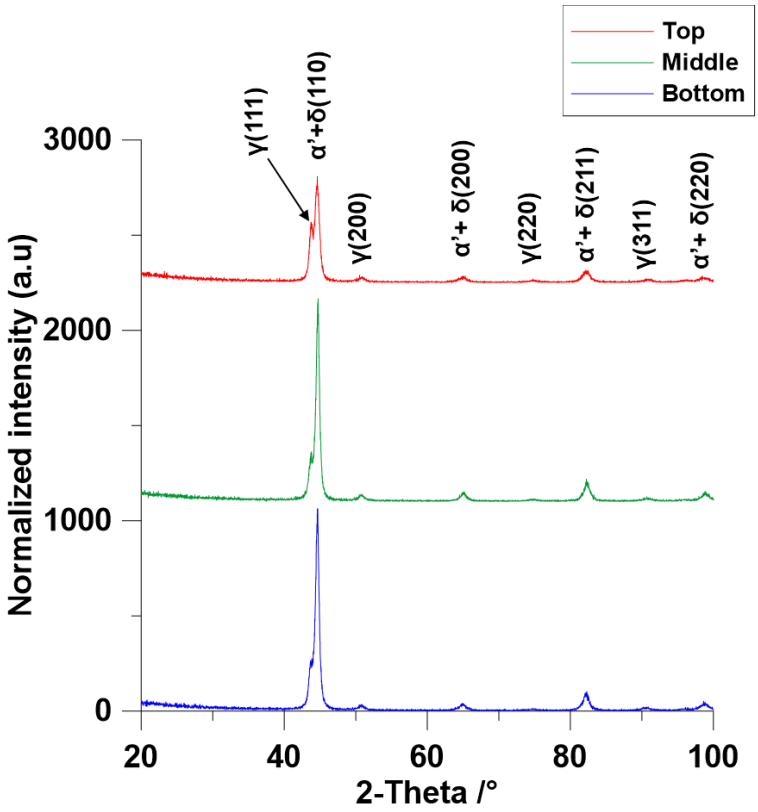

Figure 2.4. XRD patterns of the bottom, middle, and the top regions of the WAAM-ER420 wall with annotated peaks for martensite and delta ferrite (α'+δ) and austenite (γ).

3.1.3. EBSD analysis

Figure 2.5 shows the IPF maps superimposed on grain boundaries maps (Figures 2.5a-c) and phase maps (Figures 2.5d-f) of the as-printed part taken from the bottom, middle, and top regions of the fabricated part, all prepared from the center of each deposited layer and along the building direction (BD). Regardless of the position of the sample along the BD, a lath martensitic structure is formed in all layers (Figures 2.5a-c). The formed martensite laths are mostly aligned with the building direction with relatively coarse structure while randomly oriented blocky martensite are observed as well. Phase maps of different regions are extracted

from the EBSD data and illustrated in Figures 2.5d-f. The body-centered cubic (BCC) structure stands for both the delta ferrite phase and the tempered martensitic laths, formed in the structure. Although making a distinction between the ferrite and martensitic phase is not practical through EBSD analysis, it is observed that the fraction of martensite phase remains relatively constant in all regions. A significant fraction of the retained austenite phase with face-centered cubic (FCC) structure is distinguished in the phase maps of all regions (~11%). Retained austenite phase is observed to distribute randomly in the structure and no significant change in the volume fraction of the austenite phase was detected from the bottom to the top layers.

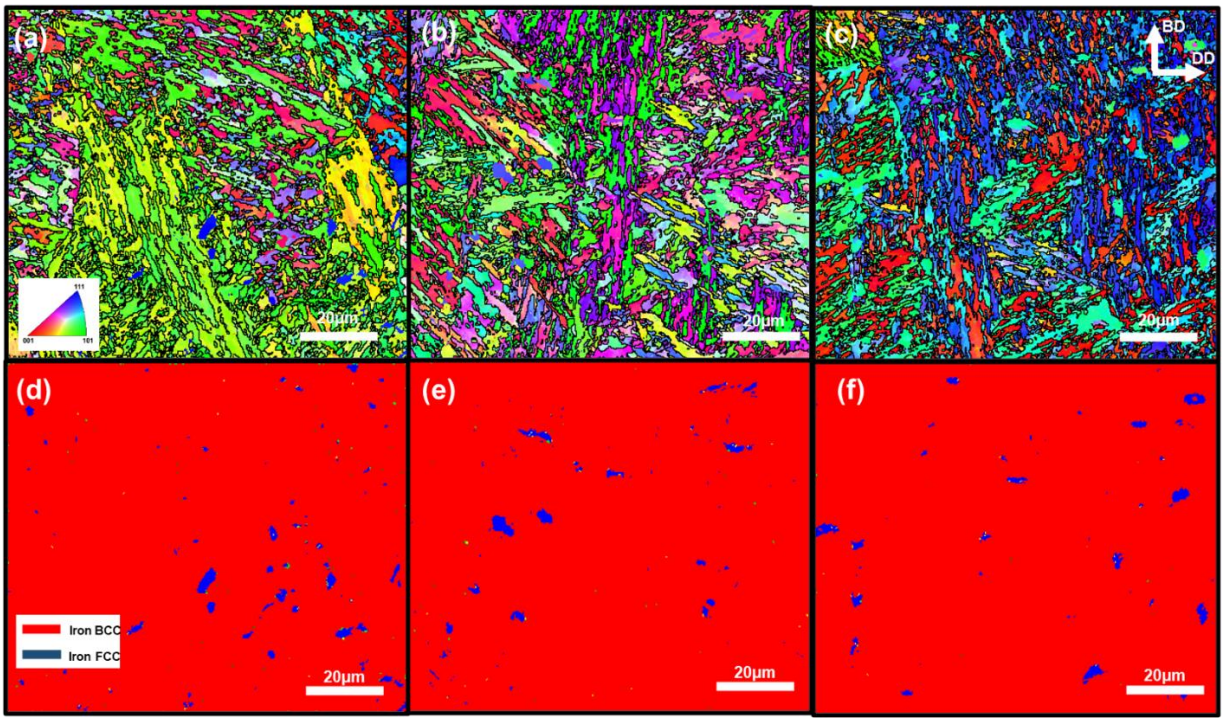

Figure 2.5. Inverse pole figure and grain boundary maps for the (a) bottom, (b) middle, and (c) top regions of the deposited wall, EBSD phase distribution map of the (d) bottom, (e) middle, and (f) top regions.

The resulting pole figures of the formed BCC phase (the tempered martensite laths combined with the delta ferrite phase) and FCC phase (the retained austenite) in the structures of the bottom, middle, and top samples for planes of {100}, {110}, and {111} are shown in Figure 2.6. A strong cubic texture with few pole components is observed for {100} and {111} family of planes of the BCC structure for the bottom, middle and top layers. The detected strong alignment of the {100} poles implies the formation of a strong texture during the solidification process [87–89] and the subsequent multi-steps heat treatment cycles associated with the deposition process. There are also misalignments between the detected {100}<100> texture and the building direction of all three samples, ascribed to the fact that the epitaxial growth direction of the grains (aligned with the <001> direction) is expected to be perpendicular to the melt pool boundaries, which are not necessarily perpendicular to the building direction. A similar misalignment between the grain growth direction and the building direction of AM fabricated parts have been reported in previous studies [90–93]. A single high-intensity pole is observed for the {110}, the most close-packed plane in the BCC phase, which is relatively aligned with the deposition direction (DD), in all regions of the deposited wall. This can potentially facilitate the plastic deformation along the deposition direction of the fabricated wall, if the microstructure of sample can accommodate some degree of plastic strain.

A significantly strong texture was detected for the retained austenite (the FCC phase) in {100} planes at all regions, representing the strong texture in the primary austenite grains in each region with some degree of misorientation relative to the building direction, consistent with the {100} PF of the BCC phase. Overall, the EBSD analysis of the bottom, middle, and the top layers exhibited nearly the same crystallographic orientation, indicating similar distribution of texture for both martensite and retained austenite phases from the bottom to the top regions of the fabricated wall.

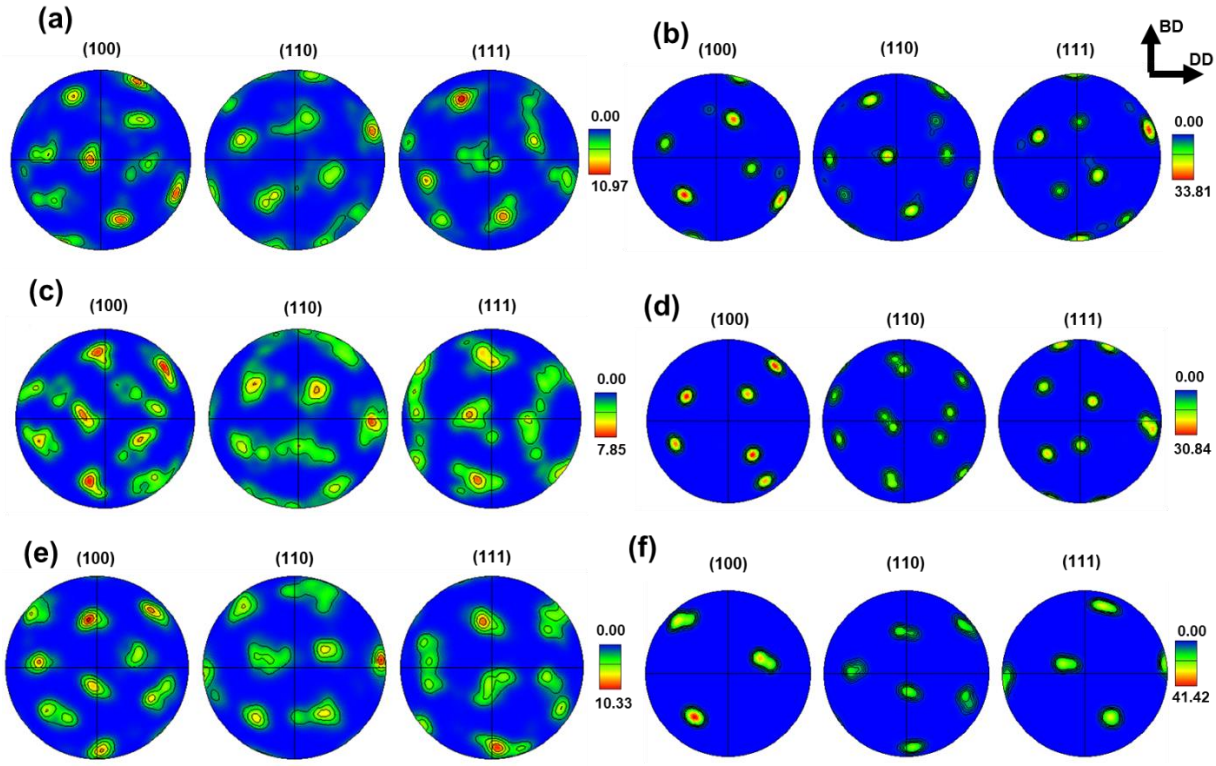

Figure 2.6. PF of the martensite phase formed in the (a) bottom, (c) middle, and (e) top regions, PF of the austenite phase formed in the (b) bottom, (d) middle, and (f) top regions.

3.2 Mechanical Properties

3.2.1. Hardness

Figure 2.7 depicts the average Vickers hardness values of three different regions of the as-printed wall. Multiple indentations were taken from three layers located within each of the three investigated regions. As can be seen from Figure 2.7, a significant increase in hardness was detected for the top region. The hardness value of 732±36.3 HV was measured for the top region, as compared to 620±36.3 HV and 637±42.7 HV for the bottom and middle regions, respectively. A similar trend in the hardness values of the WAAM fabricated 13Cr SS part along the building direction was reported in an earlier study [77]. A higher hardness value for the last deposited layer was also noted for a WAAM fabricated Inconel 625 [94]. The higher hardness values in the final layers can result from the fact that these layers have undergone a smaller number of in-situ re-heating cycles than their underlying layers. Low tempering

temperatures of 300°C have been reported not to affect the hardness of the 13Cr SS material when tempering for 2.5 h, while higher tempering temperatures of 550°C and 700°C lowered the hardness [95].

As already stated, the temperature of a specific underlying layer is periodically reheated as new layers are deposited on its top. At a certain point, the temperature of this layer no longer reaches the sufficient temperature required for the stress relieving and subsequent tempering of the martensitic matrix and consequently, the hardness stabilizes, approximately around 450°C [96]. However, for the top layers the number of in-situ re-heating cycles are lower than the middle or the bottom layers, resulting in the formation of harder top layers in as-printed condition [80].

A higher volume fraction of retained austenite has been also reported to lower the hardness in SS family [52, 97]. However, due to the lack of sufficient localized re-heating treatment in the top layers and the homogeneous distribution of retained austenite from the bottom to the top layers, the formation of retained austenite in the WAAM fabricated AISI 420 SS wall in this study did not seem to be the dictating factor in controlling the as-printed hardness of the alloy.

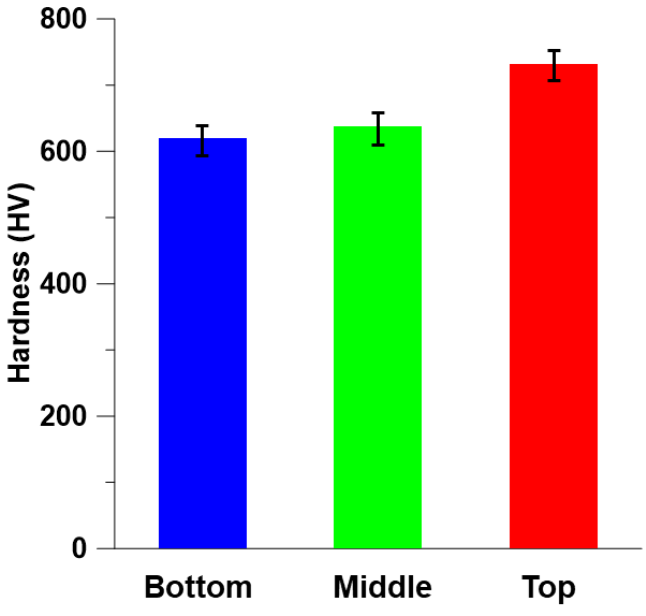

Figure 2.7. Vickers microhardness results of the bottom, middle and top regions of the as-printed wall.

3.2.2. Tensile Properties

Figure 2.8 shows the stress-strain graphs obtained from uniaxial tensile testing of the samples taken from the horizontal direction (deposition direction) in the bottom, middle, and top regions along with the building direction denoted as vertical. As can be observed from the graphs, the mechanical properties of the fabricated part under uniaxial tensile loading seems to be very consistent at the bottom and middle regions along both horizontal and vertical directions with comparable values of fracture strength and elongation, suggesting an isotropic response in the mechanical properties. However, the horizontal sample from the top region (Horizontal-Top) differs from the other three by demonstrating lower properties, fracturing at both lower strength and elongation. The extracted values of the ultimate tensile strength (UTS), elongation, and yield strength (YS) of all tested samples are summarized in Table 2.4. None of the samples experienced necking before fracture, indicating that all samples fractured when reached to their UTS points. Consistent with the observed more brittle response of the Horizontal-Top sample herein, Ge *et al*. [27] reported a more brittle fracture for the top layer of a CMT WAAM-2Cr13 thin wall part than the underlying layers as a result of the formed fully martensitic microstructure in the top layer.

It is also worth noting that retained austenite can transform into martensite during uniaxial loading, leading to an increase in strength and ductility for SS alloys, known as transformation induced plasticity (TRIP) [98]. Random crystallographic texture has been reported to promote TRIP during uniaxial tension for austenitic steels [99]. However, even though the samples in the present study show high strength, the fracture mode of the samples is predominantly brittle, indicating little to no improved plasticity induced by the transformation of retained austenite to martensite. The similarity of the obtained EBSD results for all regions implies that

solidification induced texture in the fabricated samples is not the driving force for the top region's distinct mechanical properties.

Delta ferrite has been also reported to have a positive impact on elongation, while deteriorating the overall strength of MSSs [100]. A high amount of retained delta ferrite in the microstructure has been shown to accelerate the cracking of AISI 420 SS weld [101]. Therefore, the harder nature of less tempered martensite in the top layers accompanied with their higher content of delta ferrite have resulted in the lower strength and more brittle fracture of the top region under uniaxial tensile loading compared with the other regions.

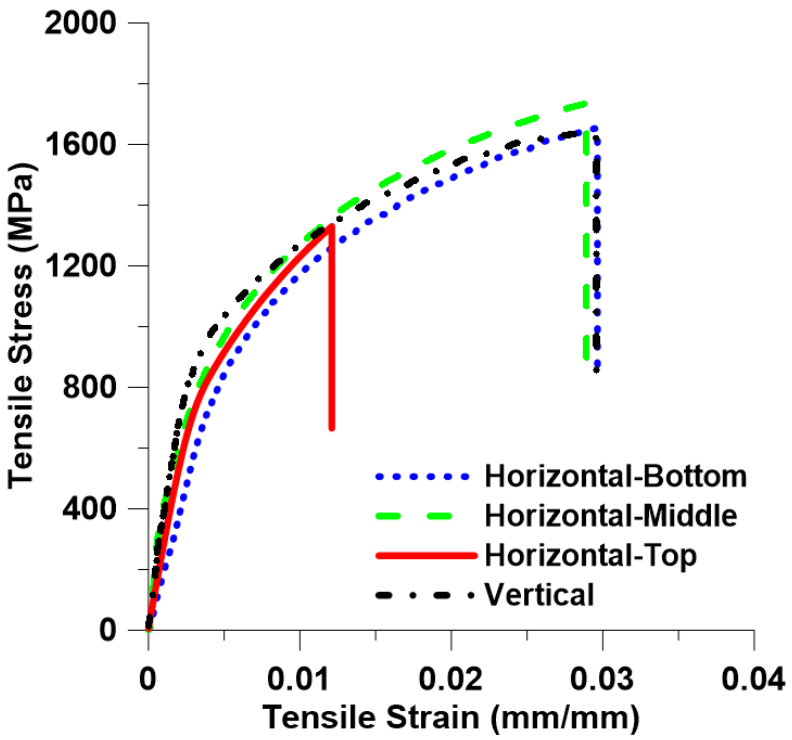

Figure 2.8. Stress-strain graphs of the horizontal samples machined from the bottom, middle, and the top regions of the fabricated wall and the vertical tensile specimens.

Table 2.3. Tensile test values for the horizontal samples from the bottom, middle, and the top regions, and the vertical samples.

Sample	YS (MPa)	UTS (MPa)	Elongation (%)
Horizontal-Bottom	987 ± 26.2	1654 ±43.8	2.97 ± 0.24
Horizontal-Middle	933 ± 24.7	1733 ± 45.9	2.89 ± 0.24
Horizontal-Top	907 ± 24.0	1330 ± 35.2	1.21 ± 0.10
Vertical	1027 ± 27.2	1633 ± 43.3	2.96 ± 0.24

3.2.3. Fractography

Figure 2.9 shows the SEM images depicting the fractured surfaces of the vertical and horizontal tensile samples from the bottom, middle and top regions. Cleavage facets and dimples indicated by the arrows in the lower magnification images can be seen on all fractured surfaces, indicating that a mixed-mode brittle and ductile fractures has occurred. Higher magnification images of the dimpled areas also revealed the presence of inclusion particles at the center of the dimples. Furthermore, the dimples formed on the fractured surface of the top layer were found to be shallower than those on the other samples, consistent with the measured lower plastic strain for the horizontal-top sample.

Similar mixed-mode fractures at a relatively low elongation of 2% have been reported for 13Cr SS alloy tempered at 300°C [95]. Previous studies have also shown similar variations of fracture modes from ductile to mixed and brittle modes from the bottom to the middle and top regions, respectively, of a CMT WAAM fabricated 2Cr13 part [27]. Inclusions, on the other hand, can lead to the formation of voids, which can affect the fracture process of a material [102]. Similar inclusion particles were found on the fractured surfaces of tensile specimens for a Cr-Ni SS produced by both single- and double-wire feed plasma arc AM [103]. An increasing

amount of inclusions can facilitate voids nucleation, which can lead to a decreasing active load area for the specimen under tension, ultimately resulting in a premature fracture [102]. Contrarily, a high number of nucleation sites for micro-voids can delay the fracture, thus increasing the ductility of the material [104].

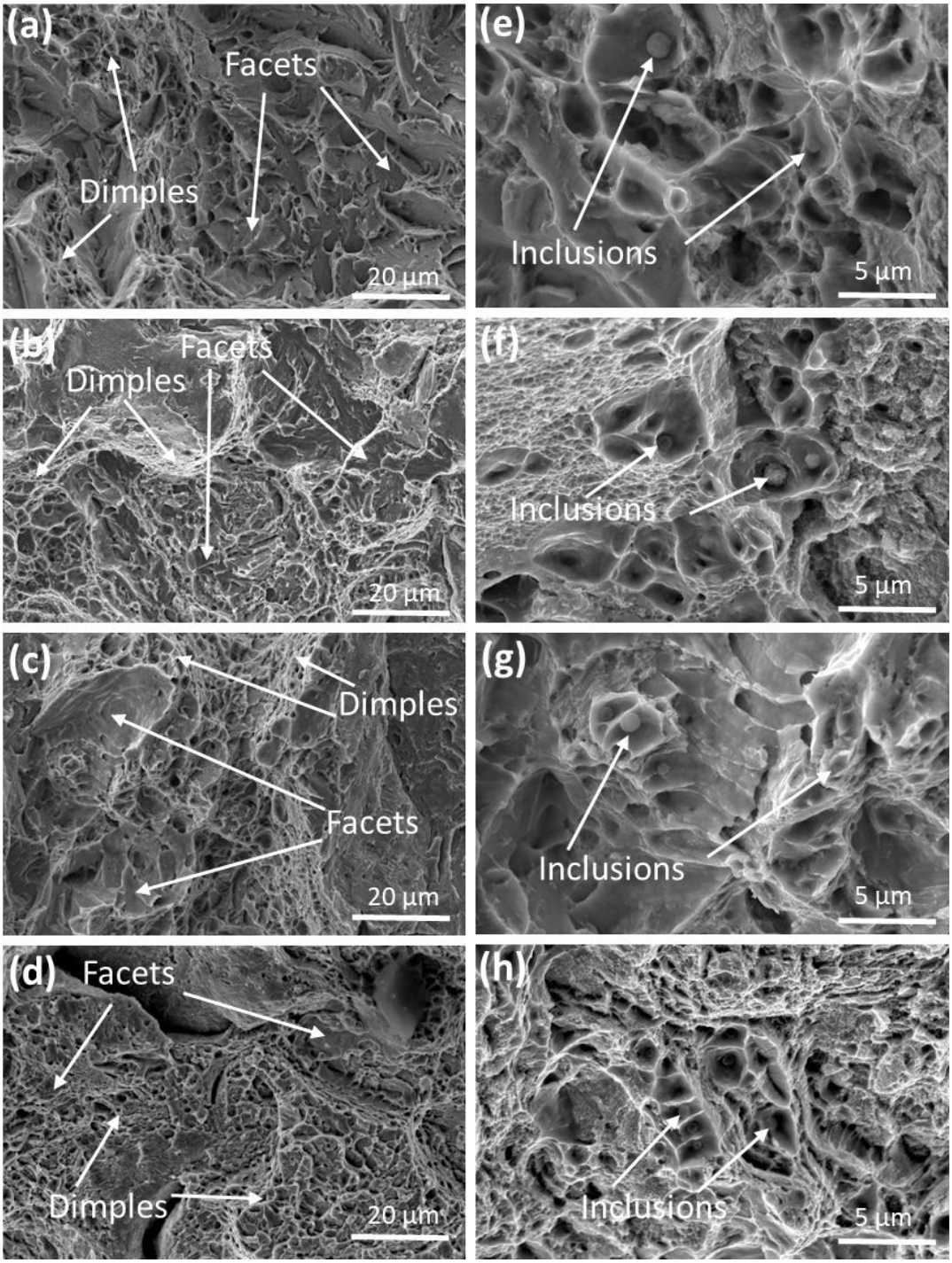

Figure 2.9. SEM images of the fractured surfaces of the tensile samples showing a mixed-mode fracture along with the presence of inclusions at the center of the dimples. (a,e), (b,f), (c,g) and (d,h) correspond to the horizontal bottom, middle, top and vertical samples, respectively.

4. Conclusions

The present study investigated the microstructure and mechanical properties of an AISI 420 multi-layer thin wall part fabricated using WAAM technology. The following conclusions can be made:

1. The as-printed wall revealed a multi-phase microstructure consisting of a martensitic matrix along with secondary retained austenite and delta ferrite phases. The stability of delta ferrite at room temperature was correlated to high cooling rates during solidification combined with the high content of ferrite stabilizing elements, such as chromium, in the alloy.
2. The morphology of delta ferrite phase in the top region varied from the other regions and was characterized by having a vermicular shape morphology formed along the primary austenite grain boundaries as compared to the less continuous network of delta ferrite formed in lower regions. This was due to the heat from newly deposited layers, retransforming a portion of the delta ferrite to austenite during heating and ultimately transforming to martensite upon cooling.
3. The lower M_f temperature of the alloy than the room temperature led to the stability of retained austenite in the microstructure at room temperature.
4. Significantly higher hardness values were found for the top layers compared with the bottom and middle layers, which both exhibited similar hardness values. The increase in hardness at top layers was observed due to the lack of sufficient in-situ re-heating treatment from above-deposited layers.

5. The high hardness values of the deposited wall resulted in high strength and low elongation fractures under uniaxial tensile loading. The top region along the deposition direction fractured at lower elongation and strength than the horizontal bottom, middle and vertical samples, which all revealed a similar mechanical response under uniaxial tension. The measured texture of the fabricated sample at different regions was found to be relatively the same, suggesting that the detected higher amount of delta ferrite phase along with the harder nature of the formed martensite in the top region were the determining factors in controlling the lower tensile properties of the top layer.
6. All tensile specimens experienced a mixed mode fracture with inclusion particles present inside the formed dimples. These particles contributed to the brittle nature of the fracture by decreasing the active load area of the specimen under tension.

Chapter 3

Beneficiary effect of tempering process on the corrosion performance of wire arc additively manufactured 420 martensitic stainless steel

Preface

I am the first and corresponding author of this paper. Along with the co-authors, Salar Salahi, Mahya Ghaffari, Alireza Vahedi Nemani, and Dr. Ali Nasiri, I investigate the effects of tempering temperatures on the microstructure and corrosion behavior of a wire arc additively manufactured 13Cr (AISI 420) martensitic stainless steel part. I prepared methodology, performed experiments, analysed the data, and prepared the first draft of the manuscript, and given the co-authors' feedback I revised the paper. Salar Salahi, Mahya Ghaffari, and Alireza Vahedi Nemani contributed with experiments and data analysis, and Dr. Ali Nasiri contributed with conceptualization, design, project administration, and supervision, review and editing of the manuscript.

Abstract

In the present work, heat treatment of 420 martensitic stainless steel (MSS) fabricated by wire arc additive manufacturing (WAAM) was performed to improve the corrosion resistance of the material in comparison with the as-printed condition. In order to modify the microstructure and improve the corrosion performance, different heat treatment cycles were applied to the as-printed sample. The heat treatment cycles involved austenitizing for 30 min in different temperatures, including 950, 1050, and 1150°C followed by air cooling. Subsequently, a 2 h tempering treatment was conducted with tempering temperatures of 300°C, 400°C, 500°C and 600°C, followed by cooling in still air. Microstructural characterizations revealed that the austenitizing treatment led to the removal of retained austenite and delta ferrite, while the tempering process resulted in the precipitation of a variety of carbide particles at different tempering temperatures. Electrochemical tests performed in an aerated 3.5 wt. % NaCl solution showed that the sample tempered at 400°C has the highest corrosion resistance, while tempering at 500°C led to the worst corrosion performance. A stable passive layer was able to form for the sample tempered at 400°C due to the similar chemical composition of the formed carbide precipitates and its matrix. However, the 500°C sample was unable to form a passive layer due to the size and chemical composition of the carbide precipitates existing within its microstructure, resulting in an active surface.

1. Introduction

Metal additive manufacturing (AM) is a layer by layer process widely used to fabricate 3D-objects by joining processes with a high deposition rate, low equipment cost and material waste, which is superior to conventional subtractive fabrication methods [54, 105]. Using a 3D-model of the desired end-product from a computer aided design file, components with complex shapes and geometries can be fabricated by different additive manufacturing methods [56, 106]. Two of the main metal AM methods include powder bed fusion (PBF) and direct energy deposition (DED), where PBF uses metal powder as the feedstock material, and the DED method can utilize a wire beside the powder [54]. PBF is mostly desirable for fabricating parts with a complex geometry, while DED has a high deposition rate being able to fabricate larger components more time efficient than PBF [55]. DED using a feedstock wire being melted upon deposition by an arc can produce parts with satisfactory mechanical properties and a controlled microstructure [45, 55]. Wire arc additive manufacturing (WAAM) is one of the most well-known DED methods, where a multi-axis robotic arm deposits a wire which is fed through its nozzle onto a substrate [59]. The deposition of multiple incremental layers of a ferrous alloy using WAAM can result in a complex thermal history leading to an inhomogeneous microstructure in the as-printed condition [44, 107], which can be eliminated by applying a proper post-fabrication heat treatment cycle [58, 92] .

420 alloy containing approximately 13 wt.% Cr is a martensitic stainless steel (MSS) considered to have excellent mechanical properties and a moderate corrosion resistance, making it a general-purpose material [64, 65]. This alloy has a wide range of applications due to its potential tendency to be microstructurally altered by application of heat treatment [108]. The nature of the alloy's corrosion resistance comes from a 3-5 mm thick surface layer consisting of Fe and Cr which forms a passive film on the surface of the metal [69]. However**,** MSSs are prone to pitting and intergranular corrosion where a multiphase microstructure

including undesirable micro-constituents such as delta ferrite, is present [109–111]. Wen et al. [111] reported on how linear heat input during WAAM affected the microstructure and corrosion behavior of an austenitic stainless steel and found that delta ferrite phase had a negative detrimental impact on the corrosion resistance of the alloy. In a previous work by the authors of the present study [71], it was found that the presence of residual delta ferrite in the microstructure of the as-printed WAAM 420 sample prevented passivation behavior as a result of a high degree of sensitization around delta ferrite phases, leading to Cr-depleted zones with a weak passive layer.

The chemical composition of MSSs causes the formation of a martensitic matrix upon cooling in air, meaning that the hardenability of MSSs are high [112]. The carbon content of the alloy affects the hardenability of MSSs, and also heat treatment can have a significant impact on the change in MSS's properties [42, 112, 113]. Bonagani *et al.* [48, 95] investigated the effect of different tempering temperatures on a MSS, and found that the tempering temperature of 550°C was the most detrimental due to hydrogen embrittlement and pitting potential. Tavares *et al.* [114] studied the intergranular corrosion of 17-4PH SS and found that an increase in aging temperature resulted in an increasing susceptibility to intergranular corrosion of the alloy, resulting from a higher degree of sensitization.

As mentioned earlier, WAAM 420 alloy showed poor corrosion behavior in the as-printed condition [71], which can potentially be modified through implementing a proper post-printing heat treatment cycle. Therefore, in this study, different heat treatment cycles consisting of austenitizing and tempering at different temperatures were performed on as-printed samples of 420 alloy fabricated by WAAM. Microstructural characterizations along with electrochemical testing on the different heat treated samples were compared and contrasted with the as-printed material to study the effect of heat treatment on the corrosion behavior and microstructure of WAAM 420 MSS.

2. Experimental procedure

2.1. Materials and fabrication process

In this experiment, WAAM technique was used to deposit a 420 MSS multi-layer thin-wall component on an AISI 420 plate as the substrate. The nominal chemical composition of the feedstock material (ER420 solid wire) and the substrate (AISI 420 plate) are listed in Table 3.1. The microstructural features and mechanical integrity of the interfacial bonding between the as-printed part and the substrate was characterised in a previous work [91]. The fabrication unit was equipped with an external wire feeder connected to a GMAW torch mounted on a six-axis robotic arm which utilized an all-y scanning strategy with alternating directions. The process parameters included a wire feed speed of 160 inches/min, a travel speed of 8.5 inches/min, an arc current of 135 A, a gas flow rate of 20 L/min and an arc voltage of 29 V. Protection of the fusion zone from the formation of defects and oxide layers was provided by a 99.9 % pure argon shielding during the deposition process. An interlayer deposition temperature of approximately 200°C was ensured using a laser thermometer to measure the surface temperature of the previous deposited layer. The deposited wall along with its dimensions can be seen in Figure 3.1. After production of the thin-wall it was cut from the base plate and ground on both sides to achieve flat surfaces to prepare the metallography samples with the dimensions of 10 x 7 x 7mm^3. It is notable that 0.5 cm of both ends of the fabricated part were discarded due to the instability of the arc at the starting and finishing points.

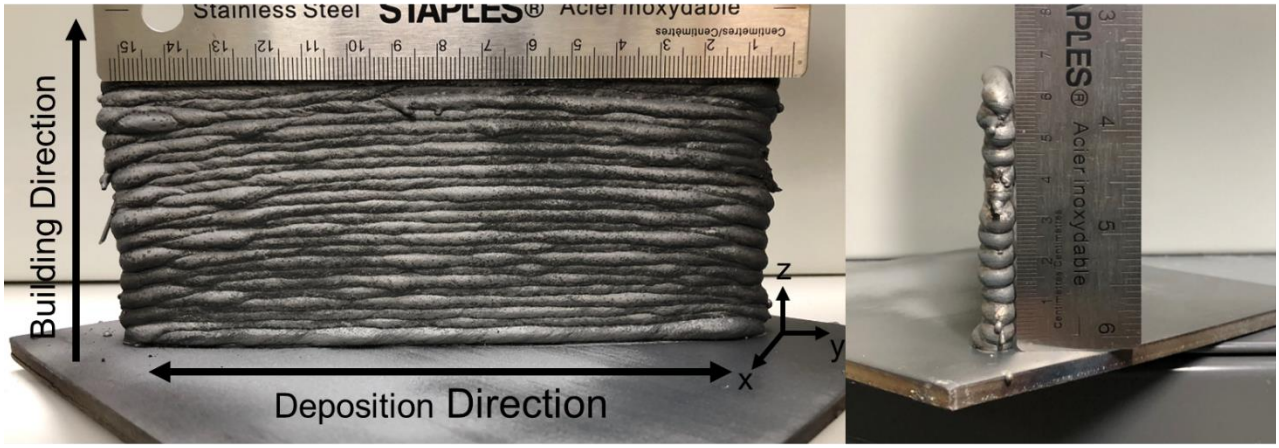

Figure 3.1. Depiction of the dimensions of the as-printed wall, showing building direction and deposition directions.

Table 3.1. Nominal chemical composition of the feedstock wire and the base metal (wt.%).

	C	Cr	Mn	Si	S	P	Ni	Mo	Sn	V	Cu	Al	Fe
Wire	0.3-0.4	12-14	0-1	0-1	0-0.03	0-0.04	0-0.5	0-0.5	0-0.05	-	0-0.5	0-0.5	Bal.
Base	0.15-0.46	12-14	0.4-1	0-1	0-0.03	0-0.04	-	0-0.1	-	0-0.3	-	-	Bal.

2.2. Microstructural characterizations

Metallographic specimens of the austenitized and tempered samples were all cut from the middle region of the deposited wall. The samples were mounted in an epoxy resin before grinding and polishing according to standard procedures for MSSs using a Tegramin-30 Struers auto-grinding and polishing machine. The polished samples were then etched for around 20 s in Vilella etchant containing 1 g picric acid, 5 ml hydrochloric acid, and 100 ml ethanol. The microstructural features of the samples were investigated using FEI MLA 650F scanning electron microscope (SEM) equipped with an energy dispersive X-ray spectroscope (EDX) to determine the chemical composition of the phases. Phase identification was carried out utilizing

X-ray diffraction (XRD) method performed by an Ultima-IV XRD machine. A scanning rate of 1 deg/min in a 2θ range of 20-100° was used with Cu-K_α radiation (λ=1.54Å). To further characterize the crystallographic orientation of the samples, electron backscatter diffraction (EBSD) techniques were used to produce accurate grain size distribution, low and high angle grain boundary maps, pole figures (PFs) and inverse pole figures (IPFs). The software Channel 5 of the HKL Inc. was employed to post-process the obtained raw data. It is notable that only data points with a confidence index higher than 0.01 were considered for the analysis in this study.

2.3. Electrochemical analysis

The corrosion behavior of as-printed, austenitized and quenched(A&Q) and austenitized and tempered (A&T) samples were investigated using potentiodynamic polarization (PD), and electrochemical impedance spectroscopy (EIS) after short and long time immersion was performed on the A&T samples. The tests were performed using a three-electrode cell setup with Ag/AgCl as the reference electrode, a graphite rod as the counter electrode and the MSS samples as the working electrode. For stabilization of the open circuit potential (OCP) the OCP was monitored for 1h before each test. All tests were performed with an IVIUM apparatus and software at room temperature in an aerated 3.5wt.% NaCl solution at room temperature and were performed at least three times on each sample to prove repeatability. The PD tests were performed using a scanning rate of 1 mV/s in the potential range of -0.2 V to 0.6 V versus the OCP and the samples were polarized cathodically to remove oxide layers already formed on the surface prior to the measuring of OCP. EIS tests at immersion times of 1h, 3 days, and 5 days were performed to investigate the behavior of the passive film after short and long immersion times. SEM images of samples following PD tests were taken to identify corrosion mechanisms in the microstructure.

2.4. Post-fabrication heat treatment

To determine the optimal austenitizing temperature for corrosion studies, three different temperatures, including 950°C (A950), 1050°C (A1050) and 1150°C (A1150), were selected based on the 13Cr pseudo-binary phase diagram [12], both inside and outside the single-phase austenite region. All samples were austenitized for 30 minutes before air quenched to room temperature. Corrosion tests and microstructural analyses were performed on the different austenitized samples to identify the optimum austenitizing temperature which provides the best base for the subsequent tempering process. After the austenitizing step, the samples were tempered at 300°C (T300), 400°C (T400), 500°C (T500) and 600°C (T600) for 2 hours, and then air cooled to room temperature.

3. Results and discussion

3.1. Microstructural analysis

3.1.1. Austenitized samples

The SEM micrographs of the as-printed and the austenitized samples, including A950, A1050, and A1150 are shown in Figure 3.2. The microstructure of the as-printed sample (Figure 3.2a) consists of a relatively high fraction of residual delta ferrite embedded in a martensitic matrix in addition to an insignificant amount of retained austenite. The high cooling rate associated with the nature of the WAAM process led to the formation of the martensitic matrix. Moreover, delta ferrite retained at room temperature as a result of the high cooling rate combined with a sufficient amount of ferrite stabilizing elements, such as chromium, which limited the transformation of delta ferrite to austenite during cooling process [12]. This delta ferrite phase is undesirable due to its higher chromium content compared with the matrix, causing chromium depleted regions and the promotion of carbide precipitates [115–117]. The stabilization of austenite phase can be attributed to the chemical composition of the alloy and also the implemented interpass temperature (200°C), which lies between martensite start and finish

temperatures (M_s = 212.2°C and M_f =12.2°C) of the alloy [83]. It is notable that the microstructure of the as-printed sample has been comprehensively characterized with more details in previous publications of the authors [70, 71]. Figure 3.2b-d depicts the SEM images of the microstructure of the austenitized samples including A950, A1050, and A1150, respectively. The images revealed a martensitic matrix similar to the as-printed sample for the three temperatures, while carbide precipitates were seen to have formed at 950°C and 1050°C only. These carbides were found to be removed in the case of austenitizing at 1150°C.

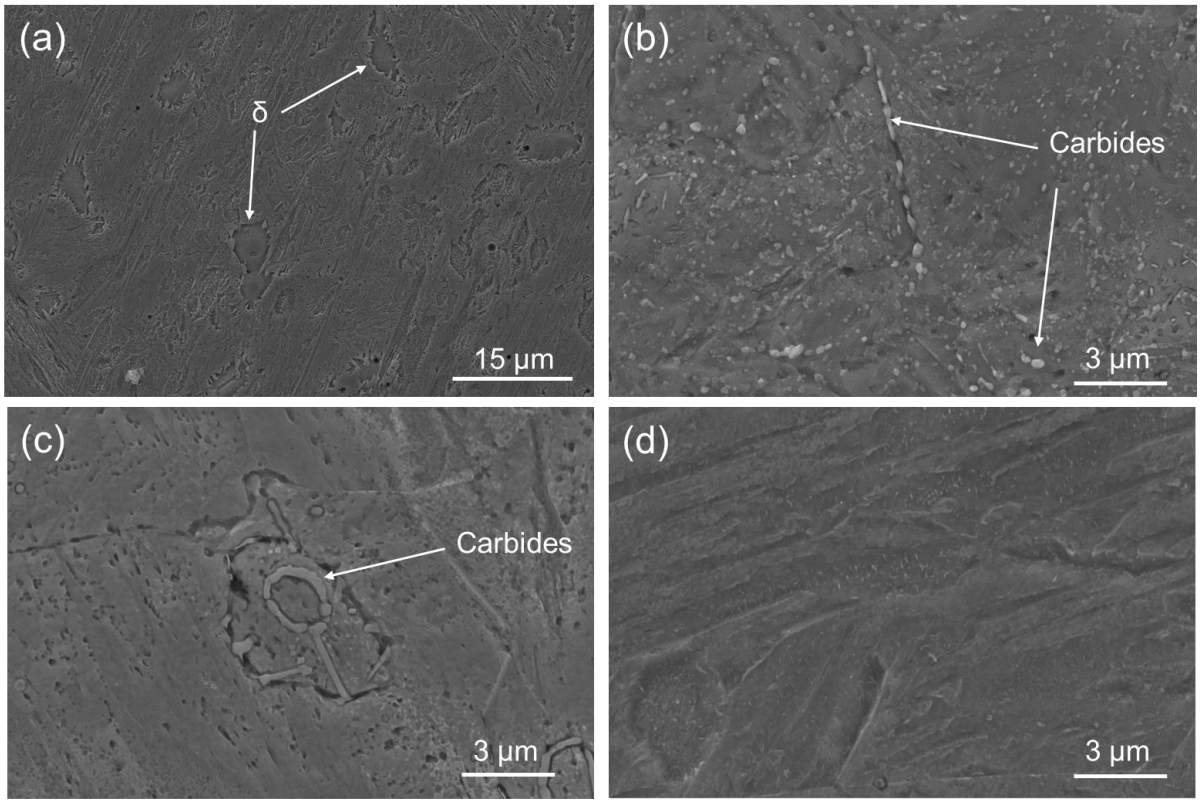

Figure 3.2. SEM images of a) as-printed sample and samples austenitized at b) 950°C, c) 1050°C and d) 1150°C.

EDX maps of chromium and iron along with SEM images of the as-printed and the austenitized and quenched samples are depicted in Figure 3.3. In the as-printed sample, the higher chromium content of the delta ferrite phases, and also lower concentration of iron, compared with the matrix can be seen in Figure 3.3a-c. Moreover, as shown in Figure 3.3d-f and Figure

3.3g-i for A950 and A1050 samples, the carbide precipitates form within residual delta ferrite phases, indicating that these austenitizing temperatures were not high enough to eliminate this phase. In contrast, the chromium and iron are evenly distributed for A1150, meaning that the delta ferrite is fully dissolved at this temperature (see Figure 3.3j-l).

Based on the microstructural observations, only one of the three austenitizing temperatures (1150°C) sufficiently re-transformed the delta ferrite to austenite during the heating cycle, which was then transformed to martensite upon cooling. Therefore, the austenitizing temperature of 1150°C was selected as the optimum heating cycle due to the complete removal of undesirable phases such as carbides and delta ferrites, in contrast to 950 and 1050°C which led to the formation of carbides within undissolved delta ferrite in the as-quenched condition.

It is important to note that carbide precipitates have been known to cause chromium-depleted zones in their nearby regions, thus increasing the susceptibility to sensitization phenomena and localized corrosion [118, 119]. Barlow *et al.* [42] also studied the influence of different austenitizing temperatures on the microstructural features conventionally fabricated AISI 420 alloy and reported that higher austenitizing temperatures were more efficient in complete removal of undesirable carbide particles during the austenitizing process. In another similar study by de Andrés *et al.* [120], the effect of austenitizing parameters, including heating temperature, heating rate, and cooling rate, on the dissolution of $M_{23}C_6$ carbides in the as-quenched of 0.45C–13Cr MSS had been investigated. They concluded that the peak austenitizing temperature required to obtain complete removal of the $M_{23}C_6$ carbides increases at higher heating rates, while austenitizing at 1060°C will guarantee total removal of carbides at any rate of heating. It is notable that optimum austenitizing temperature might vary based on the initial microstructure of the alloy. For example, the higher optimum austenitizing temperature identified in the current work (1150°C) can be attributed to the presence of residual delta ferrite in the as-printed microstructure which decelerate the austenitizing process.

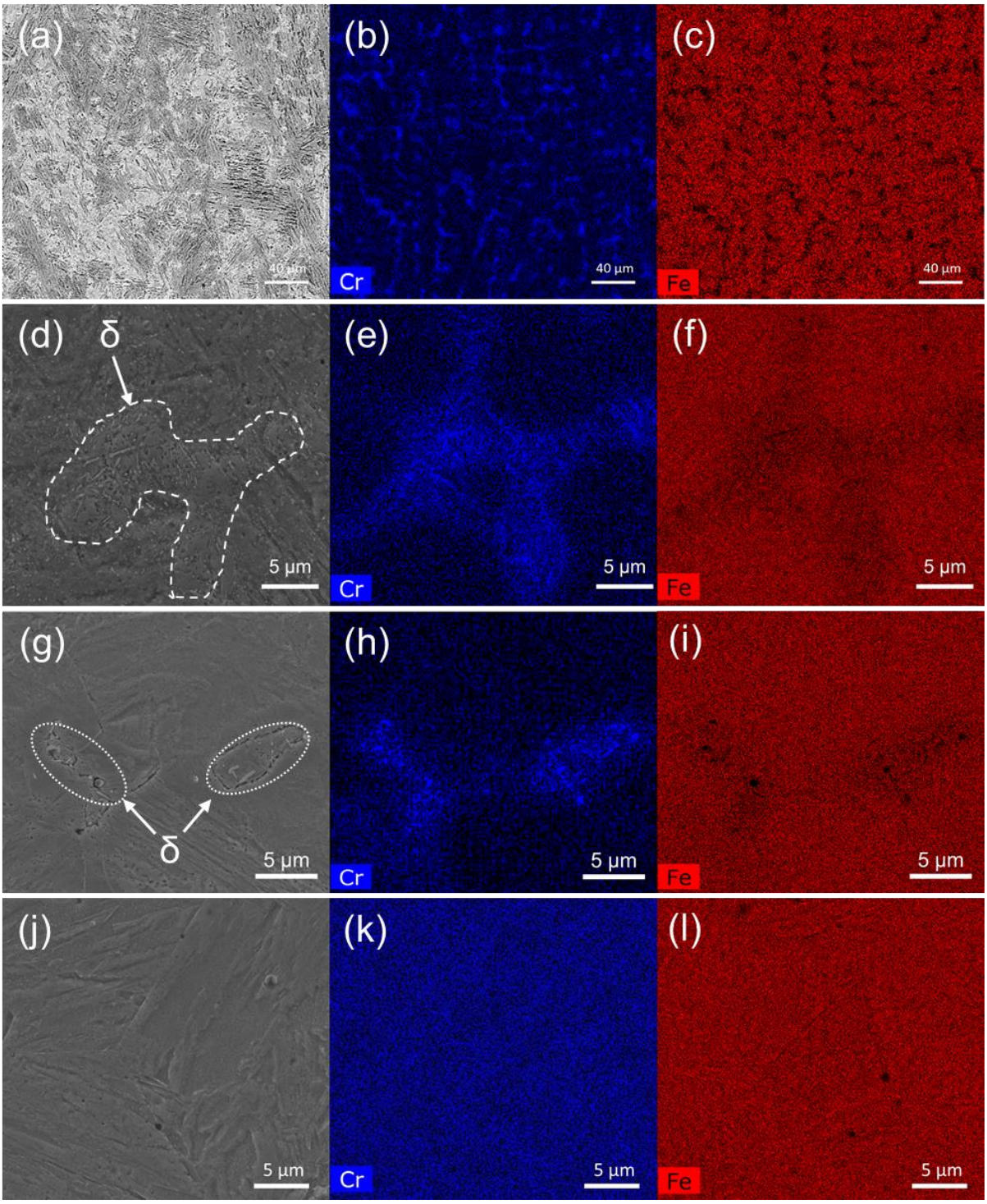

Figure 3.3. SEM images and EDX maps of Cr and Fe taken from (a-c) as-printed, (d-f) A950, (g-i) A1050 and (j-k) A1150 samples.

According to the above discussion, the present study will select A1150 samples with a fully martensitic microstructure (see Figure 3.2d) as the base case for the further tempering process

since the carbides potentially formed during tempering can be more easily distinguished from pre-existing carbides.

3.1.2. Tempered samples

Figure 3.4a-d depicts the microstructure of the WAAM 420 samples after austenitizing at 1150°C, air cooling to room temperature, and then tempering at 300°C, 400°C, 500°C and 600°C followed by air cooling. A comparison between the microstructure of the austenitized sample (A1150 seen in Figure 3.2d) and the tempered samples (T300, T400, T500, and T600 seen in Figure 3.4a-d), clearly reveals the formation of carbide precipitates as a result of the tempering process. As tempering temperature increases, the morphology of the carbides changes, where a transition from needle-shaped carbides for T300 and T400 to coarser and more spherical carbides for T500 to T600 was observed. T300 and T400 produced similar results, where a high concentration of intragranular needle-shaped carbides randomly distributed among the martensitic laths as shown in Figure 3.4a and b. In addition to these intragranular carbides, a continuous network of intergranular carbides along the primary austenite grain boundaries was also observed.

Previous studies [48, 51] on the heat treatment of 13 wt. % Cr MSSs have reported that the carbides formed at lower tempering temperatures were identified as Fe-rich M_3C with similar Cr-concentration to the matrix. As shown in Figure 3.4c, the carbides formed in the T500 sample were significantly smaller in size as compared to the other tempering conditions, while tempering at 600°C led to the coarsening of carbide particles (see Figure 3.4d). The smaller carbides found in T500 as well as the coarser carbides formed in T600 have been reported to be $M_{23}C_6$ with a significantly higher chromium concentration than the surrounding matrix, possibly leading to chromium depletion in the adjacent regions [51].

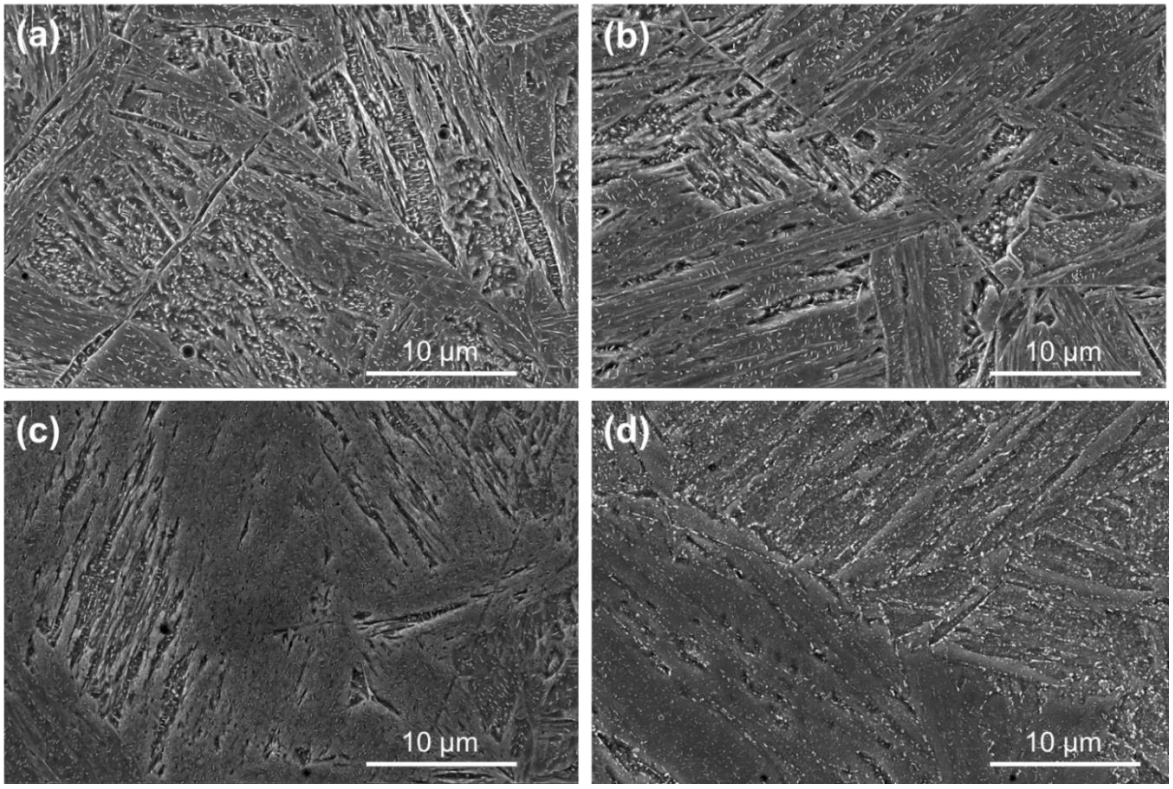

Figure 3.4. SEM micrographs of the WAAM samples after austenitizing at 1150°C and subsequent tempering at a) 300°C, b) 400°C, c) 500°C and d) 600°C.

The XRD patterns of the as-printed, austenitized (A1150), and tempered (T300, T400, T500, and T600) samples are shown in Figure 3.5. The obtained results confirm that the retained austenite phases formed in the as-printed condition, annotated by γ, was eliminated as a result of post-fabrication heat treatment cycles. Therefore the heat-treated samples only contain the BCC peaks, annotated by α', while the absence of the carbide phases peaks can be attributed to their significantly lower volume fraction compared to the martensitic matrix [77]. Although the diffraction peaks of alpha ferrite, delta ferrite and martensite are very similar in axis ratio, the BCC peaks detected in both austenitized and the tempered samples were determined to be martensite based on the microstructural observations in SEM micrographs. It is notable that tempering of other MSSs with similar chemical composition to the 420 alloy has been shown

to produce reversed austenite [86], however no austenite phase was observed for any of the tempered samples in the current study.

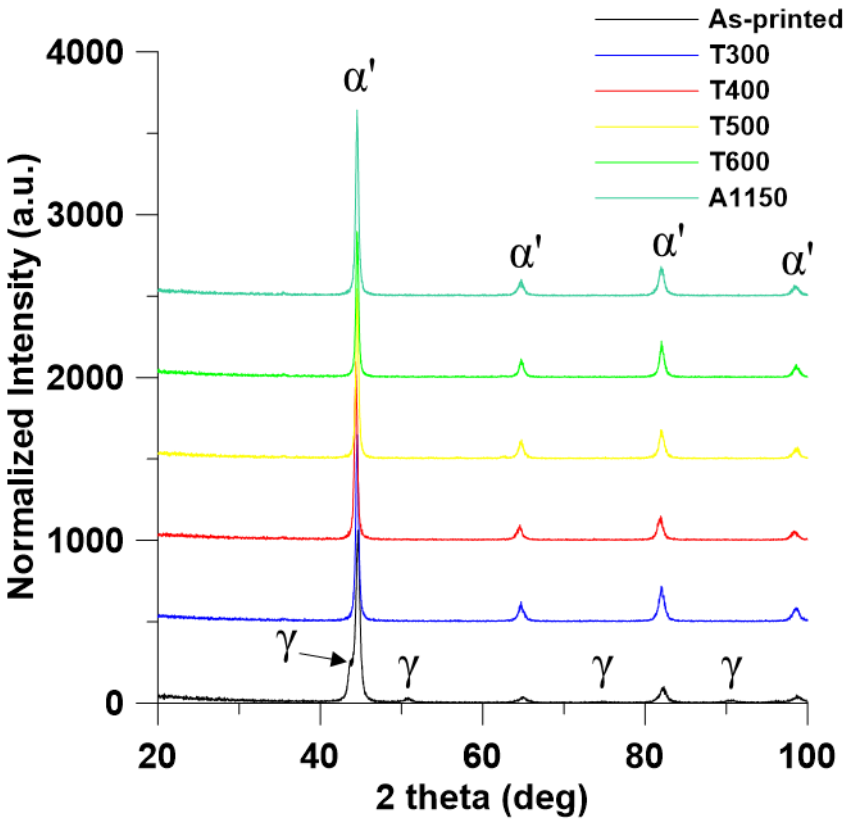

Figure 3.5. XRD patterns of the as-printed, austenitized (A1150), and tempered (T300, T400, T500 and T600) samples

3.1.3. EBSD analysis

Figure 3.6 shows the inverse pole figures (IPF) and image quality (IQ) maps of as-printed and T400. IPF maps superimposed with grain boundaries (Figure 3.6a and c), which are used to distinguish the lath martensite by projecting the crystallographic orientations normal to the observed plane, are represented with a stereographic triangle superimposed in the figures. As shown in Figure 3.6a and c, microstructure of both the as-printed sample and T400 reveal tempered martensite structure with a three-level hierarchy within their morphology: martensite lath, block, and packet, while the hierarchical nature of laths martensitic structure is confined

through the prior-austenitic grain boundary (PAGB) [121]. Moreover, the highlighted portion of IPF maps shown in the inset of the respective figure (in Figure 3.6) can specify the crystallographic orientation of laths with a combination of mixed orientations normal to {001}, {101}, and {111} planes. The IQ maps of the samples (Figure 3.6b and d) project the quality of the Kikuchi line for each captured EBSD map. Since it is difficult to obtain a clear Kikuchi-line diffraction at the grain boundaries, the IQ map quality is low and the gray scale level turns into dark at these boundaries, leading to a captured map similar to a conventional SEM image. The obtained IQ maps for samples tempered at 400°C can clearly distinguish the lath martensitic structure and PAGBs. On the other hand, the extreme dark regions of IQ map for the as-printed sample are representing the formation of retained austenite phase (face centered cubic structure) and are superimposed with the marked blue regions as shown in Figure 3.6b.

It should be noted that high volume fraction of retained austenite (~10%) phase is observed at the as printed samples, while the formed retained austenite phase disappears after the austenitizing, quenching and subsequent tempering process at 400°C. The PAGBs at the as-printed samples can be distinguished with orientation of the face centered cubic (FCC) structure as well, where the austenite regions with same orientation (Figure 3.6b) belong to the same PAGBs. The average lath size distribution for the as-printed sample and T400, Figure 3.7a and b respectively, reveals that the average lath size of the as-printed sample increases from 1.08 µm to 1.98µm after subsequent quenching and tempering process, an indication of lath coarsening after heat treatment which is visible at lath structure of the IPF maps in Figures 3.6a and c, as well. While the relative frequency of the low angle grain boundaries (LAGBs) at as printed sample is ~56%, this fraction decreases to ~52% for the sample tempered at 400°C, as seen in Figure 3.7c. It is well established that the LAGBs can hinder the fast diffusion by enforcing the grain boundaries diffusivity being equal to the bulk diffusivity and can impact the corrosion performance [67].

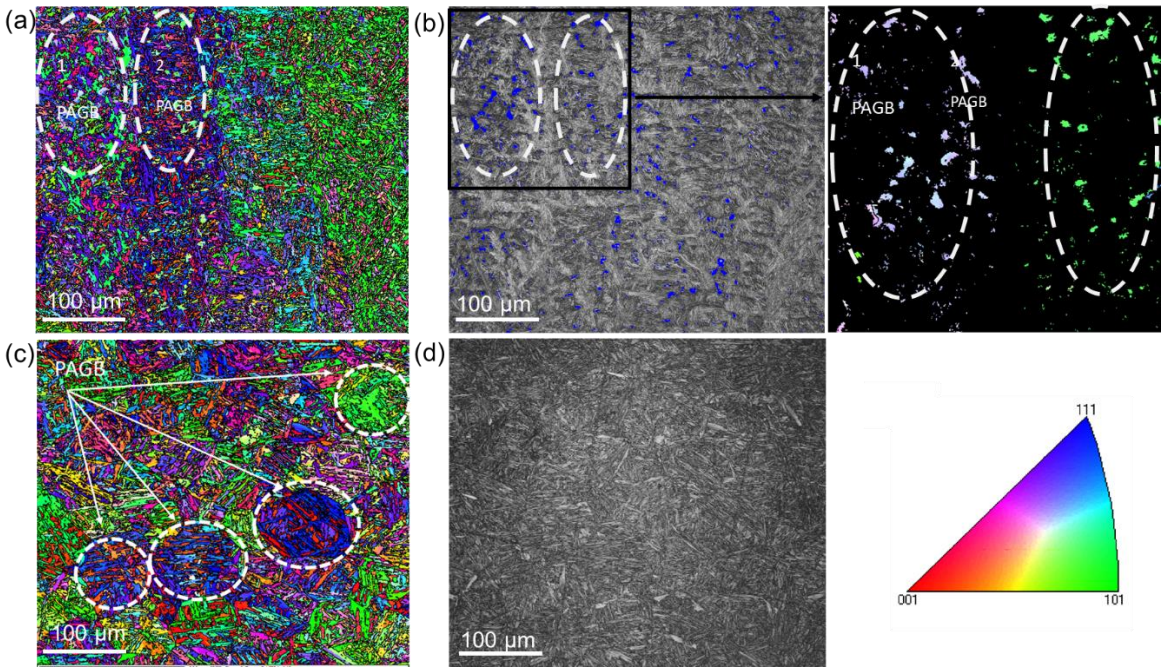

Figure 3.6. EBSD patterns of as-printed and T400 samples including IPFs for (a) as-printed and (c) T400 and IQs for (b) as-printed and (d) T400.

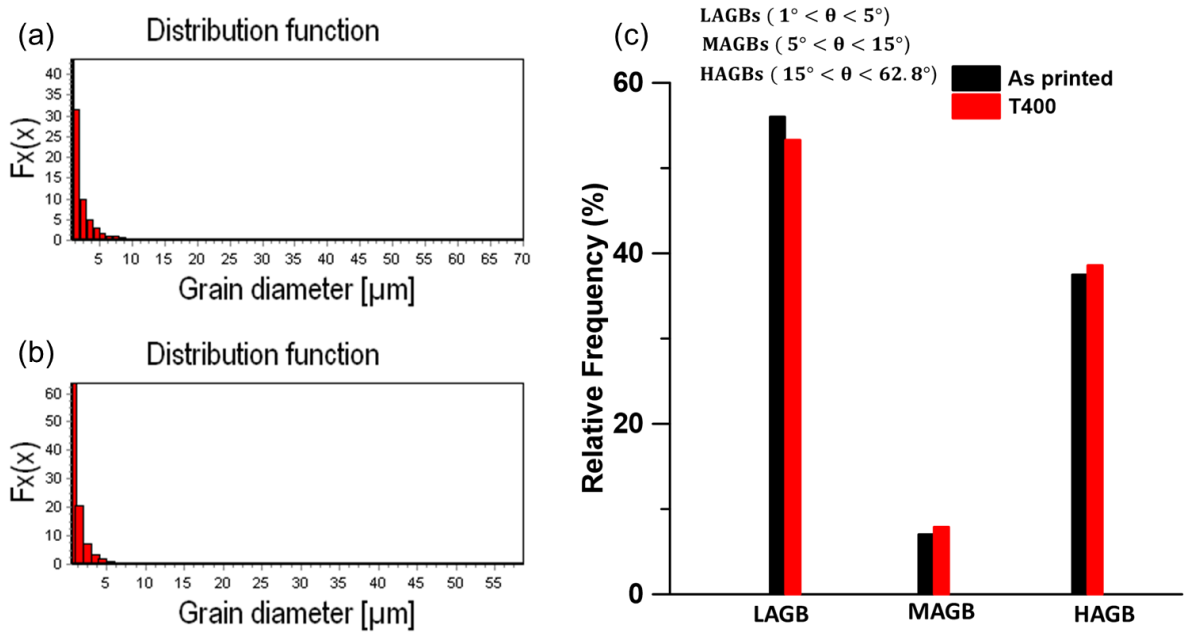

Figure 3.7. Grain size distribution for (a) as-printed and (b) T400 along with the misorientation angle distributions for the same samples.

The obtained pole figures of the body centered cubic (BCC) structure with the tempered martensite laths for the as-printed and T400 samples at the planes of {100}, {110}, and {111} are shown in Figure 3.8. As printed sample exhibits stronger cubic texture with high intensity components at the {100} and {110} planes (~4.91) aligned with the building direction compared to the tempered sample, where the intensity of pole components decreases to 2.16. The formation of strong texture in as printed sample at {100} plane is ascribed to the preferential growth (easier growth direction) aligned with <100> direction in cubic structures during solidification process [44, 122, 123]. During the austenitizing and quenching process, subsequent reheating and cooling of the as printed sample lead to transformation of retained austenite phase into the martensite and eliminates the preferential growth direction of primary grains, leading to lower texture intensity of the quenched and tempered sample at the {100} planes [87–89].

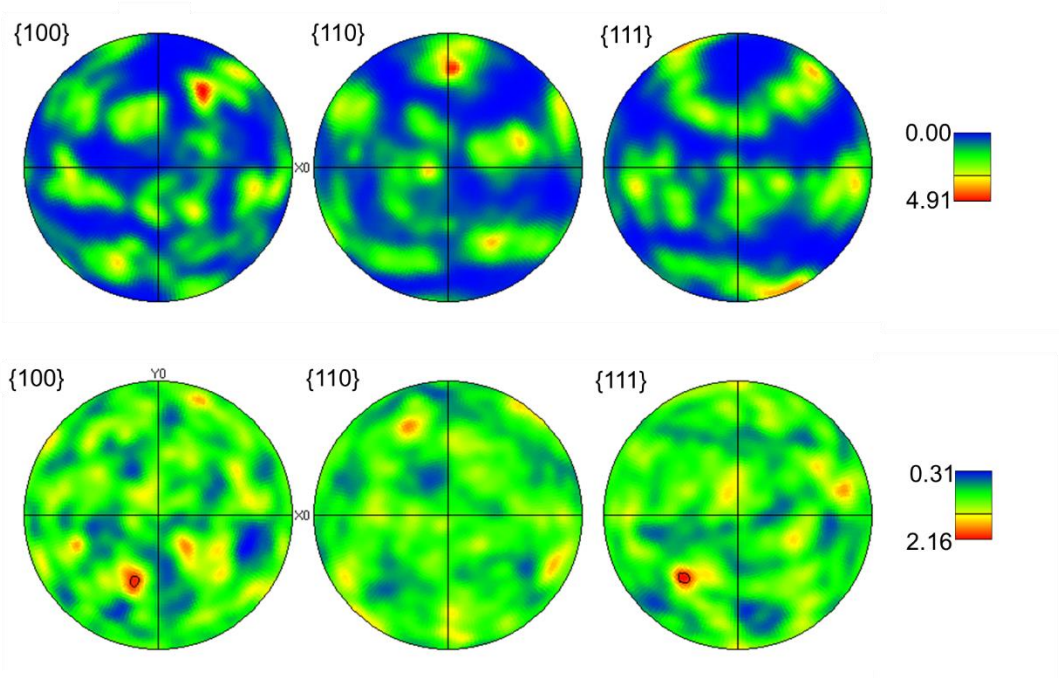

Figure 3.8. Pole figures of the martensite phases found in (a) as-printed and (b) T400.

3.2. Electrochemical analysis

Open circuit potential (OCP) variations over 1 h of immersion time in aerated 3.5 wt.% NaCl solution for all studied samples are illustrated in Figure 3.9. The OCP observed for T300, T400 and T600 stabilized after 1h, however fluctuations were observed for the as-printed and T500 samples, possibly an indication of active-like behaviour of passive film. The lower OCP values at the end of the 1h hour measurement indicates more deterioration of the passive layer, indicating a more resistant passive layer in T300 and T600. Samples showing higher OCP values are expected to have higher resistance to corrosion, as it is well stated that the thickness, quality and integrity of the passive film is related to monitored OCP values [50, 124].

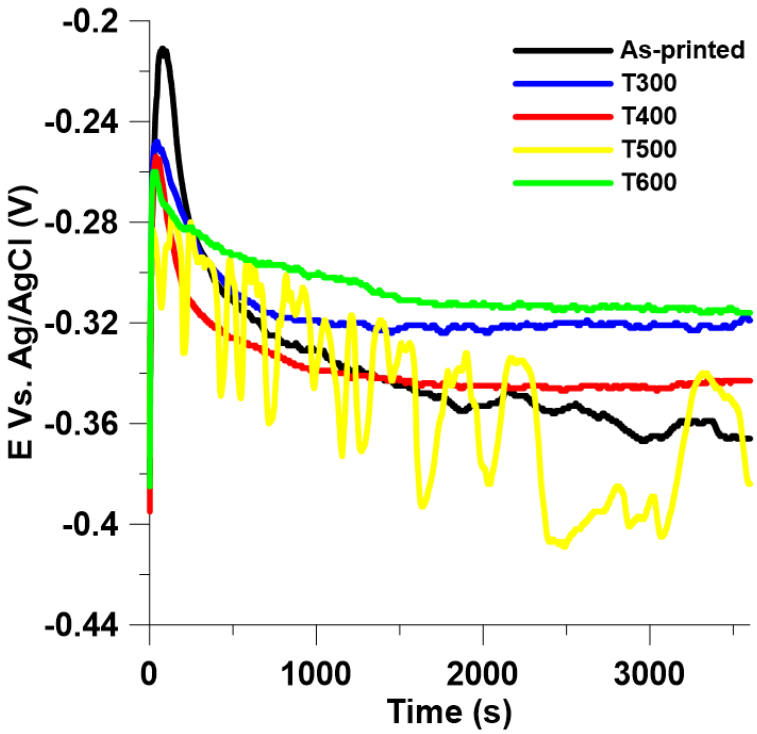

Figure 3.9. The open circuit potential of the as-printed and all tempered samples prior to potentiodynamic polarization.

3.2.1. Potentiodynamic polarization

The potentiodynamic polarization curves for T300, T400, T500, T600 and the as-printed sample are shown in Figure 3.10. All the parameters obtained from the potentiodynamic tests,

including pitting potential (E_{pit}), corrosion potential (E_{corr}), pitting current density (i_{pit}) and corrosion current density (i_{corr}) are summarized in Table 3.2. A distinct passive region and clear pitting potential can be observed for the T300, T400 and T600 samples, whereas T500 and the as-printed sample exhibit active surfaces. The highest pitting potential, indicating the highest resistance to pitting corrosion, can be seen for T400, followed by T300 and T600, respectively. While the T600 sample is showing highest corrosion potential (-0.316 ± 0.030 V), the as printed samples exhibit lowest corrosion potential, ascribed to sensitized regions formed near the delta ferrite phases. The highest corrosion potential observed was for T600, with the lowest being for the as-printed condition. Similar corrosion current density values can be seen for the samples not showing passivation, which are both higher than the corrosion current density for the samples showing passivation. The lower the corrosion current density and the greater the difference between corrosion and pitting potential is an indication of lower rate of corrosion [71]. The values for $E_{pit-corr}$ can be seen in Table 3.2 and shows that T400 has the largest difference between E_{pit} and E_{corr}, indicating that T400 sample shows the best corrosion performance.

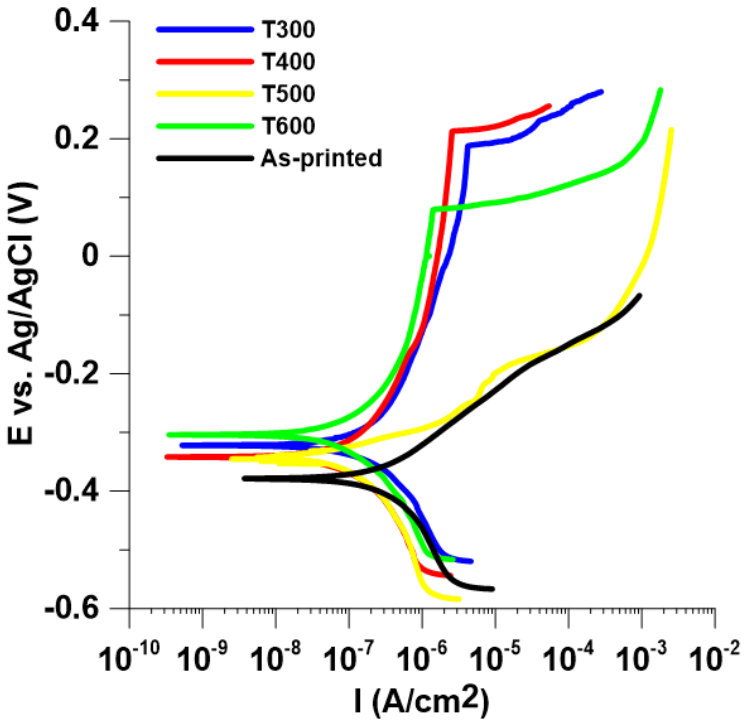

Figure 3.10. The potentiodynamic polarization graphs of the as-printed sample and all tempered samples after 1h OCP measurement.

Table 3.2. The parameters obtained from the potentiodynamic tests performed in an aerated 3.5 wt.% NaCl solution at room temperature.

Sample	**E_{pit} ($V_{Ag/AgCl}$)**	**E_{corr} ($V_{Ag/AgCl}$)**	**I_{pit} ($\mu A\ cm^{-2}$)**	**I_{corr} ($nA\ cm^{-2}$)**	**$E_{pit-corr}$ ($V_{Ag/AgCl}$)**
As-printed	N/A	-0.360 ±0.025	N/A	2.65 ± 0.194	N/A
T300	0.189 ± 0.015	-0.319 ± 0.022	4.25 ± 0.076	0.524 ± 0.11	0.508± 0.027
T400	0.214 ± 0.0030	-0.342 ± 0.010	2.67 ± 0.036	0.327 ± 0.045	0.556 ± 0.010
T500	-0.155 ± 0.0066	-0.328 ± 0.024	12.0 ± 0.18	5.33 ± 0.39	N/A
T600	0.077 ± 0.0086	-0.316 ± 0.030	1.40 ± 0.035	0.349 ± 0.074	0.393 ± 0.031

The relatively poor corrosion resistance observed for the sample in as-printed condition was the result of micro-galvanic coupling between the delta ferrite phases and the martensitic matrix. The delta ferrite contained a higher concentration of chromium compared with the matrix (Figure 3.3), leading to chromium depleted zones in the martensite-delta ferrite interfaces. The chromium content in these nearby regions was reduced sufficiently so that a passive oxide film could not form, leaving the anodic matrix exposed and highly susceptible to corrosive attacks when coupled with the cathodic delta ferrite [71]. As shown in Figure 3.3, austenitizing at 1150°C eliminated the delta ferrite, thereby healing the sensitized regions. Further tempering at any of the selected temperatures did not affect the distribution of chromium in the microstructure, as is shown by the EDX maps in Figure 3.11. This confirms that the diffraction peaks from XRD belong solely to martensite for the A1150 and tempered

samples as well as implies that the reason for the active surface in T500 is not caused by any residual delta ferrite.

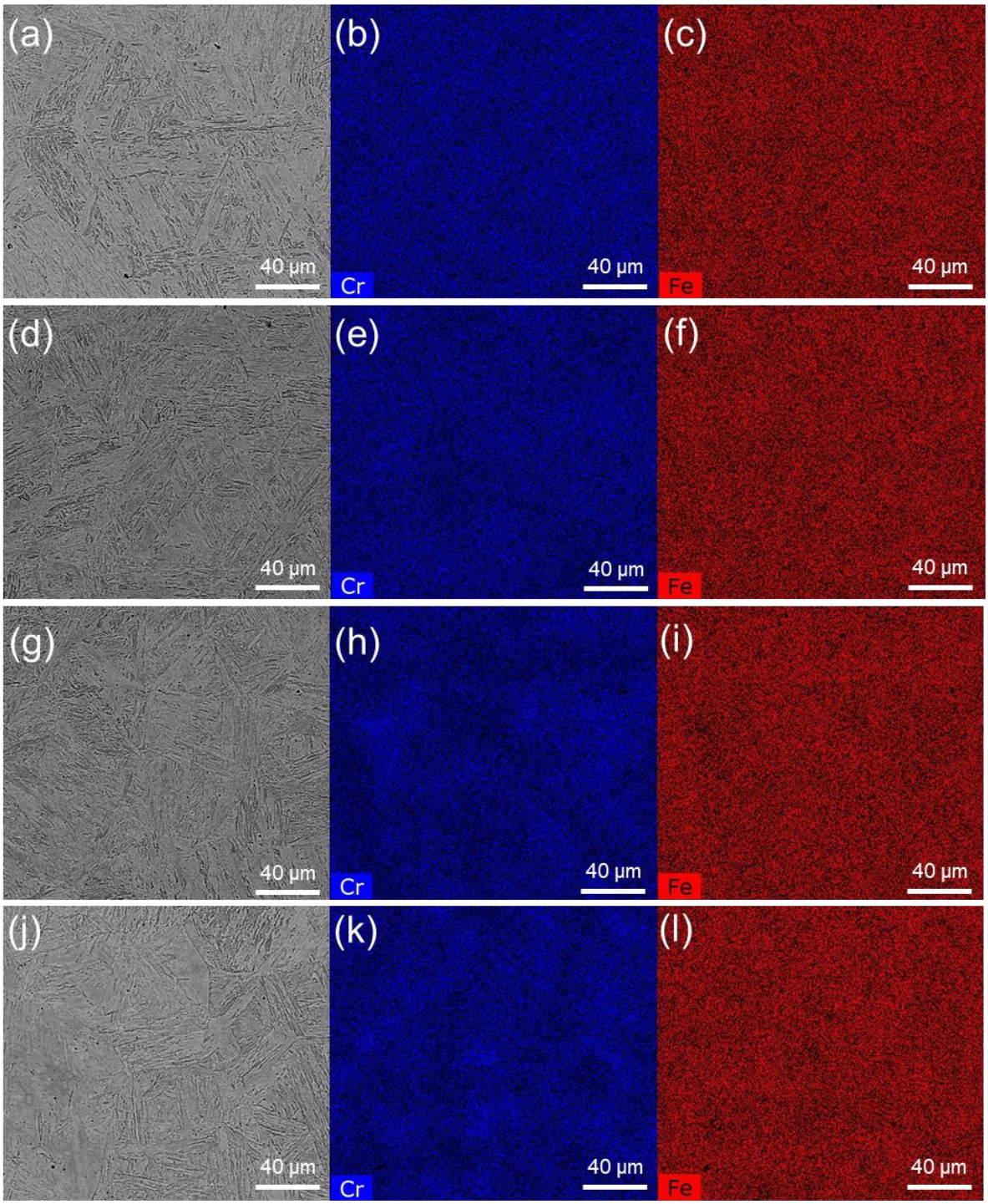

Figure 3.11. EDX maps showing the distribution of chromium and iron in (a-c) T300, (d-f) T400, (g-i)) T500 and (j-l) T600 samples.

The current densities in the passive region are significantly higher for T500, which indicates that the passive oxide layer of this sample has a higher dissolution rate [125]. The lower pitting potential of the T600 sample comes from the chromium content of the $M_{23}C_6$ carbide precipitate formed at higher tempering temperatures being larger than for the matrix [51]. Figure 3.12a-d and e-h show the EDX results of a higher magnification image of the carbide precipitates found in the T300 and T600 samples, respectively. The carbides found in T300 (Figure 3.12a-d) can be seen to have similar distribution of elements as the matrix, which supports the assumption that the carbides found in lower temperature samples are Fe_3C [48]. In contrast, the precipitates found in T600 (Figure 3.12e-h) are shown to have a higher concentration of both chromium and carbon, as well as a reduced iron content, indicating that these carbides are $M_{23}C_6$ [51]. The higher chromium content of these precipitates caused a chromium depletion in the nearby regions, weakening the passive oxide layer of the alloy.

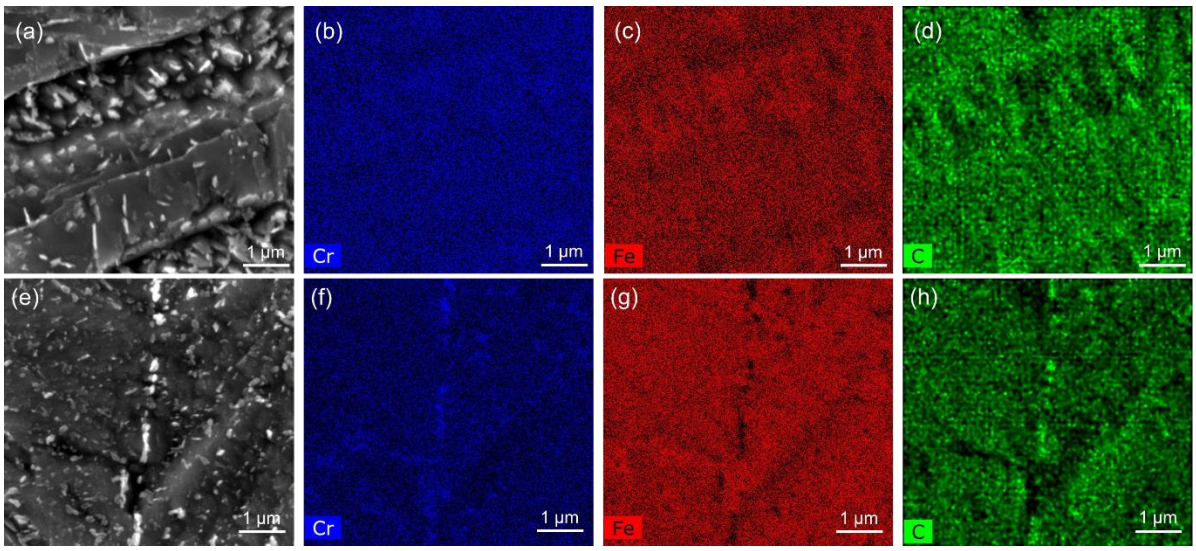

Figure 3.12. EDX maps of (a-d) T300 and (e-h) T600 samples showing a higher chromium concentration in the carbide precipitates found in T600 compared to the precipitates found in T300.

Although the active surfaces observed in the T500 sample and as-printed sample are similar, the driving force for the weak passive layer is different. The high chromium content of the large amount of nano-sized carbides formed in T500 led to chromium depletion in the interface region between the martensitic matrix and precipitates, causing a high number of sites for pits to form [48]. Compared with the other tempering temperatures, T500 produces smaller sized carbides with higher chromium content [48]. The high number of these smaller carbides caused the fluctuating OCP values seen in Figure 3.9. The small distance between the sensitized regions adjacent to the $M_{23}C_6$ carbides led to an active surface due to the coalescence of these regions, creating a continuous disruption of the passive layer [86]. When considering the galvanic series, carbides containing a higher amount of chromium are likely to be more noble compared to the surrounding matrix [126]. Larger differences in potential between carbides and matrix indicate that a lack of passivation can occur, which can be seen for T500 [127]. The better passivation behavior of T300 and T400 comes down to the chemical composition of the M_3C precipitates, as the similar chromium concentration to the matrix do not cause any sensitized regions [48, 51]. Tempering temperatures higher than 500°C led to desensitization of chromium to the matrix along with larger carbides, which resulted in fewer initiation sites for pits to occur, thus T600 showed improved corrosion resistance compared with T500 [48, 95].

3.2.2. Electrochemical impedance spectroscopy

The Bode and Nyquist plots generated from the electrochemical impedance spectroscopy (EIS) can be seen in Figure 3.13 and 3.14, respectively. All samples were measured with regards to OCP in an aerated NaCl solution of 3.5 wt.% and were exposed to the solution for immersion times of 1 hour, 3 days, and 5 days. This was done to characterize the evolution of the passive oxide layer of the samples when exposed to corrosive media. Depending on the immersion time

and tempering temperature either a single capacitive loop, representing the double and passive layer, or a double capacitive loop, resulting from a protective layer, can be seen [128]. The larger capacitive semicircle in the Nyquist plot, seen in Figure 3.14, often indicates higher corrosion resistance in the passive layer of a sample [129, 130]. After 1 hour of immersion, depicted in Figure 3.14a, the largest semicircle belongs to T400, followed subsequently by T300, T500 and lastly T600. A significant decrease in semicircle size can be observed for all samples after being immersed in the solution for 3 days, ascribed to the dissolution of the passive film into the electrolyte. Increasing the immersion time further does not seem to affect the size of the semicircle significantly, indicating that a passive film has stabilized.

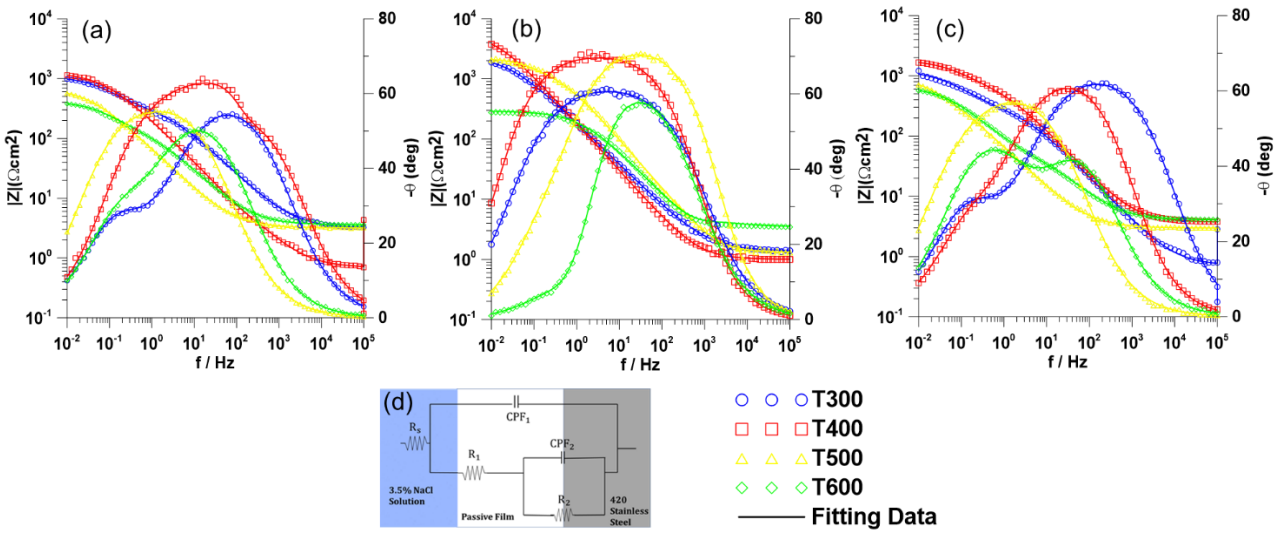

Figure 3.13. Bode plots of the tempered samples at immersion times of a) 1 hour, b) 3 days and c) 5 days, along with d) the equivalent circuit used to describe the EIS data over time.

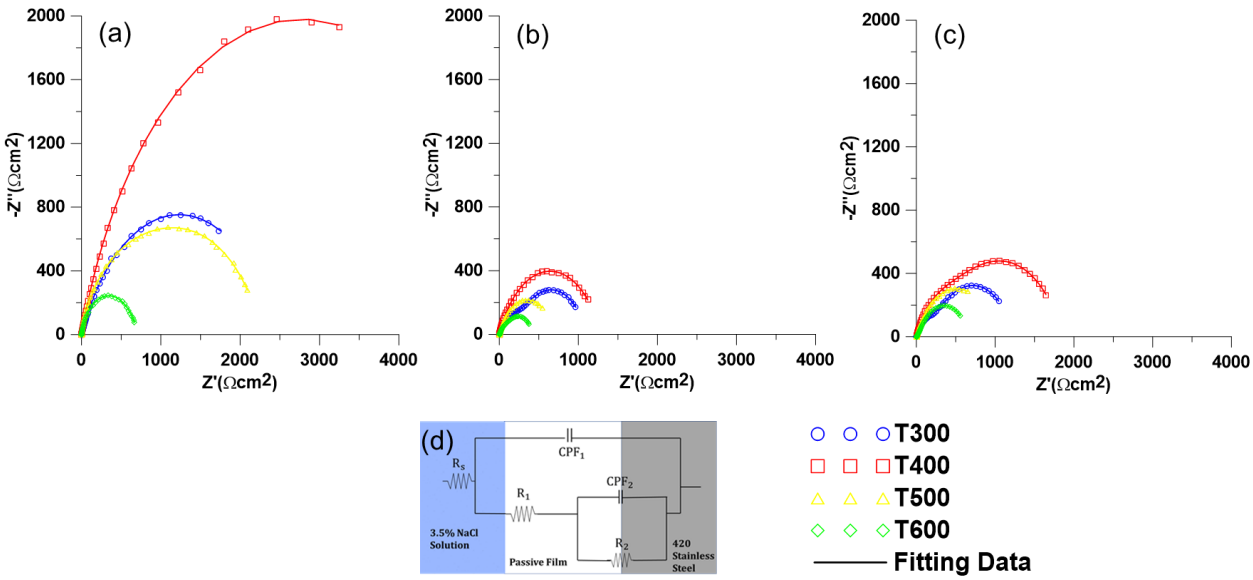

Figure 3.14. Nyquist plots of the tempered samples at immersion times of a) 1 hour, b) 3 days and c) 5 days, along with d) the equivalent circuit used to describe the EIS data over time.

Based on the semicircles of the samples in the Nyquist plot the T400 sample shows the highest corrosion resistance, which corresponds well with the observed PD results. However, the third largest semicircle belongs to T500, which does not directly agree with the results obtained in the potentiodynamic tests. In the potentiodynamic tests T500 clearly shows the lowest resistance to corrosion of the tempered samples due to its active surface. When looking into the EIS results further, namely the Bode plots and the fitting data seen in Table 3.3, the reason for T500's larger semicircle can be explained. For T300, T400 and T600 the value of the charge transfer resistance at the interface between the matrix and passive layer (R_{ct}) is larger than the value for the passive layer resistance (R_p) for all immersion times. When $R_{ct} > R_p$ the presence of a passive layer on the surface of the sample is confirmed, correlating well with the potentiodynamic results of these samples. For T500 however, it can be seen that $R_{ct} < R_p$ for all immersion times, indicating active behavior. The Bode plot after 3 days of immersion reveals that T500 shows the lowest impedance of the samples at higher frequencies, and that the impedance increases at lower frequencies. This can be interpreted to mean that T500 has

more resistance to general corrosion, but less resistance to pitting due to the type, concentration and size of carbides found at this tempering temperature. The potential difference between carbide and matrix for an MSS tempered at 500°C has been shown to be larger than for lower tempering temperatures, however exposure to a corrosive solution over time causes this potential difference to decrease [127]. This decrease in potential difference does not occur for lower tempering temperatures and is attributed to differences in how the passive oxide layers perform [127]. The change in potential during exposure to a corrosive solution can result from the deposition of corrosion products onto the surface, thereby covering up the heterogeneities in the microstructure of T500 [131]. The improved corrosion resistance results observed for T500 in the EIS compared with the PD are due to this.

Table 3.3. The fitting data values of the tempered samples after immersion times of 1h, 3d, 5d obtained from the EIS.

Sample	R_s (Ωcm^2)	R_p (Ωcm^2)	R_{ct} (Ωcm^2)	CPE_p ($\Omega^{-1}cm^2s^n$)	N_1	CPE_{ct} ($\Omega^{-1}cm^{-2}s^n$)	N_2
T300_1h	1.38	688	1772	2.75E-05	0.70	8.25E-06	0.70
T400_1h	1.00	1.22	5474	1.40E-05	0.79	1.55E-06	0.82
T500_1h	1.30	1342	922	7.09E-05	0.82	3.23E-04	0.70
T600_1h	0.61	1.64	712	1.64E-04	0.70	4.13E-05	1.03
T300_3d	3.09	258	904	5.50E-05	0.70	3.18E-05	0.70
T400_3d	1.08	3.00	1089	1.00E-05	0.75	1.53E-05	0.80
T500_3d	3.19	687	97.5	7.80E-05	0.70	9.75E-05	0.71
T600_3d	3.56	290	325	1.30E-04	0.70	1.52E-04	0.72
T300_5d	1.33	327	917	1.50E-05	0.74	6.40E-05	0.70
T400_5d	3.75	809	1036	1.22E-05	0.75	5.40E-05	0.70
T500_5d	2.98	748	257	3.92E-05	0.70	5.16E-05	0.72
T600_5d	4.06	294	609	8.55E-05	0.70	6.55E-05	0.70

Comparing the samples exhibiting passive behavior (T300, T400 and T600) it can be seen that after 1 hour of immersion the charge transfer resistance R_{ct} differ significantly. The values achieved by T400 are higher than for T300 and T600, indicating that the passive film in this sample is more protective than for the other samples [68]. This same pattern can be seen for longer immersion times, however with a smaller difference in values, ascribed to the deposition of corrosion products covering up inhomogeneities in the microstructure. A larger value for CPE_{ct} for a sample suggests that a more defective passive film has formed on the samples [68]. This corresponds well with the results observed in Table 3.3, where T400, T300 and T600 had the lowest, second lowest, and largest values, respectively.

The steady-state passive film thickness (L_{ss}) was calculated for all tempered samples after 1h, 3d and 5d immersion based on the measured EIS data and are presented in Table 3.4. The parallel plate expression was used [132, 133]:

$$L_{ss} = \frac{\varepsilon\varepsilon_0 A}{C_f} \tag{2.1}$$

where ε is the dielectric constant for the passive film (taken to be 15.6 for Cr_2O_3 [134]), ε_0 is the vacuum permittivity ($8.854 \times 10^{-14}\ Fcm^{-1}$), A is the area of the tested surface and C_f is the capacitance for the pure passive film which can be calculated by using:

$$C_f = \frac{(Y_0 R_{ct})^{\frac{1}{n}}}{R_{ct}} \tag{2.2}$$

Here, Y_0 is the constant for the CPE taken as CPE_p from Table 3.3, R_{ct} is the charge transfer resistance obtained from Table 3.3, and n is the passive film exponent taken as n_1 from Table 3.3 [135–137]. The obtained values for Lss suggest that the passive film of T400 has the largest thickness after 1h immersion, followed subsequently by T300, T500 and T600. The thickness is then reduced for all samples after 3d while maintaining the same order of most thick to least thick. After five days an increase in film thickness can be seen due to the deposition of corrosion product on the surface resulting from the long immersion time.

Table 3.4. The calculated values for the capacitance (C_f) and the thickness of the passive layer (L_{ss}) for all tempered samples.

Sample	C_f ($\Omega^{-1}cm^{-2}s^n$)	L_{ss} (nm)
T300_1h	7.53×10^{-6}	2.52×10^{-8}
T400_1h	6.99×10^{-6}	3.95×10^{-8}
T500_1h	3.90×10^{-5}	7.45×10^{-9}
T600_1h	6.53×10^{-5}	2.85×10^{-9}
T300_3d	1.52×10^{-5}	1.25×10^{-8}
T400_3d	1.41×10^{-5}	1.96×10^{-8}
T500_3d	1.30×10^{-5}	1.04×10^{-8}
T600_3d	3.35×10^{-5}	6.70×10^{-9}
T300_5d	3.33×10^{-6}	6.91×10^{-8}
T400_5d	2.84×10^{-6}	9.11×10^{-8}
T500_5d	5.47×10^{-6}	2.46×10^{-8}
T600_5d	2.41×10^{-5}	9.32×10^{-9}

3.2.3. Corroded surfaces

Figure 3.15 shows the corroded surfaces of the tempered samples after a 1h PD test in an aerated NaCl solution of 3.5 wt.%. For all samples, the initiation of corrosive attacks was observed in the interface between the martensitic matrix and sulfide inclusions with high S and Mn concentrations (see Figure 3.16). Sulfide inclusions in stainless steels (SS) can cause chromium depletion in the nearby surrounding regions, making it a preferential site for corrosion [138]. It has been suggested that this mechanism works similar to desensitization near chromium carbides in SSs, and it is generally agreed upon that sulfide formations can affect corrosion, however it is not fully understood [139]. Other initiation sites for corrosion in

the tempered samples are depicted in Figure 3.15e-h. For T300, T400 and T600 (Figure 3.15e, f and h respectively) the susceptibility to intergranular corrosion was apparent, attributed to the carbide precipitates which formed along the primary austenite grain boundaries. The corrosive damage observed on T400 was less severe than for T300 and T600 in both grain boundaries and near inclusions (Figure 3.15), indicating a higher resistance to corrosion. The corrosion mechanism observed for T500 differed from the rest of the tempered samples, as more general corrosion was observed with initiation sites located near the intragranular carbides. This fits well with the reported higher concentration of Cr in the intragranular carbides found in T500 [51]. Intergranular corrosion is a common occurrence in SSs, as a galvanic coupling between the cathodic chromium carbides and the anodic martensitic matrix can form [140].

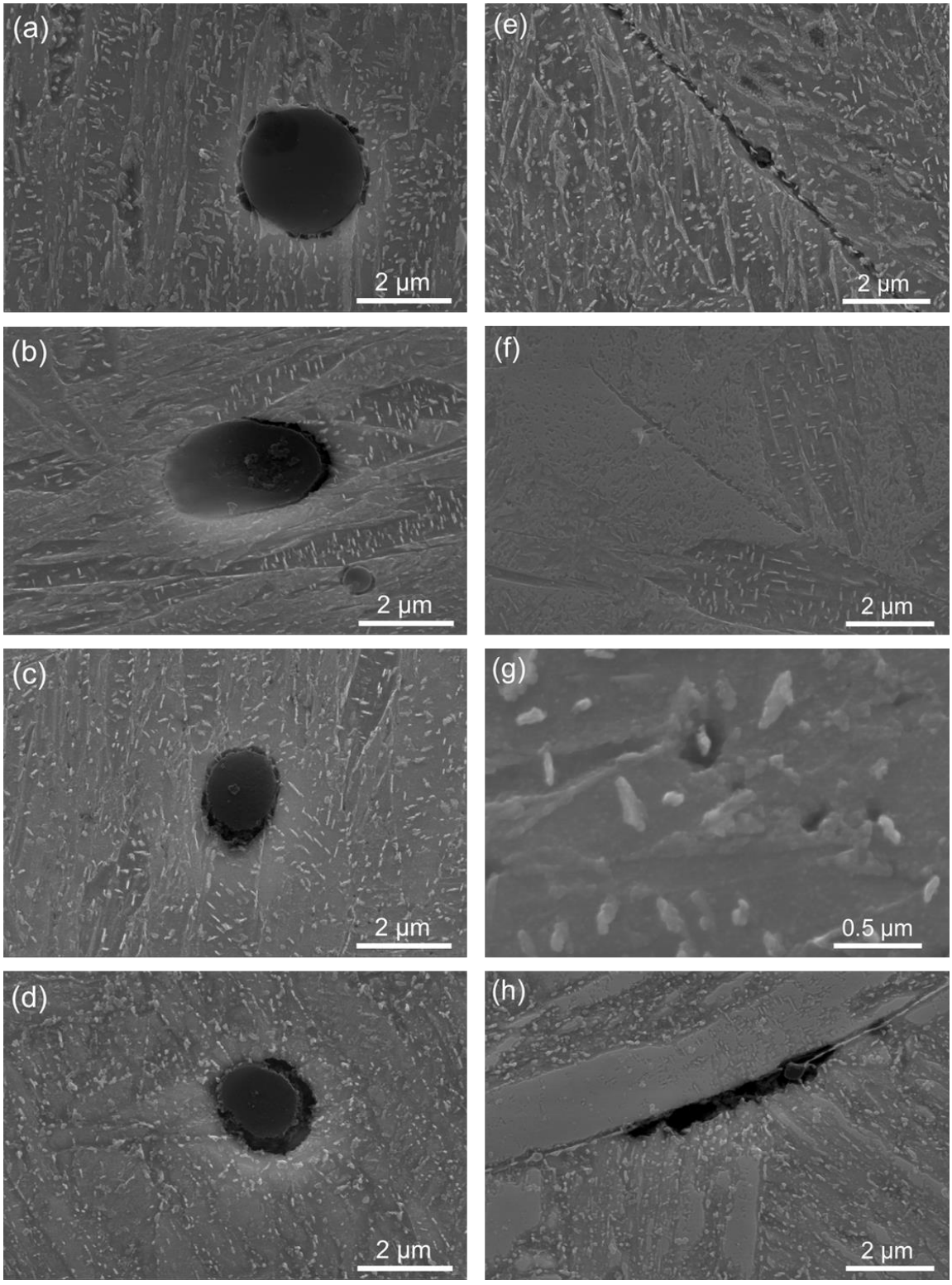

Figure 3.15. SEM images of the corroded surfaces of (a,e) T300, (b,f) T400, (c,g) T500, and (d&h) T600.

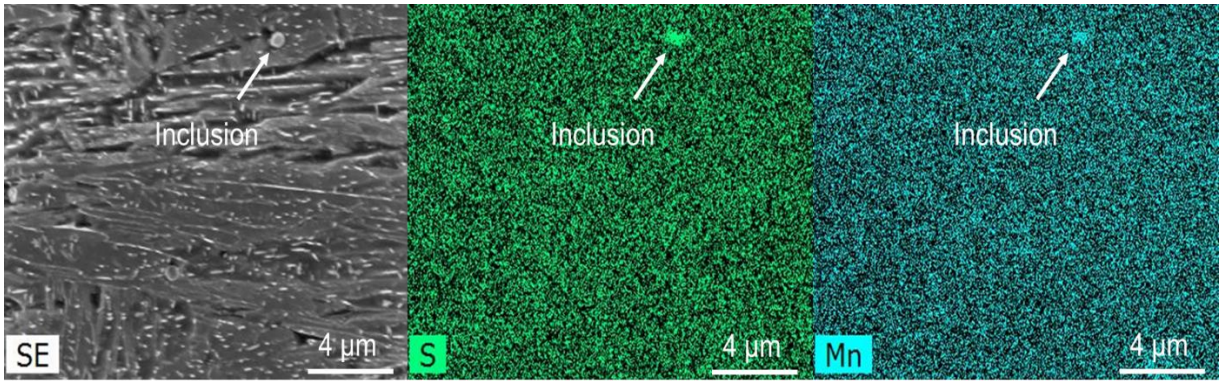

Figure 3.16. EDX maps showing the element concentration of the inclusions found in the tempered samples, example taken from T300.

4. Conclusions

Presented in this study was the improvement of corrosion performance of an AISI 420 MSS produced by WAAM through heat treatment. The following conclusions can be made:

- Austenitizing of as-printed samples at 1150°C and air-cooling to room temperature eliminated all pre-existing microstructural secondary phases. 1150°C was high enough to reach the single phase austenite region, the austenite was then able to fully transform into martensite upon cooling to room temperature. This part of the heat treatment removed the detrimental chromium-rich delta ferrite phase.
- Tempering at temperatures of 300°C, 400°C, 500°C and 600°C for 2 h led to the formation of carbide precipitates within the martensitic matrix. The chemical composition of these carbide precipitates changed with temperature, where a higher tempering temperature caused a higher chromium content in the precipitates. Needle-shaped, Fe-rich M_3C was observed for T300 and T400, while smaller $M_{23}C_6$ formed in T500. Coarser and more spherical shaped carbides could be seen in the grain boundaries for T600.
- PD tests revealed that the highest corrosion resistance was exhibited by T400, where a clear passive region ascribed to the formation of a strong and uniform oxide layer was

formed. Similar oxide layers were formed for T300 and T600, however not as strong as for T400. T500 exhibited the weakest corrosion resistance due to its active behavior, determined by unstable OCP measurements and lack of a passive region in the PD tests. The high chromium content of the carbide precipitates combined with the precipitates' close proximity to each other caused chromium depleted regions, ultimately disrupting the formation of a passive layer for this sample.

- Compared with the PD tests, the results obtained from EIS suggested a higher corrosion resistance for T500. However, this was due to the deposition of corrosion products on the surface of the sample, acting as a protective layer. For T300, T400 and T600 the EIS results agreed with the PD results, confirming a higher corrosion resistance for T400.
- The initiation of corrosive attacks was seen to occur near inclusions with high Mn and S concentrations for all samples. Intergranular corrosion was observed for all of T300, T400, and T600, whereas T500 exhibited more general corrosion which initiated near intragranular carbide precipitates.

Chapter 4

The effects of tempering time on the microstructure and corrosion behavior of wire arc additively manufactured 420 martensitic stainless steel

Preface

I am the first and corresponding author of this paper. Along with the co-authors, Salar Salahi and Dr. Ali Nasiri, I investigate the effects of tempering time on the microstructure and corrosion behavior of a wire arc additively manufactured 13Cr (AISI 420) martensitic stainless steel part. I prepared methodology, performed experiments, analysed the data, and prepared the first draft of the manuscript, and given the co-authors' feedback I revised the paper. Salar Salahi contributed with experiments and data analysis, and Dr. Ali Nasiri contributed with conceptualization, design, project administration, and supervision, review and editing of the manuscript.

Abstract

In this study, the effects of tempering time on the microstructure and corrosion behavior of a 420 martensitic stainless steel (MSS) fabricated using wire arc additive manufacturing were investigated. The microstructure of the as-printed part consisted of retained austenite and detrimental delta ferrite embedded in a martensitic matrix. The undesirable delta ferrite phase was eliminated through austenitizing, followed by air-quenching of the as-printed samples, before tempering at 400°C. A wide range of tempering times from 1 h to 8 h were investigated. The tempered microstructure was found to contain a martensitic matrix along with both inter-

and intragranular nano-sized carbide precipitates, formed within and along primary austenite grains and their boundaries. An increase in the size of carbide precipitates was observed with increasing the tempering time from 1 h to 8 h. Electrochemical studies revealed a decrease in pitting potential and passive layer resistance of the fabricated alloy as tempering time increased, indicating the deterioration of corrosion resistance. The corrosion morphology assessment of the tempered samples revealed that primary austenite grain boundaries were the preferential sites for localized corrosion attacks in all samples, ascribed to the formation of intergranular chromium carbide precipitates, causing the alloy's susceptibility to intergranular corrosion. Larger sized carbides in samples tempered for longer times were proven to be detrimental to the corrosion performance.

1. Introduction

Metal additive manufacturing (AM) has provided a more viable way of fabricating intricate components at drastically lower fabrication time [45]. This fabrication method differs from conventional subtractive methods by depositing feedstock material in a layer-by-layer fashion until achieving a near-net-shaped component [59]. As a direct energy deposition process, in wire arc additive manufacturing (WAAM), a wire is used as the feedstock material and an electric arc or plasma as the heat source [141]. The high deposition rate associated with the WAAM process along with its low capital cost and material waste, make this AM method a suitable option for fabrication of large-scale components [18].

Martensitic stainless steel (MSS) is a relatively new material used as feedstock wire for WAAM. It is considered as a general-purpose material due to its moderate resistance to corrosion and excellent mechanical properties [65]. AISI 420 is a MSS alloy containing approximately 13 wt.% Cr [69]. As a result of its ability to achieve a range of different microstructural features after exposure to specific heat treatment cycles, AISI 420 MSS is commonly used for a wide range of applications [108]. However, when used as feedstock material for WAAM, this ability can make it challenging to predict the final microstructure of the fabricated part due to the complex thermal history during deposition and subsequent cooling [70, 71]. The deposition of subsequent layers during WAAM causes the part to experience multiple heating and cooling cycles, leading to an inhomogeneous final microstructure containing multiple phases [59]. From the corrosion's perspective, a multiphase microstructure can be detrimental to the pitting and intergranular corrosion resistance in MSSs [109]. In previous works by the authors, it was determined that the complex thermal history led to the formation of delta ferrite in the as-printed microstructure of the WAAM-420 MSS part [70, 71]. The higher Cr concentration of the delta ferrite phase compared to the martensitic matrix

caused depletion of Cr in the nearby regions of the delta ferrite, ultimately causing local loss of passivation, which resulted in reduced corrosion resistance [71].

Heat treatment of MSSs can be a complicated procedure as the carbon content promotes the formation of various carbides depending on temperature, time, and chemical composition of the treated alloy [112]. The formed carbides in MSSs are an important factor in influencing the alloys' resistance to abrasion, wear, and corrosion [120]. Undesirable microstructural phases affecting corrosion resistance, such as delta ferrite and Cr-rich carbides, can be eliminated through austenitizing at sufficiently high temperatures before tempering [58]. Bonagani et al. (Bonagani et al., 2018) investigated how different tempering treatments can influence the microstructure and pitting corrosion of a 13Cr MSS and reported that different types of carbides form at different temperatures, Fe-rich M_3C at 300°C and Cr-rich $M_{23}C_6$ at 550°C and 700°C. Another study (Lu et al., 2015) similarly reported the formation of nano-sized M_3C, nano-sized $M_{23}C_6$, and micron-sized $M_{23}C_6$ after tempering at 300°C, 500°C, and 650°C, respectively. It was reported that tempering at higher temperatures led to sensitized regions by Cr-rich carbides, which caused a more electrochemically active microstructure (Anantha et al., 2017).

Although, the effects of tempering temperatures on the microstructure and corrosion properties of 13Cr MSS have been reported in the literature, little has been done to elucidate the impact of tempering time on corrosion performance of the alloy. Zhang et al., 2015 reported how holding time at 620°C affected the evolution of retained austenite in a 13Cr MSS containing 4% Ni and detected a parabolic trend with increasing time. During their investigation on how low-temperature plasma carburizing of AISI 420 MSS enhanced corrosion resistance of the alloy, Scheuer et al., 2019 found that the growth of detrimental Cr-rich carbides is promoted by longer treatment time. As a relatively new field of study, more work is needed to better understand the properties of WAAM fabricated MSSs, and in particular, the post printing of fabricated parts. Understanding the microstructural evolution during tempering of 420 MSS is

crucial to be able to assess the overall electrochemical properties and corrosion response of the alloy in service condition. Focusing on this gap, the purpose of the performed study was to investigate the effect of tempering time on the microstructure and corrosion behavior of 420 MSS.

2. Experimental methods

The tested material in this study was a 420 MSS fabricated using a robotic gas metal arc (GMA)-WAAM system. A thin-wall part was deposited layer-by-layer onto an AISI 420 substrate with an interlayer temperature of 200°C, which was ensured using a laser thermometer. The nominal chemical composition of both the feedstock wire and the base plate are given in Table 4.1. A six-axis robotic arm utilizing an all-y scanning strategy was employed for the fabrication of the part. A 99.9 % pure argon shielding gas provided protection of the fusion zone from oxidation and other contaminations during the deposition process. The process parameters used for deposition are listed in Table 4.2.

Table 4.1. Nominal chemical compositions of the used base metal and wire (wt.%)

Sample	Cr	C	Si	Mn	Ni	Mo	P	S	Cu	V	Fe
ER-420 Wire	12-14	0.3-0.4	0-1	0-1	0-0.5	0-0.5	0-0.04	0-0.03	0-0.5	-	Bal.
AISI-420 Base Plate	12-14	0.15-0.46	0-1	0.4-0.1	-	0-0.1	0-0.04	0-0.03	-	0.3	Bal.

Table 4.2. WAAM process parameters used for fabrication of the thin-wall part.

Wire Feed Speed	Travel Speed	Current	Gas Flow Rate	Arc Voltage	Wire Size
4.06 m/min	0.22 m/min	135 A	45 L/min	29 V	0.11 cm

Samples with dimensions of 10 × 7 × 7 mm^3 for metallographic examination and corrosion testing were extracted from the middle region of the fabricated thin-wall part. After

austenitizing and tempering, these samples were ground and polished following standard procedures for preparation of MSS and subsequently etched using Vilella's etchant. To investigate the microstructural features an FEI MLA 650F scanning electron microscope (SEM) equipped with a Bruker energy dispersive X-ray was used. X-ray diffraction (XRD) was performed using an Ultima-IV XRD machine to identify the phases present in the microstructure of the austenitized and tempered samples. The XRD machine used Cu-K_α radiation (λ=1.54Å) with a scanning rate of 1°/min in a 2θ-range of 20-100°. Further characterization of the crystallographic orientation of the samples was performed using electron backscatter diffraction (EBSD) analysis. This analysis produced inverse pole figures (IPFs), pole figures (PFs), grain boundary maps, and phase maps. To be considered valid for the study herein, the obtained data points needed a confidence index higher than 0.01.

The applied post-fabrication heat treatment included an austenitizing cycle for 30 min at 1150°C, air-cooling to room temperature, and then tempering at 400°C for various times. The austenitizing temperature was selected based on the 13Cr pseudo-binary phase diagram, where the high temperature of 1150°C was in the single-phase austenite region [12]. The investigated tempering times included 1 h, 2 h, 4 h, and 8 h.

The corrosion behaviors of the tempered samples were characterized by performing electrochemical testing including potentiodynamic polarization (PD) and electrochemical impedance spectroscopy (EIS). A three-electrode cell setup where the MSS sample was the working electrode, Ag/AgCl was the reference electrode, and a graphite rod was the counter electrode was used for the testing. To ensure consistency during testing, all tests were performed at room temperature in an aerated 3.5 wt.% NaCl solution using an IVIUM apparatus and were performed at least three times on each sample to prove repeatability. The open circuit potential (OCP) was monitored for 1 h before each test for stabilization purposes. The PD tests were performed versus the OCP using a scanning rate of 1 mV/s within the

potential range of -0.2 V to 0.6 V versus OCP. The EIS tests were performed after immersion times of 1 h, 24 h and 72 h in 3.5 wt.% NaCl solution. EIS testing was done to determine the evolution of the passive layer after different exposure times to the corrosive medium.

3. Results and discussion

3.1. Microstructure

The SEM images of the microstructure of the part in as-printed condition and after austenitizing at 1150°C and quenching is shown in Figure 4.1a and d, respectively. The as-printed microstructure consisted of a martensitic matrix along with secondary phases including retained austenite and delta ferrite [70, 71]. As can be seen in the EDX maps in Figure 4.1b and 32c, the delta ferrite phases contained a higher concentration of Cr compared with the matrix with detrimental effect to the corrosion performance of the part [71]. Figures 4.1e and f depict EDX concentration maps of the austenitized and quenched samples, where it is clear that the delta ferrite phase has been eliminated and a single-phase martensitic microstructure was achieved.

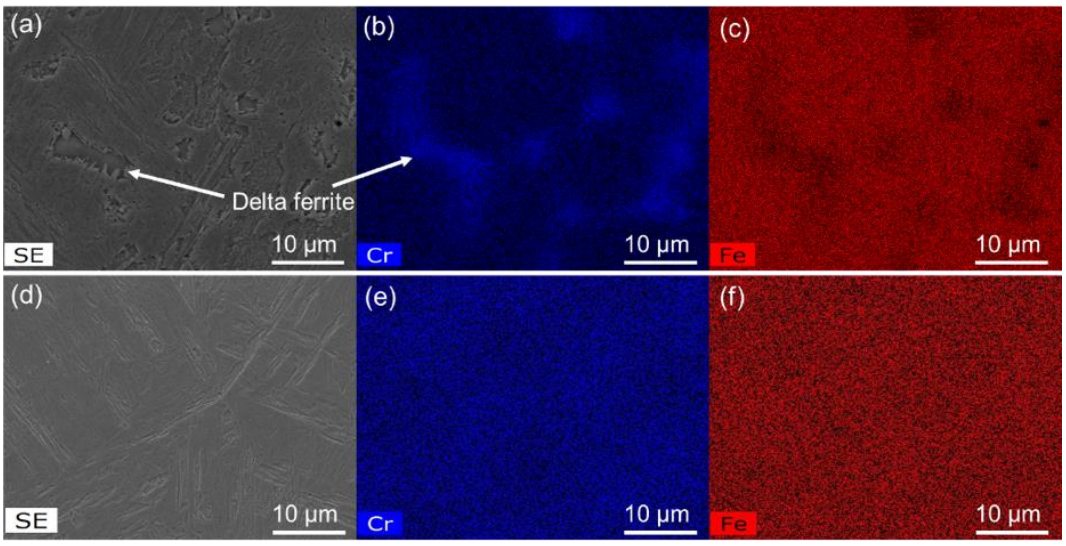

Figure 4.1. SEM images and EDX concentration maps of the fabricated thin-wall part in (a-c) as-printed and (d-f) austenitized and quenched condition.

The SEM micrographs of the samples after the austenitizing and tempering processes can be seen in Figure 4.2, where Figure 4.2a-d represent T400_1h, T400_2h, T400_4h, and T400_8h, respectively. For all tempered samples, a martensitic microstructure accompanied by both inter- and intragranular carbides were observed. The intragranular carbides observed for all tempering temperatures were needle-shaped precipitates distributed randomly among the martensitic laths and had similar concentrations of Cr to the matrix (Figure 4.2e-h). This is an indication that the observed carbides in the tempered samples are M_3C-carbides, which have been shown to form at lower tempering temperatures [48].

The intergranular carbides were distributed along the primary austenite grain boundaries (PAGB) where they formed a continuous network. No distinct difference could be observed in the intragranular carbides' shape or size as tempering time increased. However, the intergranular carbide network seems to be coarser in T400_8h sample than the other samples (Figure 4.3), indicating carbide precipitates' growth as tempering time increases. Precipitation and growth of carbides are diffusion-controlled, dictated by the tempering temperature and time [53]. Tempering of MSS at 400°C and 450°C for long times can cause precipitation of chromium carbides, such as Cr_7C_3 and $Cr_{23}C_6$ [144], which contain higher chromium concentration than the M_3C carbides. Consequently, the chromium carbides formed along the grain boundaries as a result of diffusion can create regions depleted of chromium at their periphery, which are susceptible to localized corrosion attacks [114].

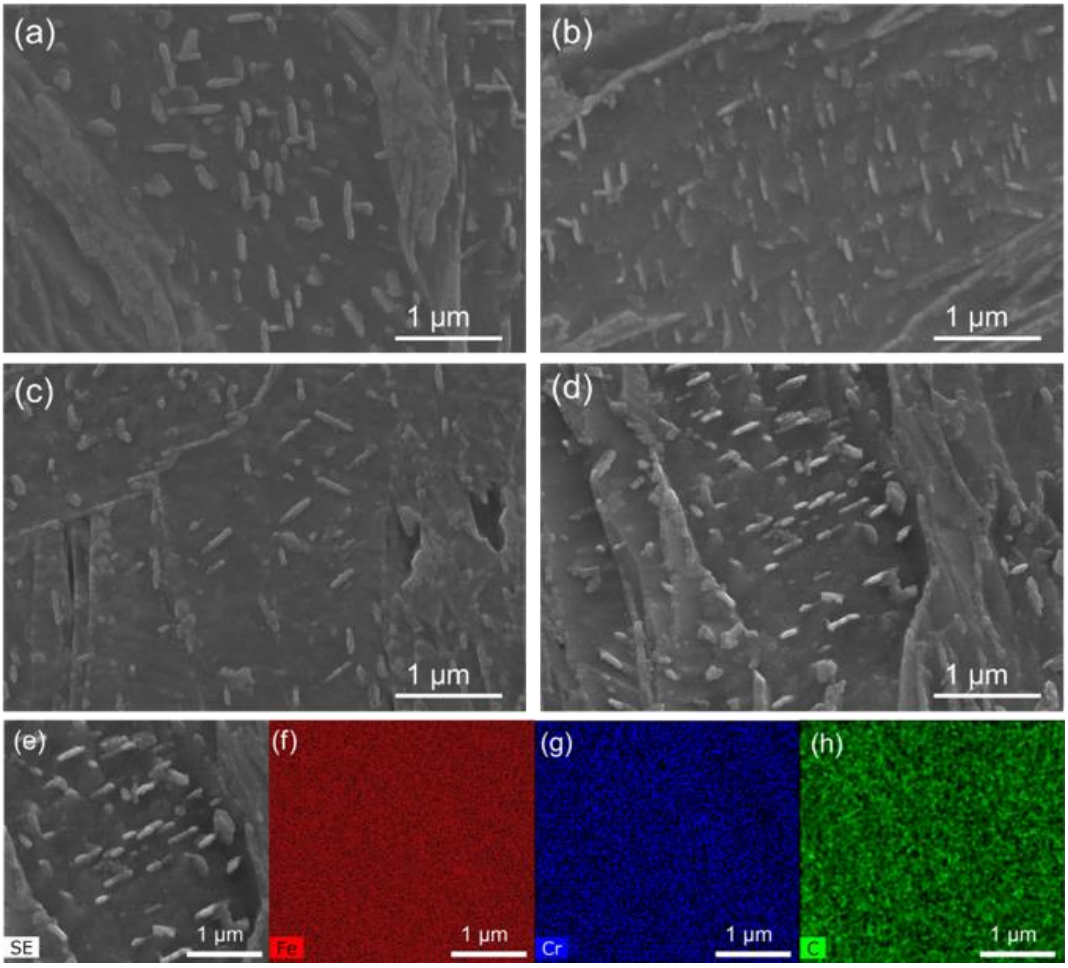

Figure 4.2. SEM images of (a) T400_1h, (b) T400_2h, (c) T400_4h, (d) T400_8h and (e-h) EDX elemental concentration maps of intragranular carbides.

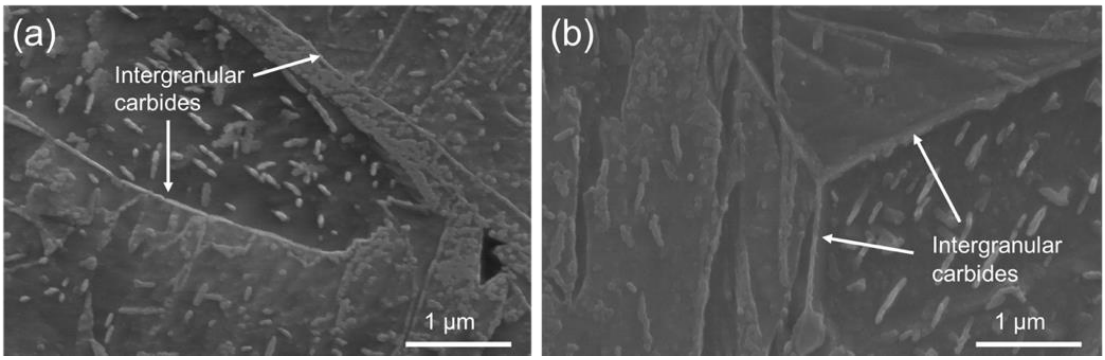

Figure 4.3: SEM images showing the size comparison of intergranular carbide precipitates in (a) T400_1h and (b) T400_8h.

The XRD patterns of the tempered samples can be seen in Figure 4.4. The observed diffraction peaks for all samples are the same, suggesting that a difference in tempering time does not affect the phase structure of MSS. The peaks belong to the BCC phase (annotated by α'), while the carbide precipitates observed in Figures 4.2 and 4.3 were not detected due to the relatively low concentration of the precipitates compared with the martensitic matrix [77]. The similar lattice axis ratio corresponding to alpha ferrite, delta ferrite, and martensite makes it difficult to distinguish the diffraction peaks of these phases from each other [86]. However, based on the results from the SEM analysis seen in Figures 4.1-4.3, it was determined that the diffraction peaks represent the martensite (α') phase.

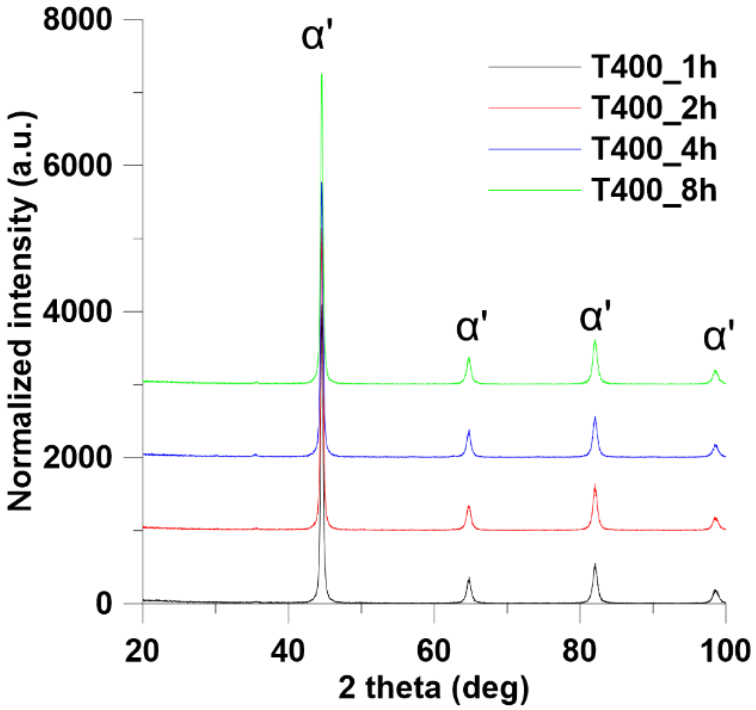

Figure 4.4. XRD patterns of the tempered samples.

Figure 4.5 depicts the inverse pole figures (IPF) as well as grain boundary misorientation maps of T400_1h and T400_8h samples. The IPF maps seen in Figure 4.5a and b were superimposed on the grain boundaries maps to better illustrate the formed lath martensitic structure in the alloy. For both samples, a martensitic microstructure confined within the primary austenite

grain boundaries (PAGB) can be seen. Within the morphology of the observed lath martensitic structure, there is a three-level hierarchy, martensite lath, block, and packet [121]. The grain boundary misorientation maps seen in Figure 4.5c and d clearly reveal the location of the PAGBs and martensite laths, blocks, and packets. These grain boundaries have distinct angles related to them: 2-5° for laths (red), 15-48° for PAGB (blue), and 48-62° for blocks and packets (green) [145]. No significant change in the amount of low and high angle grain boundaries can be seen with increasing the tempering time, suggesting no dominant influence on corrosion behavior from grain boundary misorientation. The lath martensitic structure is fine grained, which is shown by the high number of high-angle grain boundaries between the block and packet martensite seen in Figure 4.5c and d [121].

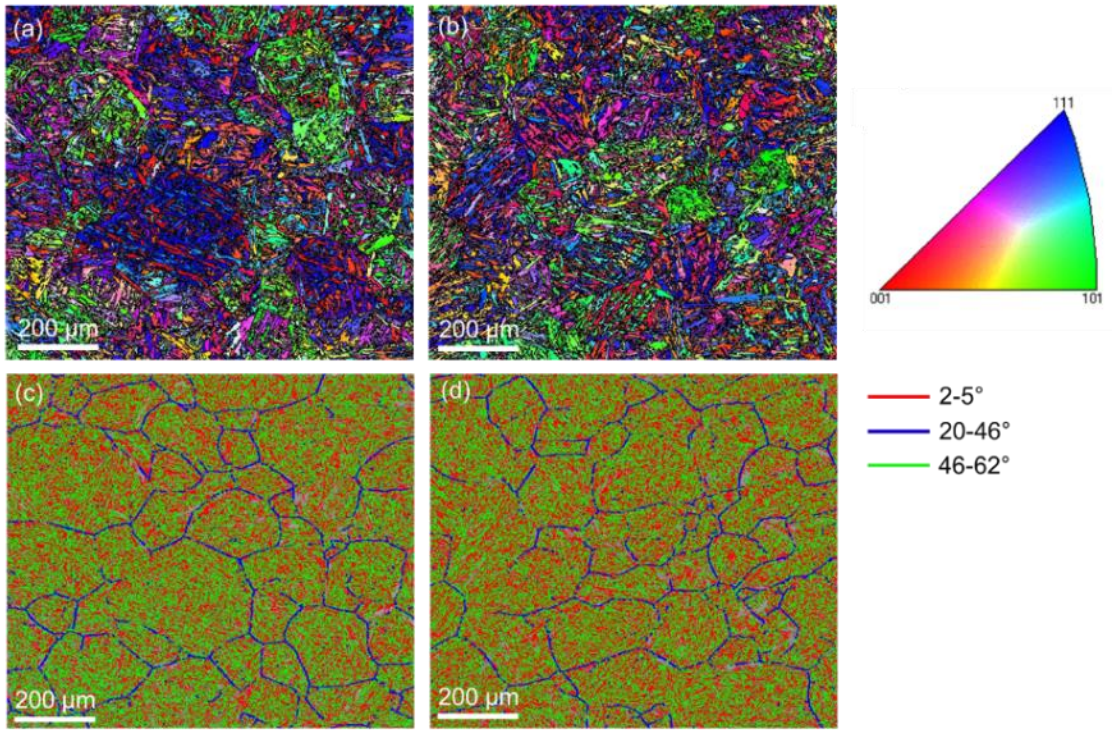

Figure 4.5. EBSD patterns showing inverse pole figures of (a) T400_1h and (b) T400_8h, and grain boundary misorientation maps of (c) T400_1h and (d) T400_8h.

The pole figures representing the body centered cubic (bcc) structure for the tempered martensite laths in T400_1h and T400_8h samples at the {100}, {110}, and {111} planes can

be observed in Figure 4.6a and b. Similar cubic texture was found for the two samples, where the largest values for the high intensity components were 1.59 and 1.53 for T400_1h and T400_8h, respectively, indicating little to no change in texture as tempering time increased. The relatively low texture values in the tempered samples compared with that in the as-printed condition [70] are accredited to the transformation of retained austenite to martensite and the elimination of preferential grain growth during the austenitizing and quenching process [89].

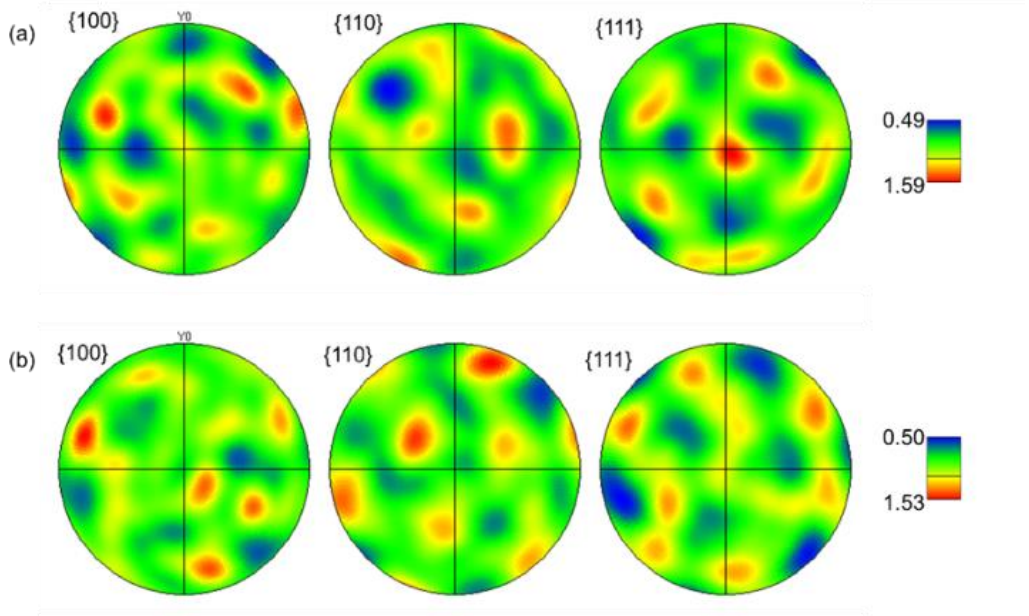

Figure 4.6. The Pole figures of the martensite phase in (a) T400_1h and (b) T400_8h.

3.2. Electrochemical results

The open circuit potential (OCP) after 1 h of immersion time in aerated 3.5 wt.% NaCl solution for all samples are shown in Figure 4.7a. For all samples, the OCP values are relatively stable after 1 h of monitoring. A slight decrease in OCP values at 1 h of immersion time can be seen as tempering time increases. More deterioration of the integrity and density of the passive layer with increasing tempering time is implied by the reduction of OCP values [124].

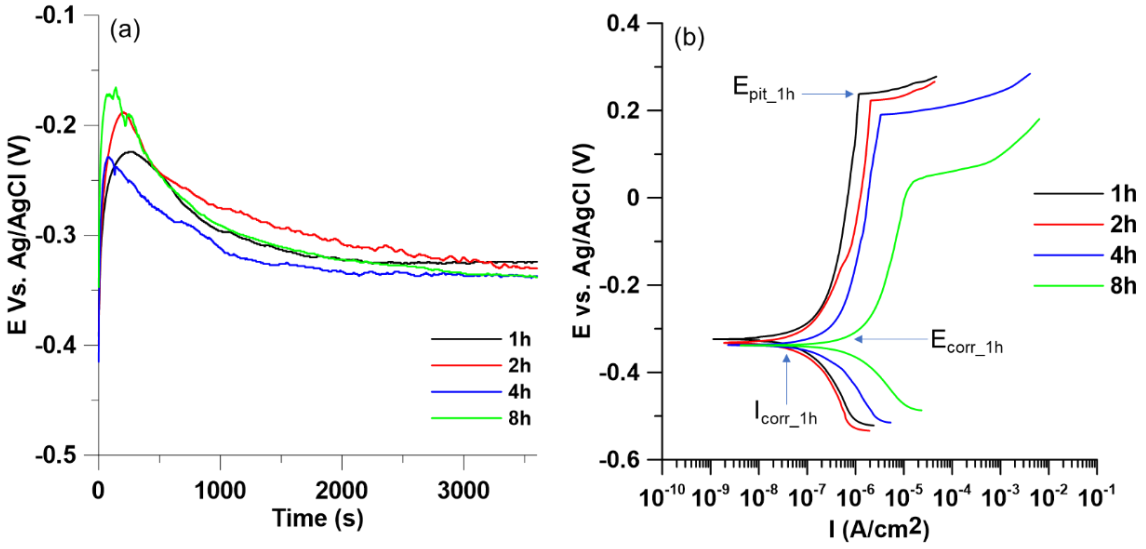

Figure 4.7. Results from the (a) OCP measurements and (b) potentiodynamic polarization test.

The potentiodynamic polarization curves for T400_1h, T400_2h, T400_4h, and T400_8h are depicted in Figure 4.7b. All samples exhibited clear passive regions with distinct pitting potentials. The parameters associated with potentiodynamic polarization, including pitting potential (E_{pit}), corrosion potential (E_{corr}), and corrosion current density (I_{corr}) are marked for T400_1h on the graph in Figure 4.7b. A decrease in E_{pit}, which indicates the resistance to pitting corrosion, can be seen as tempering time increases, with T400_1h having the highest and T400_8h having the lowest values for E_{pit}. Similar values for E_{corr} for all samples can be observed, indicating that the samples have similar tendencies towards oxidation [48]. This is in good agreement with the obtained OCP values. Similarly, a slightly increasing I_{corr} with increasing tempering time suggests a higher corrosion rate for these samples [71]. In addition, the current density for the passive region of the samples increases as tempering time increases, confirming faster dissolution of the passive layer [48].

It is generally agreed upon that micro-constituents, such as carbide precipitates, retained austenite and delta ferrite, affect the corrosion behavior of MSSs. The poor corrosion resistance

in as-printed condition of the part in the present study was correlated to the presence of delta ferrite in the as-printed structure [71]. However, as the performed austenitizing and quenching process eliminated all pre-existing phases, delta ferrite did not affect the corrosion behavior of the tempered samples. The tempering process promoted the growth of carbide precipitates, as was shown in Figures 4.2 and 4.3. The formation of carbides in stainless steel (SS) is known to drain Chromium from the matrix, thus causing regions depleted of Cr around the precipitates, in particular at grain boundaries [142]. Potential differences between the martensitic matrix and carbide precipitates have been shown to cause galvanic couplings between the cathodic carbides and anodic matrix, especially in the carbide/matrix interface regions. As a result, the sensitized regions in these interfaces are highly susceptible to localized corrosive attacks [142].

The lower resistance to corrosion in the samples tempered at longer time is attributed to the further growth of carbides in these samples (Figure 4.3). Increasing the holding time at a set temperature has been shown to cause carbide growth in a MSS [53]. The larger carbides existing in T400_8h have drained more Cr from the nearby matrix, thereby producing larger sensitized regions. Due to this, a less protective passive layer formed, thus a decrease in pitting potential and an increase in the passive current density were seen.

Figure 4.8a and b depict the Bode and Nyquist plots, respectively, generated from the EIS measurements. The samples were all immersed for 1 h, 24 h, and 72 h in an aerated 3.5 wt.% NaCl solution to characterize changes in the passive oxide layer on the surface of the samples with time. The Bode plots seen in Figure 4.8a revealed that either single or double capacitive loops could be observed for all samples, depending on the length of immersion and tempering time. The single capacitive loop represents the double and passive layer, whereas the double capacitive loop is a result of a protective layer [128]. The size of the capacitive semicircles shown in the Nyquist plots of Figure 4.8b can be regarded as an indication of corrosion resistance for the samples, where larger semicircles are related to higher resistance [130]. For

all immersion times, a trend where corrosion resistance decreases as tempering time increases, can be seen. The resistance to corrosion increases for all samples after 24 h of immersion time compared to 1 h, ascribed to the formation of a thicker passive layer with more protective nature after 24 h. Longer immersion time of 72 h shows a decrease in corrosion resistance compared with 24 h due to the degradation of the preformed passive layer.

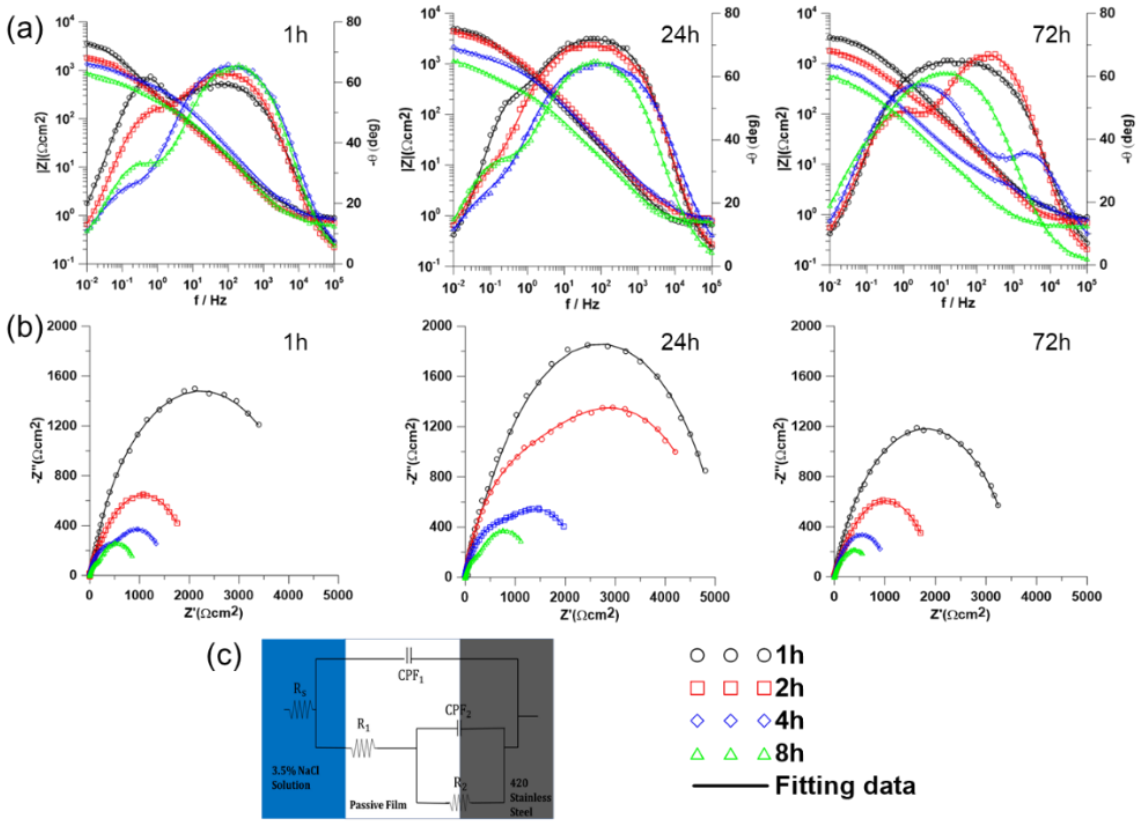

Figure 4.8. Results from the electrochemical impedance spectroscopy, (a) Bode plot after 1h, 24h, and 72h immersion, (c) Nyquist plots after 1h, 24h, and 72h immersion, and (c) the equivalent circuit used to describe the EIS data over time.

It can be observed from the semicircles found in the Nyquist plots and the impedance module of the Bode plots that the highest corrosion resistance belongs to the sample tempered for 1 h, followed subsequently by 2 h, 4 h, and 8 h. This is in good agreement with the obtained PD results presented in Figure 4.7b, where the same order of highest to lowest corrosion resistance could be seen. The fitting data results from the EIS test seen in Table 4.3 show that for all

tempering and immersion times, the values for R_{ct} (charge transfer resistance between matrix and passive layer) are larger than the values for R_p (passive layer resistance). This confirms the formation of a passive layer on the surface of the alloy, which corresponds well with the observed passive regions for all samples in the PD tests. In addition, the values for both R_{ct} and R_p at all immersion times follow the same trend as the impedance modules of the Bode plots, the semicircles of the Nyquist plots, and the polarization graphs of the PD tests, as the impedance values decrease when tempering times increase. The significantly higher values for both R_{ct} and R_p at all immersion times seen for the sample tempered at 1 h compared with the other tempering times suggest that a more protective passive film is present for this sample [68]. In contrast, the lowest R_{ct} and R_p values were observed for the longest tempering time of 8 h, suggesting that longer tempering time is detrimental for the protective nature of the passive film. The values of the constant phase elements belonging to the capacitance of the double layer and passive film, CPE_{ct} and CPE_p respectively, are presented in Table 4.3. Larger CPE_{ct} and CPE_p values suggest a more defected passive film has formed on the sample, which for all immersion times is the case for the longest tempering time (8 h) [68].

Table 4.3. The fitting data values for all tempered samples obtained from EIS after 1h, 24h, and 72h of immersion time.

Sample	R_s (Ωcm^2)	R_p (Ωcm^2)	R_{ct} (Ωcm^2)	CPE_p ($\Omega^{-1} cm^2 s^n$)	n_1	CPE_{ct} ($\Omega^{-1} cm^{-2} s^n$)	n_2
1h_1h	0.82	637	3950	2.12E-04	0.74	1.28E-04	0.75
2h_1h	0.70	322	2097	2.84E-04	0.75	3.29E-04	0.70
4h_1h	0.79	282	1148	3.55E-04	0.70	3.38E-04	0.70
8h_1h	0.61	216	758	4.40E-04	0.70	3.48E-04	0.70
1h_24h	0.63	1420	5038	7.62E-05	0.82	1.18E-04	0.70
2h_24h	0.84	1049	3438	1.04E-04	0.80	1.40E-04	0.70
4h_24h	0.77	564	2002	1.47E-04	0.70	2.26E-04	0.70
8h_24h	0.73	354	1039	1.82E-04	0.78	2.79E-04	0.82
1h_72h	0.80	633	2985	2.53E-04	0.70	1.39E-04	0.70
2h_72h	0.73	159	1802	3.15E-04	0.72	2.96E-04	0.70
4h_72h	0.73	28.2	1241	4.39E-04	0.70	3.10E-04	0.72
8h_72h	0.79	24.3	948	8.32E-04	0.81	3.40E-04	0.70

For calculation of the steady-state passive film thickness (L_{ss}) for all samples, the parallel plate expression was used [136]:

$$L_{ss} = \frac{\varepsilon \varepsilon_0 A}{C_f} \tag{3.1}$$

Here, ε is the dielectric constant for the passive film with a value of 15.6 for Cr_2O_3 [136], ε_0 is the permittivity of vacuum with a value of $8.854 \times 10^{-14}\ Fcm^{-1}$, A is the surface area of the tested sample, and C_f is the pure passive film calculated from:

$$C_f = \frac{(Y_0 R_{ct})^{\frac{1}{n}}}{R_{ct}} \tag{3.2}$$

In equation (2), Y_0 is the CPE constant taken to be CPE_p from Table 4.3, R_{ct} is the charge transfer resistance from Table 4.3, and n is the passive film exponent (n_1 from Table 4.3) [136]. The obtained values for both C_f and L_{ss} are given in Table 4.4. The calculated passive layer thicknesses show that the largest thickness for all immersion times can be found for the sample

tempered for 1 h, and a decreasing thickness can be seen as tempering time increases. It can be seen from Table 4.4 that the thickness increases for all samples from 1 h to 24 h of immersion time, ascribed to the delayed self passivation of the samples. A decrease in thickness from 24 h to 72 h of immersion time occurs for all samples due to the degradation and dissolution of the preformed passive layer at 24 h at longer exposure times to the corrosive solution. The decrease in the stability and thickness of the passive layer with increasing tempering time is associated with the coarser carbide precipitates found in these samples, causing greater sensitization in the carbide adjacent regions [53, 142].

Table 4.4. The values for the capacitance (C_f) and the passive layer thickness for all tempered samples after 1h, 24h, and 72h immersion.

Sample	C_f ($\Omega^{-1}cm^{-2}s^n$)	L_{ss} (nm)
1h_1h	1.99E-04	4.39E-09
2h_1h	2.39E-04	4.04E-09
4h_1h	2.42E-04	3.22E-09
8h_1h	2.75E-04	3.04E-09
1h_24h	6.15E-05	1.42E-08
2h_24h	8.04E-05	1.20E-08
4h_24h	8.70E-05	8.95E-09
8h_24h	1.14E-04	7.34E-09
1h_72h	1.86E-04	4.70E-09
2h_72h	2.53E-04	3.82E-09
4h_72h	3.38E-04	2.30E-09
8h_72h	7.87E-04	2.13E-09

The SEM images of the corroded surfaces of the tempered samples after 1 h of OCP measurement is shown in Figure 4.9. Figure 4.9a-d correspond to T400_1h, T400_2h, T400_4h, and T400_8h, respectively. For all samples, localized corrosion with preferential initiation sites near carbide precipitates in the primary austenite grain boundaries was observed.

As this material is susceptible to chloride corrosion, localized corrosion may take place as early as at the corrosion potential [142]. Comparing the grain boundaries of the tempered samples before and after exposure to the corrosive solution (Figure 4.3 and 4.9, respectively), it can be seen that the continuous network of carbides has been broken up by the corrosion attacks, leaving segments of disrupted carbides networks visible in the grain boundaries. The localized corrosion damage observed in the grain boundaries of the tempered samples results from galvanic corrosion associated with the Chromium depleted regions adjacent to the carbide/matrix interface [142].

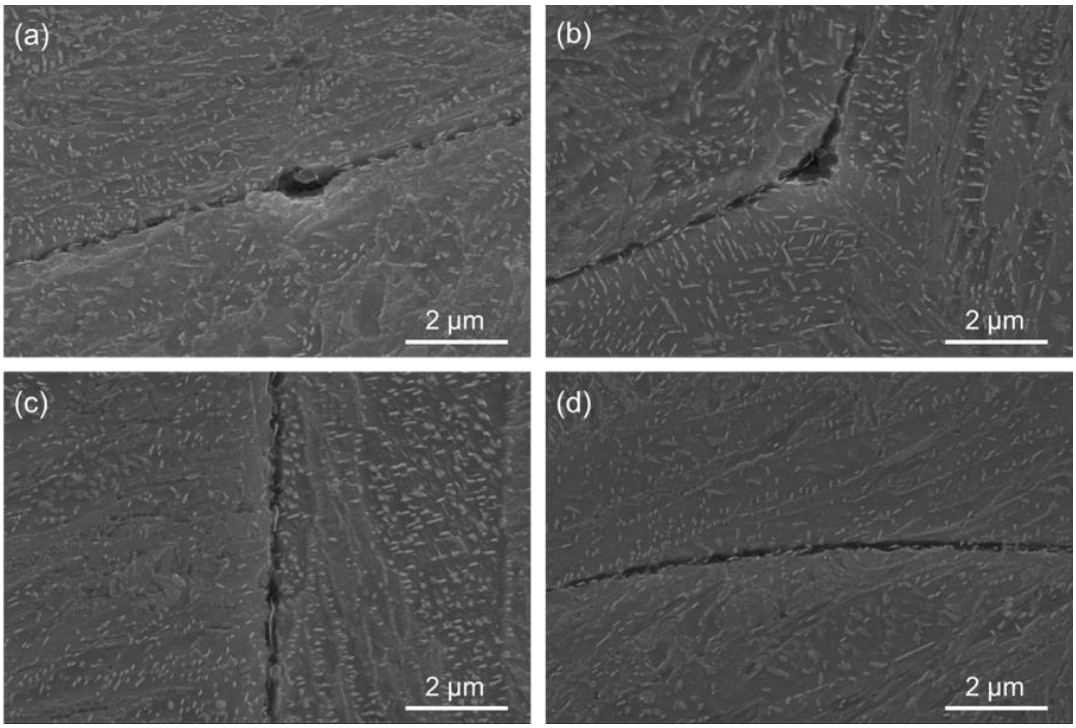

Figure 4.9. SEM images of the corroded surfaces of (a) T400_1h, (b) T400_2h, (c) T400_4h, and (d) T400_8h, after 1 h at OCP.

4. Conclusions

In the present study, the effect of tempering time on the microstructure and corrosion behavior of WAAM fabricated 420 MSS was investigated. The following conclusions were made:

- All pre-existing delta ferrite in the as-printed sample were eliminated by austenitizing at 1150°C for 30 min, a single-phase martensitic microstructure with evenly distributed Cr element was achieved. Tempering at 400°C for 1h, 2h, 4h, and 8h caused precipitation of both intra- and intergranular carbides of the M_3C type. Coarser precipitates were seen in the grain boundaries of the sample tempered for 8h, indicating carbides growth with increasing tempering time. The intergranular carbides mainly formed along the primary austenite grain boundaries.
- Potentiodynamic polarization tests revealed a trend where pitting potential decreased and both corrosion current density and passive current density increased with increasing tempering time, indicating lower pitting resistance in the samples tempered at longer times.
- Through EIS testing, it was determined that less protective passive layers with lower thicknesses formed on the samples as tempering time increased.
- The lower corrosion resistance in the longer tempered samples was due to the growth of carbide precipitates in the primary austenite grain boundaries. Greater sensitization in regions adjacent to the carbide/matrix interface as a result of galvanic coupling occurred as tempering time and consequently carbides' size increased.

Chapter 5

Summary, recommendations, and future works

5.1 Summary

The studies presented herein have been on a wire arc additively manufactured 13Cr martensitic stainless steel part. The mechanical properties of the fabricated part in as-printed condition and corrosion behavior after applying different post-fabrication heat treatments were investigated. In addition, the microstructure of the part was documented in all conditions. It was found that the microstructure of the as-printed part consisted of martensite along with retained austenite and delta ferrite as secondary phases. The high hardness of the martensitic matrix caused the part to be strong and brittle throughout. However, the top region of the fabricated part exhibited lower strength and elongation, attributed to higher hardness resulting from a lack of in-situ re-heating treatment and larger amounts of detrimental delta ferrite phase.

As the microconstituents present in the as-printed part were undesirable a post-fabrication heat treatment was required for elimination of these phases. Austenitizing at 1150°C for 30 min before quenching in air to room temperature was deemed sufficient for removing both retained austenite and delta ferrite, leaving only the martensitic matrix. Tempering after the austenitizing and quenching process for 2 h at 300-600°C was performed before microstructural examination and electrochemical testing revealed which heat treatment process provided the best results. It was determined that tempering at 400°C for 2 h provided best resistance to pitting corrosion and the most stable passive layer out of the investigated

temperatures. These results were ascribed to a lower Cr content in the samples tempered at lower temperatures (300°C and 400°C) compared with higher temperatures (500°C and 600°C).

As tempering at 400°C provided the best resistance to corrosion, the tempering process was investigated further by varying the treatment time. Tempering at 400°C for 1-8 h were performed and the microstructure and electrochemical results were analysed and compared. Based on the results it was determined that by increasing the tempering time the resistance to pitting as well as the passive layer stability and thickness decreased. Longer tempering time promoted the growth of intergranular carbide precipitates, causing larger sensitized regions susceptible to corrosive attacks.

5.2 Recommendations and future works

The following subjects are suggested for future works:

- Accurate identification of the carbide precipitates formed during tempering in the presented study was not possible due to equipment limitations. Proper investigations using transmission electron microscopy (TEM) would be beneficial to determine the effects of both tempering temperature and time on the morphologies and chemical compositions of the precipitates.
- The thin-wall part produced in the presented study was fabricated along the y- and z-axes, which led to in-situ heat treating treatments from above layers. Utilizing deposition along the x-axis as well will create a three-dimensional part which will have experienced a significantly different thermal history than the thin-wall part. Identifying the mechanical properties and corrosion behavior in relation to the microstructure in this part is topic for future works.

References

1. Cobb HM (2010) The History of Stainless Steel. ASM International,
2. Nilsson J-O (2014) Can mankind survive without stainless steels? Stainl Steel World 1–4,
3. Newman M (2020) A SHORT HISTORY ON THE ORIGIN AND DEVELOPMENT OF STAINLESS STEEL. In: Sandvik. https://www.materials.sandvik/en/materials-center/expert-columns/archive/2020/01/a-short-history-on-the-origin-and-development-of-stainless-steel/,
4. Anderson KJ (1993) Steel and Steel Alloys. MRS Bull 18:79–79. https://doi.org/10.1557/s0883769400037611,
5. Jewkes J, Sawers D, Stillerman R (1969) The Sources of Invention, 2nd ed. Macmillan and co ltd, London,
6. Nickel Development Institute (NiDI) (1976) Design guidelines for the selection and use of stainless steel. Des Handb Ser,
7. Davis JR (1994) Asm Specialty Handbook: Stainless Steels,
8. International Stainless Steel Forum (2006) Yearbook of stainless steel applications 2006,
9. Leffler B STAINLESS - stainless steels and their properties,
10. McGuire MF (2008) Stainless Steels for Design Engineers. ASM International,
11. International Stainless Steel Forum Duplex Stainless Steels,
12. Lippold JC, Kotecki DJ (2005) Welding Metallurgy of Stainless Steels - Lippold.pdf. John Wiley and Sons, Hoboken, New Jersey,
13. Cunat P (2004) Alloying elements in stainless steel and other chromium-containing alloys. Int Chromium Dev Assoc … 1–24,
14. Tverberg JC (2003) The Role of Alloying Elements on the Fabricability of Austenitic Stainless Steel. Met Mater Consult Eng,
15. Sun B, Fazeli F, Scott C, Yue S (2016) Phase Transformation Behavior of Medium Manganese Steels with 3 Wt Pct Aluminum and 3 Wt Pct Silicon During Intercritical Annealing. Metall Mater Trans A Phys Metall Mater Sci 47:4869–4882. https://doi.org/10.1007/s11661-016-3678-1,
16. Pardo A, Merino MC, Coy AE, et al (2008) Pitting corrosion behaviour of austenitic stainless steels - combining effects of Mn and Mo additions. Corros Sci 50:1796–1806. https://doi.org/10.1016/j.corsci.2008.04.005,
17. Dutta B, Froes FH (2016) Additive Manufacturing of Titanium Alloys. Elsevier,
18. Duda T, Raghavan LV (2016) 3D Metal Printing Technology. IFAC-PapersOnLine 49:103–110. https://doi.org/10.1016/j.ifacol.2016.11.111,
19. Herderick E (2011) Additive manufacturing of metals: A review. Mater Sci Technol Conf Exhib 2011, MS T'11 2:1413–1425,
20. Bhavar V, Kattire P, Patil V, et al (2017) A review on powder bed fusion technology of metal additive manufacturing. In: Additive Manufacturing Handbook: Product Development for the Defense Industry,
21. Frazier WE (2014) Metal additive manufacturing: A review. J Mater Eng Perform 23:1917–1928. https://doi.org/10.1007/s11665-014-0958-z,
22. Lewandowski JJ, Seifi M (2016) Metal Additive Manufacturing: A Review of Mechanical Properties. Annu Rev Mater Res. https://doi.org/10.1146/annurev-matsci-070115-032024,
23. Barroqueiro B, Andrade-Campos A, Valente RAF, Neto V (2019) Metal additive manufacturing cycle in aerospace industry: A comprehensive review. J Manuf Mater Process 3:1–21. https://doi.org/10.3390/jmmp3030052,

24. Pereira T, Kennedy J V., Potgieter J (2019) A comparison of traditional manufacturing vs additive manufacturing, the best method for the job. Procedia Manuf 30:11–18. https://doi.org/10.1016/j.promfg.2019.02.003,

25. Huang SH, Liu P, Mokasdar A, Hou L (2013) Additive manufacturing and its societal impact: A literature review. Int J Adv Manuf Technol 67:1191–1203. https://doi.org/10.1007/s00170-012-4558-5,

26. Haghdadi N, Laleh M, Moyle M, Primig S (2021) Additive manufacturing of steels: a review of achievements and challenges. J Mater Sci 56:64–107. https://doi.org/10.1007/s10853-020-05109-0,

27. Ge J, Lin J, Chen Y, et al (2018) Characterization of wire arc additive manufacturing 2Cr13 part: Process stability, microstructural evolution, and tensile properties. J Alloys Compd. https://doi.org/10.1016/j.jallcom.2018.03.222,

28. Cherry JA, Davies HM, Mehmood S, et al (2015) Investigation into the effect of process parameters on microstructural and physical properties of 316L stainless steel parts by selective laser melting. Int J Adv Manuf Technol 76:869–879. https://doi.org/10.1007/s00170-014-6297-2,

29. Bajaj P, Hariharan A, Kini A, et al (2020) Steels in additive manufacturing: A review of their microstructure and properties. Mater Sci Eng A 772:. https://doi.org/10.1016/j.msea.2019.138633,

30. Kamariah MSIN, Harun WSW, Khalil NZ, et al (2017) Effect of heat treatment on mechanical properties and microstructure of selective laser melting 316L stainless steel. IOP Conf Ser Mater Sci Eng 257:. https://doi.org/10.1088/1757-899X/257/1/012021,

31. Katherine Adelman B, Nakano K, Yamanaka Advisor H, et al (2018) Heat Treatment Control of Residual Stress and Microstructure of 3D-Printed 316L Stainless Steel,

32. Sistiaga MLM, Nardone S, Hautfenne C, van Humbeeck J (2016) Effect of heat treatment of 316L stainless steel produced by selective laser melting (SLM). Solid Free Fabr 2016 Proc 27th Annu Int Solid Free Fabr Symp - An Addit Manuf Conf SFF 2016 558–565,

33. Williams SW, Martina F, Addison AC, et al (2016) Wire + Arc additive manufacturing. Mater Sci Technol (United Kingdom) 32:641–647. https://doi.org/10.1179/1743284715Y.0000000073,

34. Cunningham CR, Wikshåland S, Xu F, et al (2017) Cost Modelling and Sensitivity Analysis of Wire and Arc Additive Manufacturing. Procedia Manuf 11:650–657. https://doi.org/10.1016/j.promfg.2017.07.163,

35. Rodrigues TA, Duarte V, Miranda RM, et al (2019) Current status and perspectives on wire and arc additive manufacturing (WAAM). Materials (Basel) 12:. https://doi.org/10.3390/ma12071121,

36. Jin W, Zhang C, Jin S, et al (2020) Wire arc additive manufacturing of stainless steels: A review. Appl Sci 10:. https://doi.org/10.3390/app10051563,

37. MacKenzie DS (2008) History of quenching. Int Heat Treat Surf Eng 2:68–73. https://doi.org/10.1179/174951508X358437,

38. Prabhudev KH (1988) Handbook of Heat Treatment of Steels. Tata McGraw-Hill Publishing Company Limited, New Delhi,

39. Salamci E, Candan S, Kabakci F (2017) Effect of microstructure on corrosion behavior of dual-phase steels. Kov Mater 55:133–139. https://doi.org/10.4149/km-2017-2-133,

40. Chaudhuri S (2020) Heat Treatment of Stainless Steels,

41. Padilha AF, Plaut RL, Rios PR (2006) Stainless steel heat treatment. Steel Heat Treat Metall Technol 695–739. https://doi.org/10.1081/e-eisa-120053057,

42. Barlow LD, Du Toit M (2012) Effect of austenitizing heat treatment on the microstructure and hardness of martensitic stainless steel AISI 420. J Mater Eng Perform. https://doi.org/10.1007/s11665-011-0043-9,

43. International Stainless Steel Forum Martensitic Stainless Steels,

44. Wang Z, Palmer TA, Beese AM (2016) Effect of processing parameters on microstructure and tensile

properties of austenitic stainless steel 304L made by directed energy deposition additive manufacturing. Acta Mater. https://doi.org/10.1016/j.actamat.2016.03.019,

45. Kok Y, Tan XP, Wang P, et al (2018) Anisotropy and heterogeneity of microstructure and mechanical properties in metal additive manufacturing: A critical review. Mater Des. https://doi.org/10.1016/j.matdes.2017.11.021,

46. Hejripour F, Binesh F, Hebel M, Aidun DK (2019) Thermal modeling and characterization of wire arc additive manufactured duplex stainless steel. J Mater Process Technol. https://doi.org/10.1016/j.jmatprotec.2019.05.003,

47. Caballero A, Ding J, Ganguly S, Williams S (2019) Wire + Arc Additive Manufacture of 17-4 PH stainless steel: Effect of different processing conditions on microstructure, hardness, and tensile strength. J Mater Process Technol. https://doi.org/10.1016/j.jmatprotec.2019.01.007,

48. Bonagani SK, Bathula V, Kain V (2018) Influence of tempering treatment on microstructure and pitting corrosion of 13 wt.% Cr martensitic stainless steel. Corros Sci. https://doi.org/10.1016/j.corsci.2017.12.012,

49. Chen X, Li J, Cheng X, et al (2018) Effect of heat treatment on microstructure, mechanical and corrosion properties of austenitic stainless steel 316L using arc additive manufacturing. Mater Sci Eng A 715:307–314. https://doi.org/10.1016/j.msea.2017.10.002,

50. Zhang H, Zhao YL, Jiang ZD (2005) Effects of temperature on the corrosion behavior of 13Cr martensitic stainless steel during exposure to CO 2 and Cl - environment. Mater Lett. https://doi.org/10.1016/j.matlet.2005.06.002,

51. Lu SY, Yao KF, Chen YB, et al (2015) Influence of Heat Treatment on the Microstructure and Corrosion Resistance of 13 Wt Pct Cr-Type Martensitic Stainless Steel. Metall Mater Trans A Phys Metall Mater Sci. https://doi.org/10.1007/s11661-015-3180-1,

52. Bilmes PD, Solari M, Llorente CL (2001) Characteristics and effects of austenite resulting from tempering of 13Cr-NiMo martensitic steel weld metals. Mater Charact. https://doi.org/10.1016/S1044-5803(00)00099-1,

53. Mabruri E, Pasaribu RR, Sugandi MT, Sunardi (2018) Effect of high temperature tempering on the mechanical properties and microstructure of the modified 410 martensitic stainless steel. AIP Conf Proc 1964:. https://doi.org/10.1063/1.5038314,

54. Duda T, Raghavan LV (2016) 3D Metal Printing Technology. IFAC-PapersOnLine. https://doi.org/10.1016/j.ifacol.2016.11.111,

55. Ngo TD, Kashani A, Imbalzano G, et al (2018) Additive manufacturing (3D printing): A review of materials, methods, applications and challenges. Compos. Part B Eng.,

56. Wang L, Xue J, Wang Q (2019) Correlation between arc mode, microstructure, and mechanical properties during wire arc additive manufacturing of 316L stainless steel. Mater Sci Eng A. https://doi.org/10.1016/j.msea.2019.02.078,

57. Ge J, Ma T, Chen Y, et al (2019) Wire-arc additive manufacturing H13 part: 3D pore distribution, microstructural evolution, and mechanical performances. J Alloys Compd. https://doi.org/10.1016/j.jallcom.2018.12.274,

58. Vahedi Nemani A, Ghaffari M, Nasiri A (2020) On the Post-Printing Heat Treatment of a Wire Arc Additively Manufactured ER70S Part. Materials (Basel). https://doi.org/10.3390/ma13122795,

59. Rafieazad M, Ghaffari M, Vahedi Nemani A, Nasiri A (2019) Microstructural evolution and mechanical properties of a low-carbon low-alloy steel produced by wire arc additive manufacturing. Int J Adv Manuf Technol. https://doi.org/10.1007/s00170-019-04393-8,

60. Xu X, Ganguly S, Ding J, et al (2018) Microstructural evolution and mechanical properties of maraging steel produced by wire + arc additive manufacture process. Mater Charact. https://doi.org/10.1016/j.matchar.2017.12.002,

61. Ghaffari M, Vahedi Nemani A, Rafieazad M, Nasiri A (2019) Effect of Solidification Defects and HAZ

Softening on the Anisotropic Mechanical Properties of a Wire Arc Additive-Manufactured Low-Carbon Low-Alloy Steel Part. JOM. https://doi.org/10.1007/s11837-019-03773-5,

62. Rodrigues TA, Duarte V, Miranda RM, et al (2019) Current status and perspectives on wire and arc additive manufacturing (WAAM). Materials (Basel). https://doi.org/10.3390/ma12071121,

63. Griffith ML, Ensz MT, Puskar JD, et al (2000) Understanding the microstructure and properties of components fabricated by Laser Engineered Net Shaping (LENS). Mater Res Soc Symp - Proc. https://doi.org/10.1557/PROC-625-9,

64. Li CX, Bell T (2006) Corrosion properties of plasma nitrided AISI 410 martensitic stainless steel in 3.5% NaCl and 1% HCl aqueous solutions. Corros Sci. https://doi.org/10.1016/j.corsci.2005.08.011,

65. Higgins RA (1993) Engineering Metallurgy Part I Applied Physical Metallurgy, 6th ed,

66. Kazemipour M, Salahi S, Nasiri A (2020) Box-Behnken design approach toward predicting the corrosion response of 13Cr stainless steel. Corrosion. https://doi.org/10.5006/3429,

67. Salahi S, Kazemipour M, Nasiri A (2020) Effect of Uniaxial Tension-Induced Plastic Strain on the Microstructure and Corrosion Behavior of 13Cr Martensitic Stainless Steel. CORROSION,

68. Salahi S, Kazemipour M, Nasiri A (2021) Effects of microstructural evolution on the corrosion properties of AISI 420 martensitic stainless steel during cold rolling process. Mater Chem Phys. https://doi.org/10.1016/j.matchemphys.2020.123916,

69. Olsson COA, Landolt D (2003) Passive films on stainless steels - Chemistry, structure and growth. Electrochim Acta. https://doi.org/10.1016/S0013-4686(02)00841-1,

70. Lunde J, Kazemipour M, Salahi S, Nasiri A (2020) Microstructure and Mechanical Properties of AISI 420 Stainless Steel Produced by Wire Arc Additive Manufacturing. In: Minerals, Metals and Materials Series,

71. Kazemipour M, Lunde JH, Salahi S, Nasiri A (2020) On the Microstructure and Corrosion Behavior of Wire Arc Additively Manufactured AISI 420 Stainless Steel. In: Minerals, Metals and Materials Series,

72. Baghjari SH, Akbari Mousavi SAA (2013) Effects of pulsed Nd: YAG laser welding parameters and subsequent post-weld heat treatment on microstructure and hardness of AISI 420 stainless steel. Mater Des. https://doi.org/10.1016/j.matdes.2012.06.027,

73. Tarasov SY, Filippov A V., Shamarin NN, et al (2019) Microstructural evolution and chemical corrosion of electron beam wire-feed additively manufactured AISI 304 stainless steel. J Alloys Compd. https://doi.org/10.1016/j.jallcom.2019.06.246,

74. Ge J, Lin J, Fu H, et al (2018) Tailoring microstructural features of wire arc additive manufacturing 2Cr13 part via varying inter-layer dwelling time. Mater Lett. https://doi.org/10.1016/j.matlet.2018.08.037,

75. Bahrami Balajaddeh M, Naffakh-Moosavy H (2019) Pulsed Nd:YAG laser welding of 17-4 PH stainless steel: Microstructure, mechanical properties, and weldability investigation. Opt Laser Technol. https://doi.org/10.1016/j.optlastec.2019.105651,

76. Ge J, Lin J, Fu H, et al (2018) A spatial periodicity of microstructural evolution and anti-indentation properties of wire-arc additive manufacturing 2Cr13 thin-wall part. Mater Des. https://doi.org/10.1016/j.matdes.2018.09.021,

77. Ge J, Lin J, Lei Y, Fu H (2018) Location-related thermal history, microstructure, and mechanical properties of arc additively manufactured 2Cr13 steel using cold metal transfer welding. Mater Sci Eng A. https://doi.org/10.1016/j.msea.2017.12.076,

78. Pickering FB (1979) , The Metallurgical Evolution of Stainless Steels, a Discriminative Selection of Outstanding Articles and Papers from the Scientific Literature. Am Soc Met,

79. Krakhmalev P, Yadroitsava I, Fredriksson G, Yadroitsev I (2015) In situ heat treatment in selective laser melted martensitic AISI 420 stainless steels. Mater Des. https://doi.org/10.1016/j.matdes.2015.08.045,

80. Ali Y, Henckell P, Hildebrand J, et al (2019) Wire arc additive manufacturing of hot work tool steel

with CMT process. J Mater Process Technol. https://doi.org/10.1016/j.jmatprotec.2019.01.034,

81. Irvine KJ, Crowe DJ, Pickering FB (1960) The physical metallurgy of 12% chromium steels. J iron steel Inst 195:386–405,

82. Steven W, Haynes AG (1956) The temperature of formation of martensite and bainite in low-alloy steels. J Iron Steel Inst 183:349–359,

83. Andrews K (1965) Empirical Formulae for the calculation of some transformation temperatures. J Iron Steel Inst 203:721–727,

84. Gooch GT (1977) Welding martensitic stainless steels. Weld Inst Res Bull 18:343–349,

85. Self JA, Olson DL, R. EG (1984) The stability of austenitic weld metal. Proc IMCC,

86. Lu SY, Yao KF, Chen YB, et al (2015) The effect of tempering temperature on the microstructure and electrochemical properties of a 13 wt.% Cr-type martensitic stainless steel. Electrochim Acta. https://doi.org/10.1016/j.electacta.2015.02.038,

87. Li S, Beyerlein IJ, Bourke MAM (2005) Texture formation during equal channel angular extrusion of fcc and bcc materials: Comparison with simple shear. Mater Sci Eng A. https://doi.org/10.1016/j.msea.2004.11.032,

88. Raabe D, Luecke K (1994) Rolling and annealing textures of bcc metals. Mater Sci Forum. https://doi.org/10.4028/www.scientific.net/msf.157-162.597,

89. Suwas S, Kumar Ray R (2014) Crystallographic texture of materials. Springer, London,

90. Fathi P, Rafieazad M, Duan X, et al (2019) On microstructure and corrosion behaviour of AlSi10Mg alloy with low surface roughness fabricated by direct metal laser sintering. Corros Sci. https://doi.org/10.1016/j.corsci.2019.05.032,

91. Ghaffari M, Vahedi Nemani A, Nasiri A (2020) Interfacial bonding between a wire arc additive manufactured 420 martensitic stainless steel part and its wrought base plate. Mater Chem Phys. https://doi.org/10.1016/j.matchemphys.2020.123199,

92. Vahedi Nemani A, Ghaffari M, Nasiri A (2020) Comparison of microstructural characteristics and mechanical properties of shipbuilding steel plates fabricated by conventional rolling versus wire arc additive manufacturing. Addit Manuf. https://doi.org/10.1016/j.addma.2020.101086,

93. Shahriari A, Khaksar L, Nasiri A, et al (2020) Microstructure and corrosion behavior of a novel additively manufactured maraging stainless steel. Electrochim Acta. https://doi.org/10.1016/j.electacta.2020.135925,

94. Yangfan W, Xizhang C, Chuanchu S (2019) Microstructure and mechanical properties of Inconel 625 fabricated by wire-arc additive manufacturing. Surf Coatings Technol. https://doi.org/10.1016/j.surfcoat.2019.05.079,

95. Bonagani SK, Vishwanadh B, Tenneti S, et al (2019) Influence of tempering treatments on mechanical properties and hydrogen embrittlement of 13 wt% Cr martensitic stainless steel. Int J Press Vessel Pip 176:103969. https://doi.org/10.1016/j.ijpvp.2019.103969,

96. ASM International (2016) One Minute Mentor: Tempering Corrosion-Resistant Tool Steels. https://www.asminternational.org/web/hts/news/newswire/-/journal_content/56/10192/26295783/NEWS. Accessed 4 Sep 2020,

97. Pan L, Kwok CT, Lo KH (2019) Enhancement in hardness and corrosion resistance of AISI 420 martensitic stainless steel via friction stir processing. Surf Coatings Technol. https://doi.org/10.1016/j.surfcoat.2018.10.023,

98. Shi J, Sun X, Wang M, et al (2010) Enhanced work-hardening behavior and mechanical properties in ultrafine-grained steels with large-fractioned metastable austenite. Scr Mater. https://doi.org/10.1016/j.scriptamat.2010.06.023,

99. Polatidis E, Hsu WN, Šmíd M, et al (2018) Suppressed martensitic transformation under biaxial loading in low stacking fault energy metastable austenitic steels. Scr Mater.

https://doi.org/10.1016/j.scriptamat.2017.12.026,

100. Schäfer L (1998) Influence of delta ferrite and dendritic carbides on the impact and tensile properties of a martensitic chromium steel. J Nucl Mater. https://doi.org/10.1016/S0022-3115(98)00200-1,

101. Lin YC, Chen SC (2003) Effect of residual stress on thermal fatigue in a type 420 martensitic stainless steel weldment. In: Journal of Materials Processing Technology,

102. Zhang X, Zhou Q, Wang K, et al (2019) Study on microstructure and tensile properties of high nitrogen Cr-Mn steel processed by CMT wire and arc additive manufacturing. Mater Des. https://doi.org/10.1016/j.matdes.2019.107611,

103. Feng Y, Zhan B, He J, Wang K (2018) The double-wire feed and plasma arc additive manufacturing process for deposition in Cr-Ni stainless steel. J Mater Process Technol. https://doi.org/10.1016/j.jmatprotec.2018.04.040,

104. Alam MK, Mehdi M, Urbanic RJ, Edrisy A (2020) Mechanical behavior of additive manufactured AISI 420 martensitic stainless steel. Mater Sci Eng A,

105. Wu B, Pan Z, Ding D, et al (2018) A review of the wire arc additive manufacturing of metals: properties, defects and quality improvement. J. Manuf. Process.,

106. Yu J, Rombouts M, Maes G (2013) Cracking behavior and mechanical properties of austenitic stainless steel parts produced by laser metal deposition. Mater Des. https://doi.org/10.1016/j.matdes.2012.08.078,

107. Lemke JN, Simonelli M, Garibaldi M, et al (2017) Calorimetric study and microstructure analysis of the order-disorder phase transformation in silicon steel built by SLM. J Alloys Compd. https://doi.org/10.1016/j.jallcom.2017.06.085,

108. Isfahany AN, Saghafian H, Borhani G (2011) The effect of heat treatment on mechanical properties and corrosion behavior of AISI420 martensitic stainless steel. J Alloys Compd. https://doi.org/10.1016/j.jallcom.2010.12.174,

109. Aquino JM, Della Rovere CA, Kuri SE (2009) Intergranular corrosion susceptibility in supermartensitic stainless steel weldments. Corros Sci. https://doi.org/10.1016/j.corsci.2009.06.009,

110. Mabruri E, Sujianto, Anwar MS, et al (2019) Comparison of strength, microstructure and corrosion resistance of stainless steels type 410 and type 410-3Mo in tempered condition. In: Materials Today: Proceedings,

111. Wen DX, Long P, Li JJ, et al (2020) Effects of linear heat input on microstructure and corrosion behavior of an austenitic stainless steel processed by wire arc additive manufacturing. Vacuum. https://doi.org/10.1016/j.vacuum.2019.109131,

112. ASM International (1991) ASM Handbook, Volume 4 - Heat Treating. ASM International,

113. Jiang W, Zhao K yu, Ye D, et al (2013) Effect of Heat Treatment on Reversed Austenite in Cr15 Super Martensitic Stainless Steel. J Iron Steel Res Int. https://doi.org/10.1016/S1006-706X(13)60099-0,

114. Tavares SSM, da Silva FJ, Scandian C, et al (2010) Microstructure and intergranular corrosion resistance of UNS S17400 (17-4PH) stainless steel. Corros Sci. https://doi.org/10.1016/j.corsci.2010.07.016,

115. Bilmes PD, Llorente CL, Saire Huamán L, et al (2006) Microstructure and pitting corrosion of 13CrNiMo weld metals. Corros Sci. https://doi.org/10.1016/j.corsci.2005.10.009,

116. Dadfar M, Fathi MH, Karimzadeh F, et al (2007) Effect of TIG welding on corrosion behavior of 316L stainless steel. Mater Lett. https://doi.org/10.1016/j.matlet.2006.09.008,

117. Aquino JM, Della Rovere CA, Kuri SE (2008) Localized corrosion susceptibility of supermartensitic stainless steel in welded joints. Corrosion. https://doi.org/10.5006/1.3278459,

118. Acciari HA, Guastaldi AC, Brett CMA (2001) On the development of the electrochemical potentiokinetic method. Electrochim Acta. https://doi.org/10.1016/S0013-4686(01)00674-0,

119. Da Silva GF, Tavares SSM, Pardal JM, et al (2011) Influence of heat treatments on toughness and

sensitization of a Ti-alloyed supermartensitic stainless steel. J Mater Sci. https://doi.org/10.1007/s10853-011-5753-8,

120. De Andrés CG, Caruana G, Alvarez LF (1998) Control of M23C6 carbides in 0.45C-13Cr martensitic stainless steel by means of three representative heat treatment parameters. Mater Sci Eng A. https://doi.org/10.1016/s0921-5093(97)00491-7,

121. Kitahara H, Ueji R, Tsuji N, Minamino Y (2006) Crystallographic features of lath martensite in low-carbon steel. Acta Mater 54:1279–1288,

122. Wang Q, Zhang S, Zhang C, et al (2017) Microstructure evolution and EBSD analysis of a graded steel fabricated by laser additive manufacturing. Vacuum 141:68–81,

123. Wei HL, Mazumder J, DebRoy T (2015) Evolution of solidification texture during additive manufacturing. Sci Rep 5:16446,

124. Song D, Ma A, Sun W, et al (2014) Improved corrosion resistance in simulated concrete pore solution of surface nanocrystallized rebar fabricated by wire-brushing. Corros Sci. https://doi.org/10.1016/j.corsci.2014.01.034,

125. Kirchheim R, Heine B, Fischmeister H, et al (1989) The passivity of iron-chromium alloys. Corros Sci. https://doi.org/10.1016/0010-938X(89)90060-7,

126. Forman CM, Verchot EA (1967) Practical Galvanic Series,

127. Kvryan A, Efaw CM, Higginbotham KA, et al (2019) Corrosion initiation and propagation on carburized martensitic stainless steel surfaces studied via advanced scanning probe microscopy. Materials (Basel). https://doi.org/10.3390/ma12060940,

128. Zeng CL, Wang W, Wu WT (2001) Electrochemical impedance models for molten salt corrosion. Corros Sci. https://doi.org/10.1016/S0010-938X(00)00108-6,

129. Cao C nan (1990) On the impedance plane displays for irreversible electrode reactions based on the stability conditions of the steady-state-I. One state variable besides electrode potential. Electrochim Acta. https://doi.org/10.1016/0013-4686(90)90077-D,

130. Kocijan A, Merl DK, Jenko M (2011) The corrosion behaviour of austenitic and duplex stainless steels in artificial saliva with the addition of fluoride. Corros Sci. https://doi.org/10.1016/j.corsci.2010.11.010,

131. Schmutz P (1998) Corrosion Study of AA2024-T3 by Scanning Kelvin Probe Force Microscopy and In Situ Atomic Force Microscopy Scratching. J Electrochem Soc. https://doi.org/10.1149/1.1838634,

132. Kong D, Xu A, Dong C, et al (2017) Electrochemical investigation and ab initio computation of passive film properties on copper in anaerobic sulphide solutions. Corros Sci. https://doi.org/10.1016/j.corsci.2016.12.010,

133. Sikora E, Macdonald DD (1997) Defining the passive state. Solid State Ionics. https://doi.org/10.1016/s0167-2738(96)00505-x,

134. Fattah-alhosseini A, Golozar MA, Saatchi A, Raeissi K (2010) Effect of solution concentration on semiconducting properties of passive films formed on austenitic stainless steels. Corros Sci. https://doi.org/10.1016/j.corsci.2009.09.003,

135. Nicic I, Macdonald DD (2008) The passivity of Type 316L stainless steel in borate buffer solution. J Nucl Mater. https://doi.org/10.1016/j.jnucmat.2008.06.014,

136. Feng Z, Cheng X, Dong C, et al (2010) Passivity of 316L stainless steel in borate buffer solution studied by Mott-Schottky analysis, atomic absorption spectrometry and X-ray photoelectron spectroscopy. Corros Sci. https://doi.org/10.1016/j.corsci.2010.07.013,

137. Kong D, Ni X, Dong C, et al (2018) Bio-functional and anti-corrosive 3D printing 316L stainless steel fabricated by selective laser melting. Mater Des. https://doi.org/10.1016/j.matdes.2018.04.058,

138. Ryan MP, Williams DE, Chater RJ, et al (2002) Why stainless steel corrodes. Nature. https://doi.org/10.1038/415770a,

139. Da Costa E Silva ALV (2019) The effects of non-metallic inclusions on properties relevant to the performance of steel in structural and mechanical applications. J. Mater. Res. Technol.,

140. Aydoğdu GH, Aydinol MK (2006) Determination of susceptibility to intergranular corrosion and electrochemical reactivation behaviour of AISI 316L type stainless steel. Corros Sci. https://doi.org/10.1016/j.corsci.2006.01.003,

141. Montevecchi F, Venturini G, Grossi N, et al (2017) Finite Element mesh coarsening for effective distortion prediction in Wire Arc Additive Manufacturing. Addit Manuf 18:145–155. https://doi.org/10.1016/j.addma.2017.10.010,

142. Anantha KH, Örnek C, Ejnermark S, et al (2017) Correlative Microstructure Analysis and In Situ Corrosion Study of AISI 420 Martensitic Stainless Steel for Plastic Molding Applications. J Electrochem Soc. https://doi.org/10.1149/2.0531704jes,

143. Zhang S, Wang P, Li D, Li Y (2015) Investigation of the evolution of retained austenite in Fe-13%Cr-4%Ni martensitic stainless steel during intercritical tempering. Mater Des 84:385–394. https://doi.org/10.1016/j.matdes.2015.06.143,

144. Scheuer CJ, Possoli F, Borges PC, et al (2019) AISI 420 martensitic stainless steel corrosion resistance enhancement by low-temperature plasma carburizing. Electrochim Acta 317:70–82. https://doi.org/10.1016/j.electacta.2019.05.101,

145. Back JG, Engberg G (2017) Investigation of parent austenite grains from Martensite Structure Using EBSD in a Wear Resistant steel. Materials (Basel) 10:. https://doi.org/10.3390/ma10050453